

# **High Capacity Main Group Anodes for Advanced Lithium-ion and Sodium-ion Batteries**

by

**Hezhen Xie**

A thesis submitted in partial fulfillment of the requirements for the degree of

**Doctor of Philosophy**

Department of Chemistry  
University of Alberta

© Hezhen Xie, 2019

# Abstract

Nowadays, rechargeable batteries play an ever more important role in our society as an energy storage medium for a wide range of applications from tiny electronic devices to grid-level energy storage. Among the different types of batteries, lithium-ion batteries (LIBs) have achieved significant advances during the last three decades and currently dominate the market. However, to meet the needs for emerging energy storage scenarios, such as electrical vehicles, improvement of battery performance in terms of energy density, cycling life, and safety is still required. In addition to LIBs, sodium-ion batteries (SIBs) are of great interest due to the abundance and wide geographical distribution of Na resources, especially for grid-scale battery applications. SIBs lag, however, far behind LIBs in terms of research and development and suffer from sluggish kinetics, poor cycling stability, and lower energy density. The development of high-performance LIBs mainly relies on improving the electrode materials. Therefore, studying the electrode materials for LIBs and SIBs is essential. This thesis focuses on understanding and developing high capacity alloying anode materials for the next-generation high-performance LIBs and SIBs.

This thesis starts with an introduction to the motivation, working principles, and evaluation criteria of LIBs and SIBs. We begin with the research background of high capacity alloying anodes, including Sn, Sb, and Si based anodes. The three research projects are described as follows.

In the first project, three series of ternary Sn–Bi–Sb alloy electrodes, as well as elemental Sn, Bi, and Sb electrodes, were prepared by magnetron sputtering, and their electrochemical performance as anodes for SIBs was examined. Alloying was used as

the method to modify the morphology and electrochemical charge/discharge behavior in order to improve the cyclability of pure Sn and Sb electrodes. The prepared alloys were found to outperform the pure elements in terms of cycling stability and rate capability. The best performing alloy, composed of 80 at% Sb, 10 at% Sn, and 10 at% Bi, shows negligible capacity degradation after 100 charge/discharge cycles. The improved performance is ascribed to the increased resistance toward internal stresses and modification of Sb chemical potential induced by the dissolution of Sn and Bi atoms in the Sb lattice.

The second project was to investigate the sodiation–desodiation mechanism of  $\beta$ -SnSb, which is a highly stable anode material for SIBs but is poorly understood with respect to its reaction mechanism with Na. By combining in-situ TEM, ex-situ X-ray diffraction, and electroanalytical methods, it was found that sodiation of  $\beta$ -SnSb leads to the formation of  $\text{Na}_3\text{Sb}$  and  $\text{Na}_{15}\text{Sn}_4$  in sequence and that upon desodiation,  $\beta$ -SnSb reforms. The amorphous-nanocrystalline microstructure during the sodiation–desodiation and the intrinsic mechanical toughness of the  $\beta$ -SnSb account for the good cycling stability of  $\beta$ -SnSb.

In the third project, the effect of the Ni adhesion layer and C/TiO<sub>2</sub> surface coatings on the formation of both the c-Li<sub>3.75</sub>Si phase and the solid electrolyte interphase (SEI) in Si-based anodes was investigated. The adhesion layer and surface coatings were found to suppress the formation of c-Li<sub>3.75</sub>Si, resulting in improved capacity retentions and Coulombic efficiency. In addition, surface coatings were found to influence the growth rate and composition of SEI.

The thesis concludes with a summary of each chapter and directions for future studies.

# Preface

This thesis is composed of five chapters. Chapter 1 introduces the background and basic concepts for lithium-ion and sodium-ion batteries, with an emphasis on the Sn, Sb, and Si based anodes. Chapter 2 investigates three series of ternary Sn–Bi–Sb alloys as anodes for sodium-ion batteries. Chapter 3 presents a study of the sodiation–desodiation mechanism of a promising anode,  $\beta$ -SnSb, for sodium-ion batteries. Chapter 4 studies the effect of both an adhesion layer and a surface coating on the suppression of the c- $\text{Li}_{3.75}\text{Si}$  phase and the growth of the solid electrolyte interphase in Si-based anodes, which is the most promising anode material for lithium-ion batteries. Finally, Chapter 5 summarizes the research findings and provides several research directions for future work.

The work described in Chapter 2 has been published as: “Xie, H.; Kalisvaart, W. P.; Olsen, B. C.; Lubner, E. J.; Mitlin, D.; Buriak, J. M. Sn–Bi–Sb Alloys as Anode Materials for Sodium Ion Batteries. *J. Mater. Chem. A* **2017**, *5* (20), 9661–9670.” I designed the initial experimental plan with Brian C. Olsen, and conducted all the experiments, analyzed the results, and wrote the initial manuscript. Dr. Erik J. Lubner and Brian C. Olsen helped with data analysis, figure preparation, and manuscript revision. Dr. W. Peter Kalisvaart helped with data analysis and manuscript writing. Prof. David Mitlin reviewed and revised the manuscript. Prof. Jillian M. Buriak was the supervisor and helped to prepare the manuscript.

Chapter 3 is based on the following publication: “Xie, H.; Tan, X.; Lubner, E. J.; Olsen, B. C.; Kalisvaart, W. P.; Jungjohann, K. L.; Mitlin, D.; Buriak, J. M.  $\beta$ -SnSb for Sodium Ion Battery Anodes: Phase Transformations Responsible for Enhanced Cycling Stability Revealed by In Situ TEM. *ACS Energy Lett.* **2018**, *3* (7), 1670–

1676". Dr. Xuehai Tan and I designed the research plan, conducted the in-situ TEM experiment, and wrote the first manuscript. I performed the ex-situ characterizations and electrochemical tests and analyzed the data. Dr. Erik J. Lubner assisted with the sample preparation for the in-situ TEM experiment and manuscript writing, and Brian C. Olsen helped with the figure and manuscript preparation. Dr. W. Peter Kalisvaart contributed to the data analysis and manuscript revision. Dr. Katherine L. Jungjohann from the Center for Integrated Nanotechnologies, Sandia National Laboratories assisted with the in-situ TEM experiments. Prof. David Mitlin wrote the proposal for the in-situ TEM experiments to help us get the beam time and contributed to the manuscript writing. Prof. Jillian M. Buriak coordinated the collaborations and assisted in writing the manuscript.

The work in Chapter 4 also has been written as a manuscript. I proposed the initial ideas, performed the experiments, analyzed the data, and wrote the manuscript. Dr. Sayed Youssef Sayed assisted with the design of the experimental plan, sample preparation of the in-operando neutron reflectometry (NR) experiments, and revision of the manuscript. Dr. W. Peter Kalisvaart helped with the planning of the in-operando NR experiments and manuscript writing. Simon Schaper, Tobias Widmann, Lucas Kreuzer, Dr. Gaetano Mangiapia, Martin Haese, and Prof. Peter Müller-Buschbaum assisted with the in-operando NR experiments. Brian C. Olsen and Dr. Erik J. Lubner contributed to discussions of experimental results. Prof. Jillian M. Buriak was the supervisor; she coordinated the collaborations and assisted in writing the manuscript.

# Acknowledgment

At the end of my Ph.D. program, I would like to express my deep appreciation to the people who helped me during my studies. First and foremost, I would like to thank my supervisor, Dr. Jillian M. Buriak, for her continuous support for my research and professional development. Your passion for science and comprehensive knowledge inspired me to explore interesting topics in science and overcome the challenges in my research over the last five years. I am also grateful for your support and encouragement in the different collaborative projects, where I met a lot of great researchers from all over the world and broadened my horizons.

I would also like to thank my supervisory committee members, Dr. Julianne M. Gibbs and Dr. Rylan Lundgren, for their advice for my career and support for my studies. Thanks to my examination committee members, Dr. Weixing Chen and Dr. Steven Bergens for your thoughtful examination and suggestions. In addition, I am grateful to Dr. Xueliang (Andy) Sun from Western University for agreeing to be the external examiner for my Ph.D. defence. Thanks to Dr. Bob Jordan for chairing my defence examination.

My deep thanks to previous and current team members of the Buriak research group. Thanks to Dr. Peter Kalisvaart for your efficient help in research and manuscript writing. Dr. Sayed Youssef Sayed, thank you for your tireless support and guidance in my research. Brian Olsen, thanks for your versatile technical skills and knowledge. Dr. Erik Lubber, thank you for your assistance, guidance and encouragement in research. Jennifer Ozdoba, thank you for your kindness and friendly assistance in research. Thank you, Tate Hauger, for your kindness and eagerness to help. Thanks to Dr. Fenglin Liu, Dr. Cong Jin, and Dr. Bing Cao for

your encouragement and sharing of your experience. Thanks to Chengcheng Rao, Hao Wang, Minjia Hu, Mahmoud Almadhoun, Dr. Jeremy Bau, Dr. Christopher Fetterly, Dr. Jeffrey Murphy, Kelli Lubber, Gayashani Ginige, Jasper Woodard, and Aaron Kirkey for your assistance and inspiration.

I would also like to thank my collaborators for their support and sharing of their expertise: Dr. Xuehai Tan, Dr. Maryam Aghajamali, Dr. Jonathan G. C. Veinot, Dr. David Mitlin, Dr. Katherine L. Jungjohann, Dr. Peter Müller-Buschbaum, Simon Schaper, Tobias Widmann, Lucas Kreuzer, Dr. Gaetano Mangiapia, Martin Haese.

Thanks to all the staff in the Chemistry department, NRC-NINT, and nanoFAB for their support on my studies and research work: Anita Weiler, Jason Dibbs, Paul Concepcion, Steve Launspach, Dr. Anqiang He, Dr. Shihong Xu, Aditi Ganji. A deep thanks to Dr. Michael Fleischauer for your support in research. A very big thank you to Dr. Anna Jordan for helping me carefully edit my thesis.

I also would like to thank my funding resource, including the University of Alberta, and Alberta Innovates. Thanks to ATUMS for supporting my research exchange in Germany and to Leah Veinot for organizing various professional development events. Thanks to the previous and current members of the U of A Nanogroup and Chemistry Graduate Students' Society for your support in the organization of events; they helped me gain valuable experience.

And last but far from least, many thanks to my family members. Thanks to my parents (Donglan Shi and Jinyou Xie), grandparents (Yulan Xiang, Xianren Shi, Tongxiu Xiang, Zhongming Xie), aunt (Chunlan Shi), and uncle (Zhangyou Shi) for your love and support in my life. A special thank you is reserved for my love and partner, Ming Lyu. Without you, I would never have made it this far.

# Table of Contents

<b>1. Introduction.....</b>	<b>1</b>
1.1 Why Lithium-ion and Sodium-ion Batteries?.....	1
1.1.1 Electrical Energy Storage Demand and Challenges .....	1
1.1.2 Advantages of Lithium-ion Batteries and Applications.....	1
1.1.3 Interests of Sodium-ion Batteries and Potential Applications .....	2
1.2 Basic Concept of Batteries and Evaluation Criteria for Battery Electrode Materials .....	3
1.2.1 Working Principles of Lithium-ion and Sodium-ion Batteries.....	3
1.2.2 Evaluation Parameters for Electrode Materials .....	5
1.3 High Capacity Main Group Alloying Anodes for Sodium-Ion Batteries .....	7
1.3.1 Overview of High Capacity Alloying Anodes.....	7
1.3.2 Active–Inactive and All–Active Alloys Anodes.....	10
1.3.3 Sn-based Alloys .....	12
1.3.4 Sb-based Alloys .....	14
1.3.5 Challenges of Alloying Anodes Towards Practical Applications.....	17
1.4 Silicon-based Anodes for Lithium-ion Batteries .....	18
1.5 Scope of the Thesis .....	21
1.5.1 Chapter 1 Scope .....	21
1.5.2 Chapter 2 Scope .....	21
1.5.3 Chapter 3 Scope .....	22
1.5.4 Chapter 4 Scope .....	22
1.5.5 Chapter 5 Scope .....	23
<b>2. Sn–Bi–Sb Alloys as Anode Materials for Sodium Ion Batteries ...</b>	<b>24</b>
2.1 Introduction.....	24

2.2 Results and Discussion .....	26
2.3 Conclusions.....	46
2.4 Experimental Section .....	46
2.4.1 Materials and Equipment.....	46
2.4.2 Electrode Preparation and Battery Assembly .....	47
2.4.3 Electrochemical Testing.....	49
2.4.4 Characterization.....	49
<b>3. <math>\beta</math>-SnSb for Sodium Ion Battery Anodes: Phase Transformations Responsible for Enhanced Cycling Stability Revealed by In-situ TEM .....</b>	<b>50</b>
3.1 Introduction.....	50
3.2 Results and Discussions.....	51
3.3 Conclusions.....	63
3.4 Experimental Details.....	65
3.4.1 Materials and Equipment.....	65
3.4.2 Electrode Preparation and Electrochemical Testing .....	65
3.4.3 Microstructural Characterization .....	66
3.4.4 In-situ TEM.....	67
3.4.5 Calculations.....	68
<b>4. Adhesion and Surface Layers on Silicon Anodes Suppress Formation of Both c-Li<sub>3.75</sub>Si and the Solid Electrolyte Interphase... 70</b>	<b>70</b>
4.1 Introduction.....	70
4.2 Results and Discussions.....	71
4.3 Conclusions.....	85
4.4 Experimental Details.....	85

4.4.1 Materials and Equipment .....	85
4.4.2 Electrode Preparation and Battery Assembly .....	86
4.4.3 Electrochemical Testing.....	87
4.4.4 Characterization .....	87
4.4.5 In-operando Neutron Reflectometry Experiment .....	88
<b>5. Thesis Summary and Outlook.....</b>	<b>89</b>
5.1 Summary .....	89
5.1.1 Chapter 1 .....	89
5.1.2 Chapter 2.....	89
5.1.3 Chapter 3.....	90
5.1.4 Chapter 4.....	91
5.2 Proposed Research Directions .....	91
5.2.1 In-situ TEM Study of the Sn <sub>10</sub> Bi <sub>10</sub> Sb <sub>80</sub> Alloy Electrode .....	91
5.2.2 Exploration of Ternary and Quaternary Alloys for Sodium-ion Batteries	93
5.2.3 The Maximum Length Scale of the Separation Between Sn and Sb to Enable the Formation of $\beta$ -SnSb.....	94
5.2.4 Investigation of the Formation of Solid Electrolyte Interphase via In- operando Neutron Reflectometry.....	95
<b>References.....</b>	<b>97</b>

# List of Tables

<b>Table 1.1</b> Comparison of Sodium and Lithium Elements. <sup>7-10</sup> .....	3
<b>Table 1.2.</b> Comparison of Sodiation Potential, Theoretical Capacity, and Volume Change of Elemental Sn, Sb, Ge, Si, P, and TiO <sub>2</sub> . <sup>21-24</sup> The theoretical capacity was calculated based on the desodiated state. ....	8
<b>Table 1.3.</b> Comparison of Delithiation Potential, Theoretical Capacity, and Volume Change of Graphite and Silicon. ....	19
<b>Table 2.1.</b> Comparison Between Maximum Measured Capacities and Maximum Theoretical Capacities Based on a Rule of Mixtures Calculation for Each Composition. ....	27
<b>Table 2.2.</b> Phases Present in All As-deposited Films and Corresponding Cycled Films, as Determined by XRD. ....	29
<b>Table 2.3.</b> Grain Sizes of All Phases in As-deposited Films (As Determined by XRD Using the Scherrer Equation). ....	31
<b>Table 2.4.</b> Grain Sizes of All Phases after 100 Constant Current Charge/Discharge Cycles. ....	32
<b>Table 2.5.</b> Peak Fit Parameters dQ/dV Curves of Pure Sb Films. ....	39
<b>Table 2.6.</b> Peak Fit Parameters dQ/dV Curves of Sn <sub>10</sub> Bi <sub>10</sub> Sb <sub>80</sub> Films. ....	42
<b>Table 2.7.</b> Average Weight and Standard Deviation for Each Composition Based on 6 Different Samples. ....	48
<b>Table 2.8.</b> Sample Compositions of As-deposited Alloy Electrodes, Derived from XPS Spectra. ....	49
<b>Table 3.1.</b> Grain Sizes Measured by XRD via the Scherrer Equation for As-deposited Films and the Same Films After 150 Cycles of Electrochemical Battery Testing. ....	63
<b>Table 4.1.</b> Theoretical Specific Capacity of Each Sample Prepared in This Work. ..	87

# List of Figures

<b>Figure 1.1.</b> Gravimetric energy density of various rechargeable batteries. ....	2
<b>Figure 1.2.</b> (a) Selected area electron diffraction (SAED) patterns of Sn particles at different sodiation states obtained in the in-situ TEM study and schematic illustration of its structure and phase evolution, (b) specific capacity vs cycle number of elemental Sn film. Reproduced and adapted with permission from reference 20 (Copyright 2012 American Chemical Society) and reference 19 (Copyright 2017 Royal Society of Chemistry).....	9
<b>Figure 1.3.</b> Cycling performance of (a) CoSn <sub>2</sub> and FeSn <sub>2</sub> alloy, (b) Cu <sub>2</sub> Sb nanoparticles, and (c) FeSb <sub>2</sub> . Reproduced and adapted with permission from reference 55 (Copyright 2016 The Electrochemical Society), reference 46 (Copyright 2013 American Chemical Society) and reference 47 (Copyright 2015 Elsevier B.V.).....	10
<b>Figure 1.4.</b> Cycling performance of (a) SnSb alloy, (b) Bi–Sb alloy, (c) Sn–Ge alloy, and (d) Sb–Si alloy. Reproduced and adapted with permission from reference 30 (2016 The Royal Society of Chemistry), reference 50 (Copyright 2015 American Chemical Society), and reference 51 (Copyright 2014 American Chemical Society), and 61 (Copyright 2019 American Chemical Society).....	11
<b>Figure 1.5.</b> Galvanostatic voltage profile of Sn thin film electrode tested using Na foil as the counter and reference electrode. The testing current density is 200 mAh/g. ....	12
<b>Figure 1.6.</b> Phase diagram of Na–Sn. Reproduced with permission from reference 62 (Copyright 2016 ASM International).....	13
<b>Figure 1.7.</b> Cycling performance of (a) Sn and Sn–Cu alloy, (b) Sn–Sb alloy, (c) Sn–Ge–Sb alloy. (d) TEM micrograph and corresponding FFT of Sn <sub>50</sub> Ge <sub>25</sub> Sb <sub>25</sub> alloy. Reproduced and adapted with permission from reference 48 (Copyright 2013 American Chemical Society), reference 52 (Copyright 2013 Elsevier B.V.), and reference 49 (Copyright 2014 American Chemical Society).....	14
<b>Figure 1.8.</b> Phase diagram of Na–Sb. Reproduced with permission from reference 62 (Copyright 2016 ASM International).....	15
<b>Figure 1.9.</b> Galvanostatic voltage profile of a Sb thin film electrode tested using Na foil as the counter and reference electrode. The testing current density is 200 mAh/g. ....	15
<b>Figure 1.10.</b> Specific capacity and corresponding Coulombic efficiency vs cycle number of (a) bulk Sb, (b) Zn <sub>4</sub> Sb <sub>3</sub> alloys prepared with a different deposition time, (c) nanoporous Bi–Sb alloys, pure Bi and pure Sb, and (e) nanoporous Bi <sub>2</sub> Sb <sub>6</sub> alloy. (d) Rate capability of the nanoporous Bi–Sb alloys. Reproduced and adapted with permission from reference 67 (Copyright 2012 American Chemical Society),	

reference 45 (Copyright 2015 American Chemical Society), and reference 70 (Copyright 2018 American Chemical Society).....	17
<b>Figure 1.11.</b> Schematic illustration of the main degradation mechanism of the Si anode. Reproduced with permission from reference 83 (Copyright 2016 Macmillan Publishers Limited).....	20
<b>Figure 2.1.</b> Specific capacity versus cycling number of (a) Sn-rich compositions (b) Bi-rich compositions (c) Sb-rich compositions. Coulombic efficiencies also are depicted for the Sb-rich compositions. (d) Rate tests and corresponding coulombic efficiency of Sb-rich compositions.....	26
<b>Figure 2.2.</b> High resolution XPS spectra of Sb3d, Sn3d, and Bi4f of as-deposited thin films for all the alloy compositions investigated in this work.....	27
<b>Figure 2.3.</b> XRD patterns of as-deposited alloy films (top row) and after 100 electrochemical cycles (bottom row). Reference diffraction patterns: Sn (PDF no. 04-004-7747), Bi (PDF no. 00-005-0519), Sb (PDF no. 00-035-0732) and $\beta$ -SnSb (PDF no. 04-014-6042).....	29
<b>Figure 2.4.</b> Average grain sizes of as-sputtered and cycled films, as determined by the Scherrer equation applied to the XRD patterns in Figure 2.3.....	30
<b>Figure 2.5.</b> SEMs of as-deposited elemental films and alloys. (a) Sn, (b) Sn <sub>80</sub> Bi <sub>10</sub> Sb <sub>10</sub> , (c) Sn <sub>50</sub> Bi <sub>25</sub> Sb <sub>25</sub> , (d) Bi, (e) Sn <sub>10</sub> Bi <sub>80</sub> Sb <sub>10</sub> , (f) Sn <sub>25</sub> Bi <sub>50</sub> Sb <sub>25</sub> ; (g) Sb, (h) Sn <sub>10</sub> Bi <sub>10</sub> Sb <sub>80</sub> , (i) Sn <sub>25</sub> Bi <sub>25</sub> Sb <sub>50</sub> . All scale bars are 200 nm. The numbers following the elements represent the molar percent of elements in the film.....	32
<b>Figure 2.6.</b> SEM micrographs of the cycled elemental films and alloys. (a) Sn (b) Sn <sub>80</sub> Bi <sub>10</sub> Sb <sub>10</sub> , (c) Sn <sub>50</sub> Bi <sub>25</sub> Sb <sub>25</sub> ; (d) Bi, (e) Sn <sub>10</sub> Bi <sub>80</sub> Sb <sub>10</sub> , (f) Sn <sub>25</sub> Bi <sub>50</sub> Sb <sub>25</sub> ; (g) Sb, (h) Sn <sub>10</sub> Bi <sub>10</sub> Sb <sub>80</sub> , (i) Sn <sub>25</sub> Bi <sub>25</sub> Sb <sub>50</sub> . Pure Sn and Bi were cycled 50 times, and all other electrodes 100 times. All scale bars are 2 $\mu$ m.....	33
<b>Figure 2.7.</b> Voltage profiles (left) and corresponding dQ/dV plots (right) for (a,b) elemental Sn, (c,d) Sn <sub>80</sub> Bi <sub>10</sub> Sb <sub>10</sub> , (e,f) Sn <sub>60</sub> Bi <sub>20</sub> Sb <sub>20</sub> and (g,h) Sn <sub>50</sub> Bi <sub>25</sub> Sb <sub>25</sub> . .	35
<b>Figure 2.8.</b> Voltage profiles (left) and corresponding dQ/dV plots (right) for (a,b) elemental Bi, (c,d) Sn <sub>10</sub> Bi <sub>80</sub> Sb <sub>10</sub> , (e,f) Sn <sub>20</sub> Bi <sub>60</sub> Sb <sub>20</sub> , (g,h) Sn <sub>25</sub> Bi <sub>50</sub> Sb <sub>25</sub> and (i,j) Sn <sub>33</sub> Bi <sub>33</sub> Sb <sub>33</sub> . ..	36
<b>Figure 2.9.</b> Voltage profiles (a)–(c) and corresponding dQ/dV plots for elemental Sb (a and d), Sn <sub>10</sub> Bi <sub>10</sub> Sb <sub>80</sub> (b and e) and Sn <sub>20</sub> Bi <sub>20</sub> Sb <sub>60</sub> (c and f).....	37
<b>Figure 2.10.</b> Curve fitting of dQ/dV the sodiation/desodiation profiles of pure Sb. (a–c) sodiation curves for cycles 2, 10, and 35. (d–f) desodiation curves for cycles 2, 10, and 35.....	38

<b>Figure 2.11.</b> Curve fitting of $dQ/dV$ the sodiation/desodiation profiles of Sn <sub>10</sub> Bi <sub>10</sub> Sb <sub>80</sub> . (a–c) sodiation curves for cycles 2, 10, and 50. (d–f) desodiation curves for cycles 2, 10, and 50.....	41
<b>Figure 2.12.</b> Specific Na storage capacity versus cycle number of the Si substrate used in this study. (a) Normalized to the average weight of a 100 nm thin film used in this study. (b) Normalized to the surface area of the substrate. ....	48
<b>Figure 3.1.</b> (a) Simulated diffraction patterns of $\beta$ -SnSb alloy, indicating that $\beta$ -SnSb has a cubic rocksalt crystal structure. (b) Indexed X-ray diffraction patterns of the as-deposited 100 nm $\beta$ -SnSb alloy film and the Sn/Sb and Sb/Sn bilayer films.....	52
<b>Figure 3.2.</b> Galvanostatic charge–discharge curves of co-sputtered SnSb and bilayer Sn/Sb and Sb/Sn at cycles (a) 2, (b) 10, and (c) 50. (d) Associated cycling performance and CEs, which also include baseline elemental films of Sn and Sb as well as a trilayer Sn/Si(2 nm)/Sb film. All batteries were tested at 200 mA/g.....	52
<b>Figure 3.3.</b> Galvanostatic sodiation-desodiation voltage profiles of (a) Sn, (b) Sb, and (c) Sn/Si(2 nm)/Sb films at cycles 2, 10, and 50. ....	53
<b>Figure 3.4.</b> (a) Indexed XRD pattern of the SnSb film after 45 cycles in the desodiated state showing the presence of only $\beta$ -SnSb, without either Sn or Sb peaks being present. (b) Indexed XRD patterns of SnSb, Sn/Sb, and Sb/Sn after 150 cycles, indicating the even after extensive cycling $\beta$ -SnSb is still present in the desodiated state, although the crystalline Sn phase is also present. The broad peak at $2\theta \approx 57^\circ$ is from the (311) reflection of the Si substrate. This peak is broadened because the sample is close but slightly out of the Bragg condition, which is due to the in-plane rotation of the single-crystal substrate. ....	54
<b>Figure 3.5.</b> In situ TEM analysis of the sodiation–desodiation of a co-sputtered SnSb film during the first cycle. (a) Bright-field micrographs and (b) associated measured electron diffraction patterns as well simulations during sodiation. (c,d) Same analyses during desodiation.....	55
<b>Figure 3.6.</b> (a) Volume changes of SnSb film during in-situ (de)sodiation as a function of time. Sodiation is done potentiostatically at -0.5 V and desodiation at +5 V. (b) BF-TEM micrograph of an in-situ sodiated SnSb film, with the image rotated so that the wire axis is parallel to the vertical axis. Overlaid on the image is the average image intensity along the vertical direction. (c) Schematic of geometry assumed for volume calculations of the SnSb film.....	56
<b>Figure 3.7.</b> (a) BF-TEM of Sn/Sb multilayer (25 nm/25 nm) in the as-deposited state, with a single Sn particle marked in red. (b) The same particle marked in red after 65 min of in-situ sodiation. ....	57
<b>Figure 3.8.</b> Azimuthally averaged in situ electron diffraction patterns (Figure 3.5) of the SnSb during (a) sodiation and (b) desodiation.....	58

<b>Figure 3.9.</b> HRTEM analysis of the SnSb film after four in situ sodiation–desodiation cycles. (a) BF-TEM of the film and (b) corresponding HRTEM showing nanocrystallites, which are attributed to $\beta$ -SnSb.....	59
<b>Figure 3.10.</b> In situ TEM analysis of a co-sputtered SnSb film during multicycle sodiation–desodiation. Each sodiation micrograph is acquired after 60 min at -0.5 V and desodiation micrographs after 60 min at +5.0 V. Corresponding SAED patterns and relevant simulations are shown below each micrograph.....	60
<b>Figure 3.11.</b> In situ TEM analysis of the sodiating–desodiating Sb(top)/Sn(bottom) bilayer film. Figures (a) and (b) show bright field micrographs and associated experimental and simulated SAED patterns during sodiation done potentiostatically at -0.5 V. Figures (c) and (d) show these results during desodiation, done potentiostatically at +5.0 V.....	61
<b>Figure 3.12.</b> Azimuthally averaged in situ electron diffraction patterns (Figure 3.11) of the Sb(top)/Sn(bottom) film during first (a) sodiation and (b) desodiation. Each profile is independently normalized.....	61
<b>Figure 3.13.</b> In situ TEM analysis of the sodiating–desodiating Sn(top)/Sb(bottom) bilayer film. Figures (a) and (b) shows bright field micrographs and associated experimental and simulated SAED patterns during sodiation done potentiostatically at -0.5 V. Figures (c) and (d) show these results during desodiation, done potentiostatically at +5.0 V.....	62
<b>Figure 3.14.</b> Azimuthally averaged in-situ electron diffraction patterns (Figure 3.13) of the bilayer Sn(top)/Sb(bottom) during first (a) sodiation and (b) desodiation. Each profile is independently normalized.....	62
<b>Figure 4.1.</b> XRD patterns of as-deposited films on (a) Cu substrate and (b) Si substrate.....	72
<b>Figure 4.2.</b> SEM images of as-deposited (a) Si, (b) Ni/Si, (c) Ni/Si <sub>85</sub> Ti <sub>15</sub> , (d) Ni/Si <sub>85</sub> Ti <sub>15</sub> /C, (e) Ni/Si <sub>85</sub> Ti <sub>15</sub> /10TiO <sub>2</sub> , and (d) Ni/Si <sub>85</sub> Ti <sub>15</sub> /5TiO <sub>2</sub> electrodes.....	73
<b>Figure 4.3.</b> SEM micrographs of delithiated (a) Si, (b) Ni/Si, (c) Ni/Si <sub>85</sub> Ti <sub>15</sub> , (d) Ni/Si <sub>85</sub> Ti <sub>15</sub> /C, (e) Ni/Si <sub>85</sub> Ti <sub>15</sub> /10TiO <sub>2</sub> , and (f) Ni/Si <sub>85</sub> Ti <sub>15</sub> /5TiO <sub>2</sub> electrodes after 10 cycles.....	73
<b>Figure 4.4.</b> Specific capacity (a,d), associated Coulombic efficiency (b,e), and capacity retention (c,f) vs cycle number. The inset in (b,e) shows the CE for the first five cycles. (a–c) were tested first at a constant current step with a rate of 0.4 C, followed by a constant voltage step of 5 mV and 1.0 V for lithiation and delithiation, respectively. The current limit for constant voltage steps is 0.01 C. (d-f) were tested with only a CC step under the same rate.....	74
<b>Figure 4.5.</b> Specific capacity and associated Coulombic efficiency vs cycle number for the Ni/Si <sub>85</sub> Ti <sub>15</sub> /10TiO <sub>2</sub> electrode tested at 2 or 4 under both CC and CCCV	

protocol. The samples were tested first at 0.1 C for three cycles, then the testing rate was increased to 2 or 4 C. For the CV step, the limit current is one-tenth of the rate of the CC step, (e.g., 0.2 C for 2 C at the CC step)..... 76

**Figure 4.6.** Differential capacity vs voltage of (a) Si, (b) Ni/Si, (c) Ni/Si<sub>85</sub>Ti<sub>15</sub>, (d) Ni/Si<sub>85</sub>Ti<sub>15</sub>/C, (e) Ni/Si<sub>85</sub>Ti<sub>15</sub>/10TiO<sub>2</sub>, and (f) Ni/Si<sub>85</sub>Ti<sub>15</sub>/5TiO<sub>2</sub> electrodes for selected cycles tested at CCCV protocol. The corresponding galvanostatic charge–discharge curves are shown in Figure 4.7. .... 77

**Figure 4.7.** Galvanostatic charge–discharge curves of (a) Si, (b) Ni/Si, (c) Ni/Si<sub>85</sub>Ti<sub>15</sub>, (d) Ni/Si<sub>85</sub>Ti<sub>15</sub>/C, (e) Ni/Si<sub>85</sub>Ti<sub>15</sub>/10TiO<sub>2</sub>, and (f) Ni/Si<sub>85</sub>Ti<sub>15</sub>/5TiO<sub>2</sub> electrodes for selected cycles. The results are tested at CCCV protocol and associated with the results presented in Figure 4.6. .... 77

**Figure 4.8.** Curve fitting of the delithiation branch in the  $dQ/dV$  plots of the Ni/Si electrode for cycle 30, 35, 40, and 90. .... 78

**Figure 4.9.** The normalized area of the Li<sub>3.75</sub>Si peak and capacity retention vs cycle number of Si, Ni/Si, Ni/Si<sub>85</sub>Ti<sub>15</sub>, Ni/Si<sub>85</sub>Ti<sub>15</sub>/C, Ni/Si<sub>85</sub>Ti<sub>15</sub>/10TiO<sub>2</sub>, and Ni/Si<sub>85</sub>Ti<sub>15</sub>/5TiO<sub>2</sub> electrodes. .... 79

**Figure 4.10.** (a) Cumulative relative irreversible capacity due to the formation of SEI vs cycle number. (b) Relative composition of SEI in the outer 10 nm after 10 cycles of lithiation–delithiation. The results were calculated based on the XPS spectra of F 1s, C 1s, and Li 1s. All samples were tested under CCCV protocol. .... 81

**Figure 4.11.** XPS spectra and Voigt function fits of the SEI composition, in the C 1S, F 1s, P 2p, Li 1s, and O 1s regions. .... 83

**Figure 4.12.** (a) Schematic sketch and (b) optical image of the in operando NR experimental setup. .... 84

**Figure 4.13.** Voltage profiles of (a) Ni/Si<sub>85</sub>Ti<sub>15</sub> electrode tested at 0.4 C, and (b) Ni/Si<sub>85</sub>Ti<sub>15</sub>/10TiO<sub>2</sub> electrode tested at 0.1 C for the first three cycles. The samples were tested using the customized electrochemical cell, as shown in Figure 4.12. .... 84

**Figure 4.14.** Neutron reflectivity vs  $Q$  for sample Ni/Si<sub>85</sub>Ti<sub>15</sub> and Ni/Si<sub>85</sub>Ti<sub>15</sub>/10TiO<sub>2</sub> electrodes at different times of cycling tests. .... 85

**Figure 5.1.** In situ TEM analysis of a 100-nm Sb film deposited on the TiN coated Ge nanowires. (a) BF-TEM micrograph of the film in the fully sodiated state after around 10 h and (b) in the desodiated state. Corresponding high-angle annular dark-field (HAADF) micrographs (c) and energy-dispersive X-ray spectroscopy (EDX) mapping of Sb (d) in the desodiated state. Reproduced with permission from reference 175 (Copyright 2015 American Chemical Society)..... 92

**Figure 5.2.** (a) Indexed XRD pattern of as-desodiated Sn/Si/Sb trilayer films. Specific capacity vs cycle number of (b) Sn/Si/Sb trilayer films and (c) Sb/Sn bilayer films.

Reproduced and adapted with permission from reference 210 (Copyright 2019  
American Chemical Society). ..... 94

# List of Schemes

<b>Scheme 1.1.</b> Illustration of the configuration and working principle of typical lithium-ion batteries.....	4
<b>Scheme 1.2.</b> Illustration of the configuration and working principle of typical sodium-ion batteries.....	5
<b>Scheme 3.1.</b> Schematic illustration of the proposed phase transition of $\beta$ -SnSb during the sodiation–desodication cycle. ....	64
<b>Scheme 4.1.</b> Schematic illustration of the electrodes prepared via magnetron sputtering.....	71
<b>Scheme 5.1.</b> Scheme illustration of the configuration of the platform for in-situ TEM experiments. ....	93
<b>Scheme 5.2.</b> Scheme illustration of the (a) configuration of the operando cell and (b) working electrode during neutron measurement. Reproduced and adapted with permission from reference 209 (Copyright 2018 Elsevier B.V.).....	96

## List of Abbreviations

CE	Coulombic Efficiency
DEC	Diethyl Carbonate
EC	Ethylene Carbonate
EDX	Energy Dispersive X-ray Spectroscopy
FEC	Fluoroethylene Carbonate
HAADF	High-angle Annular Dark-field
HRTEM	High Resolution Transmission Electron Microscopy
LIBs	Lithium-ion Batteries
SAED	Selected Area Electron Diffraction
SEI	Solid Electrolyte Interphase
SEM	Scanning Electron Microscopy
SIBs	Sodium-ion Batteries
TEM	Transmission Electron Microscopy
WE	Working Electrode
XPS	X-ray Photoelectron Spectroscopy
XRD	X-ray Diffraction

# Chapter 1\*

## Introduction

### 1.1 Why Lithium-ion and Sodium-ion Batteries?

#### 1.1.1 Electrical Energy Storage Demand and Challenges

Today, as the world moves rapidly towards an electrified, low carbon world, rechargeable batteries play an ever more important role in the sustainable energy landscape as an energy storage medium for electrical vehicle and grid-level applications. Many renewable energy sources, such as wind and solar, are intrinsically intermittent and thus need energy storage mediums to buffer the mismatch between supply and demand in time and space. Ground transportation, which mainly relies on petroleum, consumes 29% of global energy and produces 25% of CO<sub>2</sub> emissions (according to the International Energy Agency's 2018 report).<sup>1,2</sup> Therefore, switching from petroleum vehicles to electrical vehicles could reduce the CO<sub>2</sub> emission significantly. The global energy storage market that supports renewable energies and electric vehicles increased dramatically in recent years and is expected to continue growing.<sup>3,4</sup>

Current technologies of rechargeable batteries do not, however, satisfy the increasing requirements of electric vehicle and grid-level applications. High-performance rechargeable batteries with a higher energy density, enhanced cycling stability, and a lower price still need to be developed.

#### 1.1.2 Advantages of Lithium-ion Batteries and Applications

Lithium-ion batteries (LIBs), first commercialized in 1991 by Sony Corp., have many advantages, including high energy density, long cycle life, and low self-discharge,

---

\* Some of the contents of this chapter have been reproduced and/or adapted from the following publications: (1) Xie, H.; Kalisvaart, W. P.; Olsen, B. C.; Luber, E. J.; Mitlin, D.; Buriak, J. M. Sn–Bi–Sb Alloys as Anode Materials for Sodium Ion Batteries. *J. Mater. Chem. A* **2017**, 5 (20), 9661–9670. (2) Xie, H.; Tan, X.; Luber, E. J.; Olsen, B. C.; Kalisvaart, W. P.; Jungjohann, K. L.; Mitlin, D.; Buriak, J. M.  $\beta$ -SnSb for Sodium Ion Battery Anodes: Phase Transformations Responsible for Enhanced Cycling Stability Revealed by In Situ TEM. *ACS Energy Lett.* **2018**, 3 (7), 1670–1676.

compared to other battery family members, such as lead–acid and nickel–metal hydride batteries.<sup>5</sup> As shown in Figure 1.1, the specific energy density of LIBs is the highest among different types of rechargeable batteries, nearly five times that of the lead–acid battery and twice that of the nickel–metal hydride batteries. Over the last three decades, LIBs have become the mainstay in commercial markets for portable electronic devices. In recent years, the applications of LIBs also have been expanded to electric vehicle and grid-level applications. For instance, Tesla’s electric vehicles have attracted a lot of interest since 2012. In 2017, Tesla installed the largest grid-scale LIBs in South Australia, with a storage capacity of 129 MWh and a power of 100 MW.<sup>6</sup>

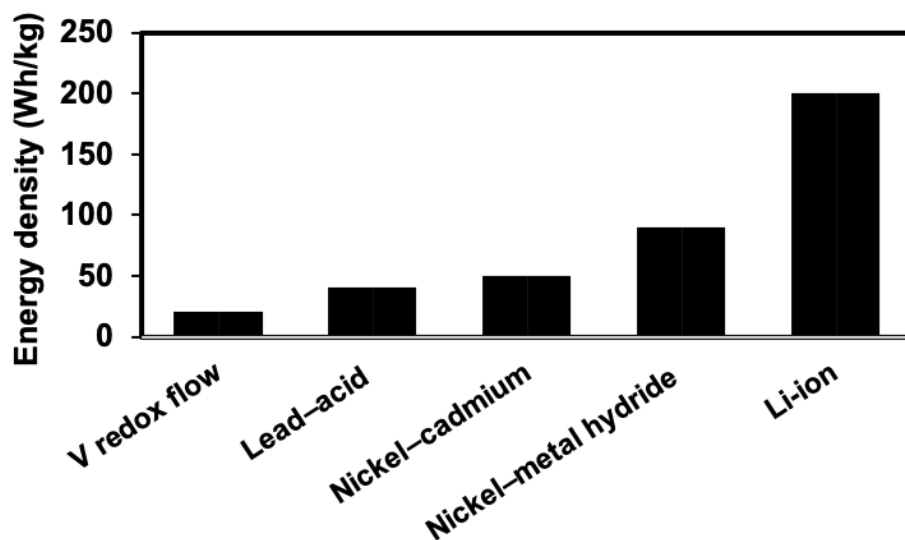


Figure 1.1. Gravimetric energy density of various rechargeable batteries.<sup>5</sup>

### 1.1.3 Interests of Sodium-ion Batteries and Potential Applications

The motivation to work on sodium-ion batteries (SIBs) is due to the abundance of sodium source in the earth’s crust, which is over 1000 times higher than that of lithium, as shown in Table 1.1. Unlike lithium whose known reserves are located mainly in the lithium triangle of South America (Argentina, Bolivia, and Chile, ~44–64%),<sup>7,8</sup> sodium is distributed over the earth’s entire surface. Thus, the cost of sodium salts is significantly less than their lithium equivalents; for example,  $\text{Na}_2\text{CO}_3$  is ~0.50 US\$/kg and  $\text{Li}_2\text{CO}_3$  is ~6.5 US\$/kg. In addition, there are many similarities with

respect to the working principles and design strategies between SIBs and LIBs, which could enable the rapid development of SIBs as a result of the ample experience gained in LIBs. Capitalizing on the abundance of sodium to develop sodium ion batteries (SIBs) will lead to diversification of battery technologies, reduce reliance on a potentially more limited and costly element, and enable widespread deployment of grid-scale battery applications.

**Table 1.1** Comparison of Sodium and Lithium Elements.<sup>7-10</sup>

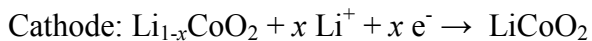
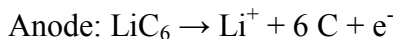
	Na	Li
Abundance in the earth's crust (mg/kg)	23600	20
Distribution	Everywhere	~44–64 % in South America
E° vs. SHE (V)	-2.71	-3.04
Cost of carbonate (\$/kg)	0.50	~6.5

Note: E° = Standard potential of the electrode; SHE = Standard hydrogen electrode.

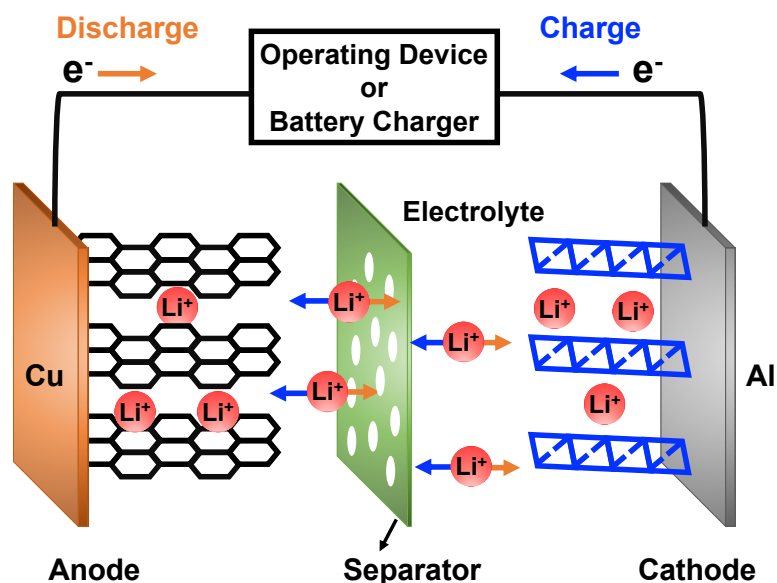
## 1.2 Basic Concept of Batteries and Evaluation Criteria for Battery Electrode Materials

### 1.2.1 Working Principles of Lithium-ion and Sodium-ion Batteries

A rechargeable battery is a device that reversibly converts electrical energy to chemical energy. Typical LIBs consist of four components, including an anode, cathode, separator, and electrolyte, as shown in Scheme 1.1. A typical anode of LIBs is graphite coated on a copper current collector; a cathode is composed of lithium transition metal oxides/lithium iron phosphates coated on aluminum foil. The electrolyte is a lithium salt dissolved in organic solvents, and the separator is usually porous polymers to prevent a short-circuit. When the battery is discharging, an oxidation reaction occurs at the anode to produce electrons and Li ions, and a reduction reaction occurs at the cathode to accept the electrons and Li ions. An example of the reaction during discharge is shown below:

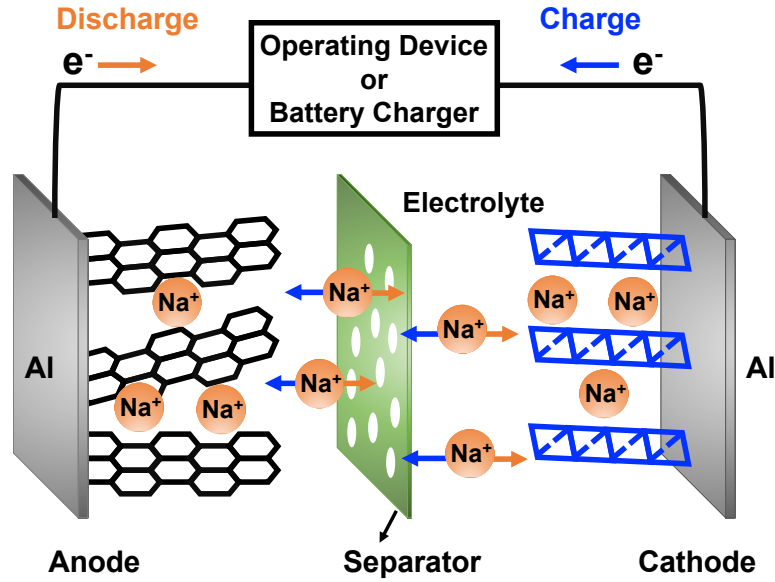


The generated electrons at the anode move through the external circuit into the cathode to power electronic devices, and the  $\text{Li}^+$  transport through the ionic electrolyte, which is conductive but electrically insulative, into the cathode to complete the circuit. During charging, the reaction and moving directions of the electrons and  $\text{Li}^+$  are reversed.



**Scheme 1.1.** Illustration of the configuration and working principle of typical lithium-ion batteries.

The structure and working principle of SIBs are basically the same as LIBs, and the major difference is the use of sodium ions instead of lithium ions as the current carrier in the internal circuit, as shown Scheme 1.2. In addition, SIBs can use aluminum as the current collector for both cathode and anode because sodium does not react with aluminum at low voltages. This could further reduce the cost.



**Scheme 1.2.** Illustration of the configuration and working principle of typical sodium-ion batteries.

## 1.2.2 Evaluation Parameters for Electrode Materials

### 1.2.2.1 Gravimetric and Volumetric Capacity

The capacity of an electrode material is the quantity of electric charge it can store.

The capacity of electrodes and the working voltage of a battery determine the total energy the battery it can store. Gravimetric (specific) and volumetric capacity are the capacity per unit mass and volume, respectively, as expressed below:

$$Q_g = \frac{Q}{m} = \frac{xF}{3.6M_w}$$

$$Q_v = \frac{Q}{v} = \frac{xF}{3.6V_m} = Q_g * \rho$$

where  $Q_g$  is gravimetric (specific) capacity,  $Q_v$  is volumetric capacity,  $Q$  is the capacity of an electrode,  $m$  is the mass of the electrode,  $v$  is the volume of the electrode,  $x$  is the amount of  $Li^+$  that can be stored in the electrode materials ( $Li_xA$ ),  $F$  is Faraday's constant,  $M_w$  is the molar mass,  $V_m$  is the molar volume, and  $\rho$  is the density of the electrode.

The gravimetric and volumetric capacity of electrodes are important parameters for evaluating the energy density of a battery. From a theoretical perspective, electrode materials with a high gravimetric and volumetric capacity are favored to obtain a high energy density battery.

### **1.2.2.2 Voltages**

As stated above, the voltage of a battery is another important parameter that determines its energy and energy density. The voltage of a battery is the potential difference between the anode and cathode. Since the voltage of a battery is proportional to the energy and energy density of a battery, anode and cathode materials with lower and higher potential, respectively, are preferred. However, their potential must be within the potential window of the electrolyte, otherwise, the electrolyte will decompose dramatically. In addition, the potential of anode materials for lithium-ion and sodium-ion batteries must be higher than that of lithium (-3.04 V vs SHE) and sodium (-2.7 vs SHE) metal respectively, otherwise lithium and sodium dendrites will grow and cause safety issues. In research, the potential of the electrode material often is measured using Li or Na metal as the reference electrode.

### **1.2.2.3 Power**

The power of a battery is the product of the voltage and current it can output, both of which are determined mainly by the electrode materials. The maximum power that a battery can supply is significant, especially for applications requiring high power like the acceleration of electric vehicles. Electrode materials often are tested in a series of high current rates to evaluate its power capability.

### **1.2.2.4 Coulombic Efficiency**

Coulombic efficiency (CE) is the percentage ratio of the charges (electrons) output ( $Q_o$ ) from an electrode during a reduction reaction to the charges (electrons) input ( $Q_i$ ) into the electrode during an oxidation reaction, as expressed below:

$$CE = \frac{Q_o}{Q_i} * 100\%$$

CE and voltage efficiency determine the energy conversion efficiency of a battery. In addition, CE is an indicator of the reversibility of the redox reactions of the electrode material and growth of the solid electrolyte interphase (SEI).

#### **1.2.2.5 Cycle life**

The cycle life of a battery is used to evaluate its long term stability during repeated charge/discharge cycles. The cycle life in industry usually is defined as the number of full charge/discharge cycles a battery completes when its capacity drops to 80% of its initial value. In fundamental studies, the cycle life often is described as the capacity retention vs cycle numbers.

### **1.3 High Capacity Main Group Alloying Anodes for Sodium-Ion Batteries**

#### **1.3.1 Overview of High Capacity Alloying Anodes**

Although Na also reacts with a wide range of transition metal oxides, their average sodiation/desodiation potentials tend to be significantly lower than for their reactions with Li.<sup>11-13</sup> In order to compete with LIB terms of energy density, novel cathode materials, such as  $\text{Na}_3\text{V}_2(\text{PO}_4)_3$ , exhibiting a long voltage plateau near 3.5 V vs  $\text{Na}/\text{Na}^+$ , have been developed.<sup>14</sup> On the anode side, graphite, the anode of choice for commercial LIB, also needs to be replaced as it barely reacts with Na.<sup>15</sup> Some so-called hard carbons have capacities in excess of 300 mAh/g, and the best-performing materials are equivalent in capacity to Li in graphite at  $\sim 350$  mAh/g.<sup>16-18</sup> However, in order to make further gains in the energy density of the battery, anode materials with higher capacities are desirable.

Several main group elements, including Sn, Sb, P, Ge, and Si, that alloy with sodium are attractive candidates because of their high theoretical capacity and low redox potential vs  $\text{Na}/\text{Na}^+$ . Unlike intercalation anode materials, such as  $\text{TiO}_2$ , the atomic framework of alloying materials does not constrain the reaction, so alloying materials usually have a high theoretical capacity, as shown in Table 1.2. However,

since the alloying reaction involves the breaking of bonds and rearrangement of host atoms, alloying anodes also exhibit significant changes in structure and volume upon sodiation (Table 1.2). Such a dramatic change will lead to fracture and pulverization of the electrode, unstable SEI, and loss of electrical contact of active materials, resulting in a poor cycle life. For example, as shown in Figure 1.2, full sodiation of elemental Sn involves a volume change of 420%, and the galvanostatic charge/discharge test of elemental Sn film prepared by sputtering shows dramatic capacity degradation after only ten charge/discharge cycles.<sup>19,20</sup>

**Table 1.2.** Comparison of Sodiation Potential, Theoretical Capacity, and Volume Change of Elemental Sn, Sb, Ge, Si, P, and TiO<sub>2</sub>.<sup>21-24</sup> The theoretical capacity was calculated based on the desodiated state.

Materials	Sn	Sb	Ge	Si	P	TiO <sub>2</sub>
Average sodiation potential (V vs Na/Na <sup>+</sup> )	≈0.20	≈0.60	≈0.30	≈0.50	≈0.40	≈1.5
Fully sodiated phase	Na <sub>15</sub> Sn <sub>4</sub>	Na <sub>3</sub> Sb	Na <sub>1.56</sub> Ge	NaSi/Na <sub>0.75</sub> Si	Na <sub>3</sub> P	NaTiO <sub>2</sub>
Theoretical gravimetric capacity (mAh/g)	847	660	576	954/715	2596	335
Theoretical volumetric capacity (mAh/cm <sup>3</sup> )	6170	4420	3063	2223/1668	5711	1268
Volume change (%)	420	293	205	114	300	12

Note: Volume change = ((volume in fully sodiated state/volume in fully desodiated state) -1) \* 100%

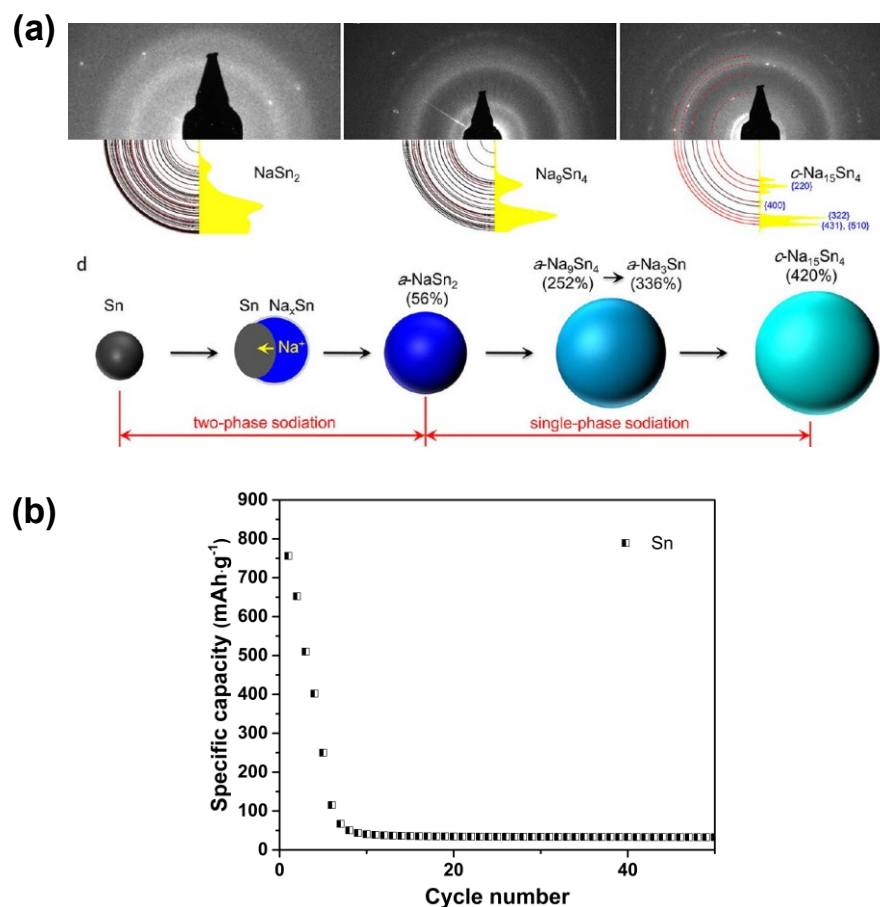


**Figure 1.2.** (a) Selected area electron diffraction (SAED) patterns of Sn particles at different sodiation states obtained in the in-situ TEM study and schematic illustration of its structure and phase evolution, (b) specific capacity vs cycle number of elemental Sn film. Reproduced and adapted with permission from reference 20 (Copyright 2012 American Chemical Society) and reference 19 (Copyright 2017 Royal Society of Chemistry).

Several strategies have been developed to address the issues associated with the large volume change, including nanostructuring,<sup>25–31</sup> surface coating,<sup>32–35</sup> hybrid composite design,<sup>26,36–41</sup> and alloying.<sup>42–52</sup> Among these methods, alloying with active or inactive elements is a simple, effective, and cost-effective way for improving the electrochemical performance of alloying anodes. This method has been applied in commercial rechargeable batteries. For example, in 2005 Sony Corp. developed an Sn-based amorphous anode mainly composed of Sn, Co, and C,<sup>53</sup> and Panasonic announced a new 18650-type lithium ion battery using a Si-based alloy as the anode in 2009.<sup>54</sup>

### 1.3.2 Active–Inactive and All–Active Alloys Anodes

It is worth noting that in this thesis an “alloying anode (for SIBs)” is defined as the anode material that forms alloys with sodium, such as Sn, while an “alloy anode (for SIBs)” is the anode material, which itself is an alloy (e.g., intermetallic SnSb).

Generally, alloy anodes for SIBs can be divided into two categories based on the chemical reactivity of each component to sodium: 1) active–inactive and 2) all–active alloys.

For active–inactive alloys, the component that does not react with sodium will serve as a buffering matrix to maintain the structural integrity and electrical contact of the electrode. Examples include Sn–Co,<sup>55</sup> Sn–Fe,<sup>55</sup> Sn–Al,<sup>56</sup> Sn–Cu,<sup>48</sup> Cu<sub>2</sub>Sb,<sup>46,57</sup> Mo<sub>3</sub>Sb<sub>7</sub>,<sup>43</sup> FeSb<sub>2</sub>,<sup>47,58</sup> and Zn<sub>4</sub>Sb<sub>3</sub>,<sup>45</sup> which generally exhibit improved cycling stability, but at the expense of reducing system capacity, as shown in Figure 1.3.

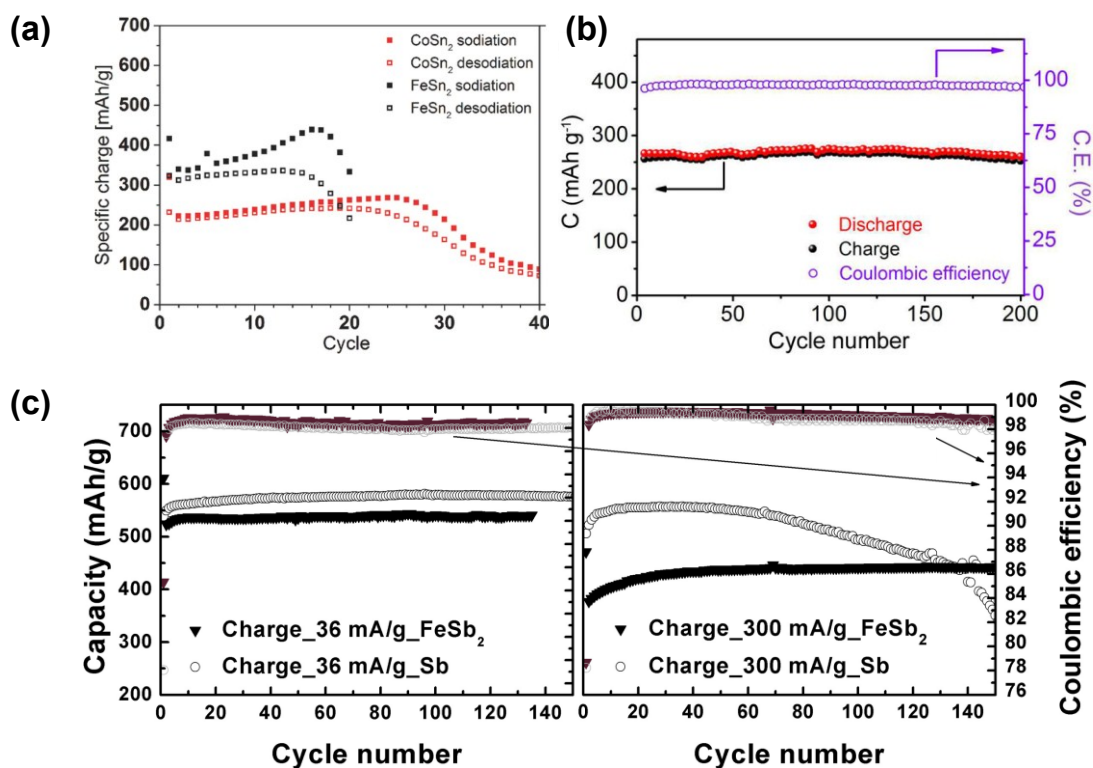


**Figure 1.3.** Cycling performance of (a) CoSn<sub>2</sub> and FeSn<sub>2</sub> alloy, (b) Cu<sub>2</sub>Sb nanoparticles, and (c) FeSb<sub>2</sub>. Reproduced and adapted with permission from reference 55 (Copyright 2016 The Electrochemical Society), reference 46 (Copyright 2017 American Chemical Society) and reference 47 (Copyright 2015 Elsevier B.V).

All-active alloy systems are electrodes where, in principle, all the elements participate in the sodiation reactions. All-active alloys, such as Sn–Sb<sup>30,31,52,59,60</sup>, Sb–Bi<sup>50</sup>, Sn–Ge<sup>51</sup>, Sb–Si,<sup>61</sup> and Sn–Ge–Sb<sup>49</sup>, possess enhanced cycling stability while maintaining high specific capacity (Figure 1.4). The improved cycling stability was ascribed to the amorphization of the electrode materials,<sup>49,51</sup> improved resistance to internal stress, and decreased internal stress.<sup>19,60</sup>

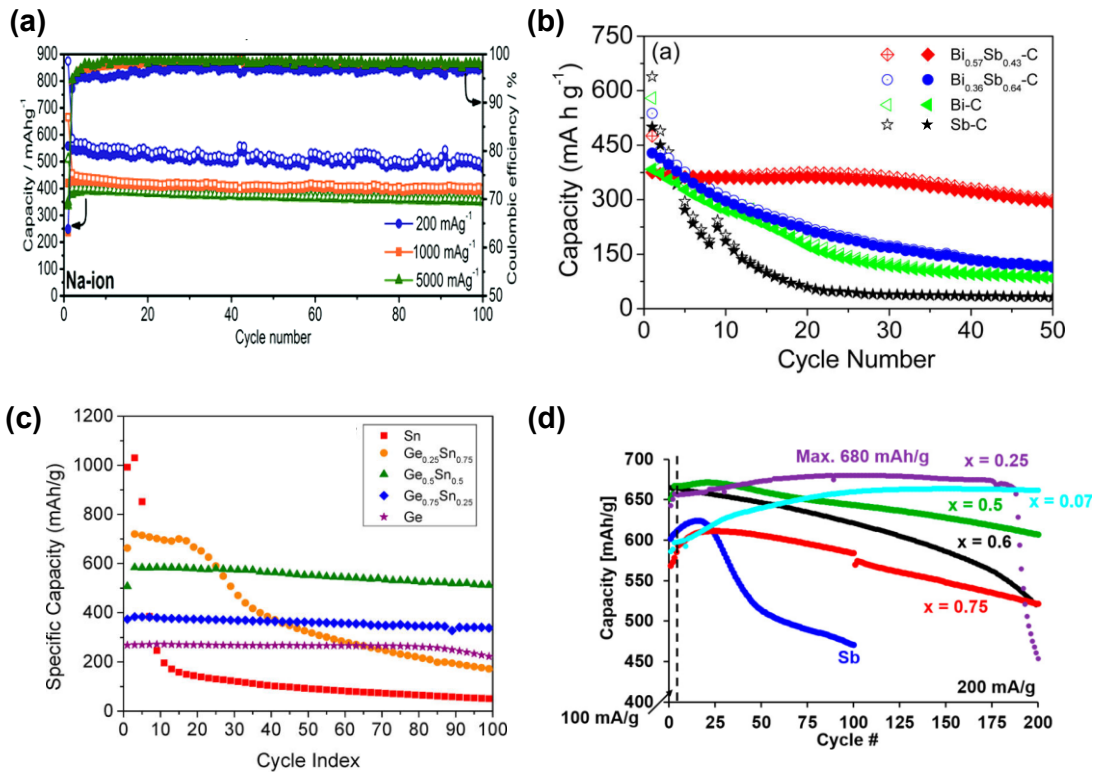
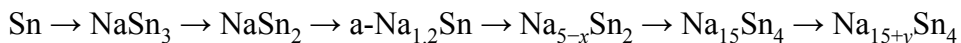


**Figure 1.4.** Cycling performance of (a) SnSb alloy, (b) Bi–Sb alloy, (c) Sn–Ge alloy, and (d) Sb–Si alloy. Reproduced and adapted with permission from reference 30 (2016 The Royal Society of Chemistry), reference 50 (Copyright 2015 American Chemical Society), and reference 51 (Copyright 2014 American Chemical Society), and 61 (Copyright 2019 American Chemical Society).

Among different alloy anodes, Sn-based and Sb-based alloys are probably the most promising ones and are the most widely studied alloy systems for SIBs. Their research progress is summarized below.

### 1.3.3 Sn-based Alloys

Elemental Sn has a theoretical specific capacity of 847 mAh/g and volumetric capacity of 6170 mAh/cm<sup>3</sup>. As shown in Figure 1.5, the galvanostatic voltage profile of Sn during sodiation typically shows four plateaus at around 0.4, 0.18, 0.06, and 0.02 V vs Na/Na<sup>+</sup>, and four plateaus at around 0.20, 0.26, 0.55, and 0.75 V vs Na/Na<sup>+</sup>, indicating at least four phase transition regions. According to the equilibrium phase diagram of Na–Sn, it forms seven phases at room temperature, including NaSn<sub>6</sub>, NaSn<sub>4</sub>, NaSn<sub>3</sub>, NaSn<sub>2</sub>, Na<sub>9</sub>Sn<sub>4</sub>, Na<sub>3</sub>Sn, and Na<sub>15</sub>Sn<sub>4</sub> (Figure 1.6).<sup>62</sup> However, only the terminal phase, Na<sub>15</sub>Sn<sub>4</sub>, has been observed to form in room-temperature SIBs in most studies.<sup>63,20</sup> Recently, Stratford et al. investigated the phase transition of Sn during sodiation by combining density functional theory, pair distribution function analysis, and solid-state NMR spectroscopy and proposed a sodiation mechanism of Sn as the following processes:<sup>64</sup>



They also reported that the final product can store additional Na<sup>+</sup>, resulting in an off-stoichiometry compound (Na<sub>15+y</sub>Sn<sub>4</sub>).

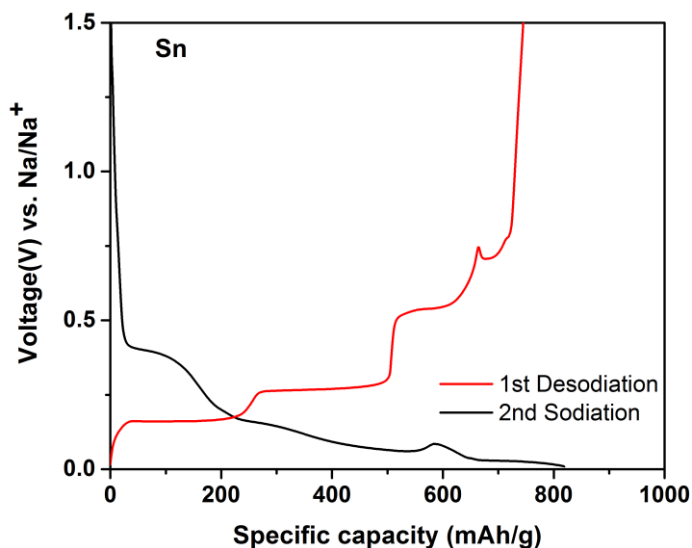


**Figure 1.5.** Galvanostatic voltage profile of Sn thin film electrode tested using Na foil as the counter and reference electrode. The testing current density is 200 mAh/g.

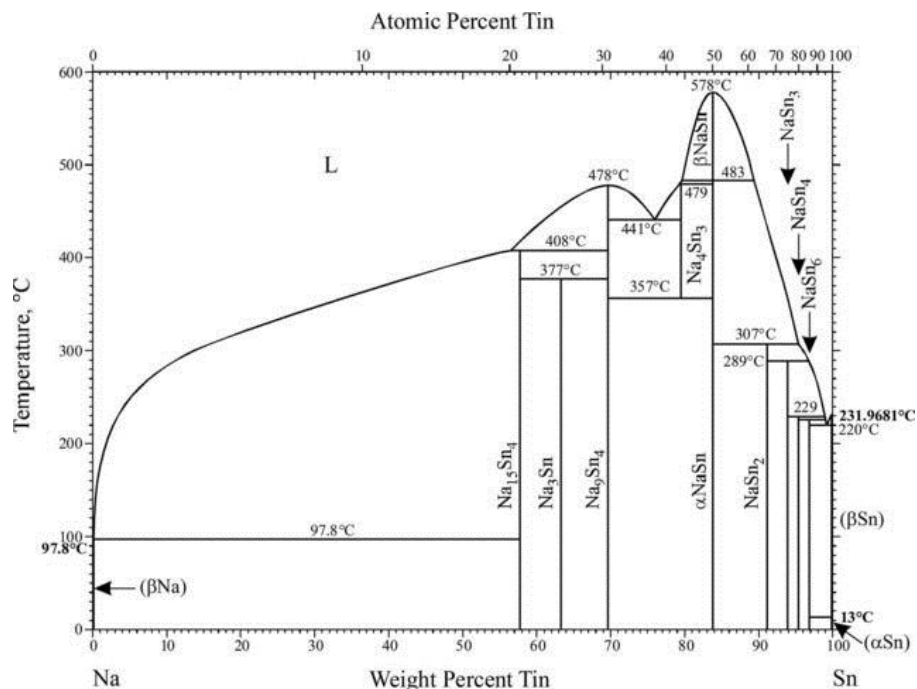


**Figure 1.6.** Phase diagram of Na–Sn. Reproduced with permission from reference 62 (Copyright 2016 ASM International).

As discussed above, the formation of  $\text{Na}_{15}\text{Sn}_4$  corresponds to a volume change of 420%, resulting in poor cycling stability. Alloying with Cu,<sup>48</sup> Co,<sup>55,65</sup> Fe,<sup>55</sup> and Ge<sup>66</sup> has been reported to improve the cycling stability of Sn greatly, but at the cost of reducing about one third to two thirds of the theoretical capacity. As shown in Figure 1.7, intermetallic SnSb also has been shown to improve cyclability of Sn significantly while maintaining a high reversible capacity of over 700 mAh/g, although the experimental capacities are dependent on the testing current rate and electrode composition.<sup>30,31,52,59</sup> Besides these binary alloys, a series of Sn-based ternary alloys has been studied. Some Sn-rich Sn–Ge–Sb alloys, in the work of Farbod et al., exhibit reversible capacities of over 800 mAh/g.<sup>49</sup> The improved capacity retention compared to elemental Sn was attributed to the large amount of an amorphous fraction, which may help to buffer the large volume change and alleviate the fracture and pulverization of the electrode. The Ge in the ternary alloys also was found to sodiate beyond the reported 1:1 Na:Ge ratio of elemental Ge. These results suggest that alloying is an effective method for improving the cycling stability of high capacity anode materials.

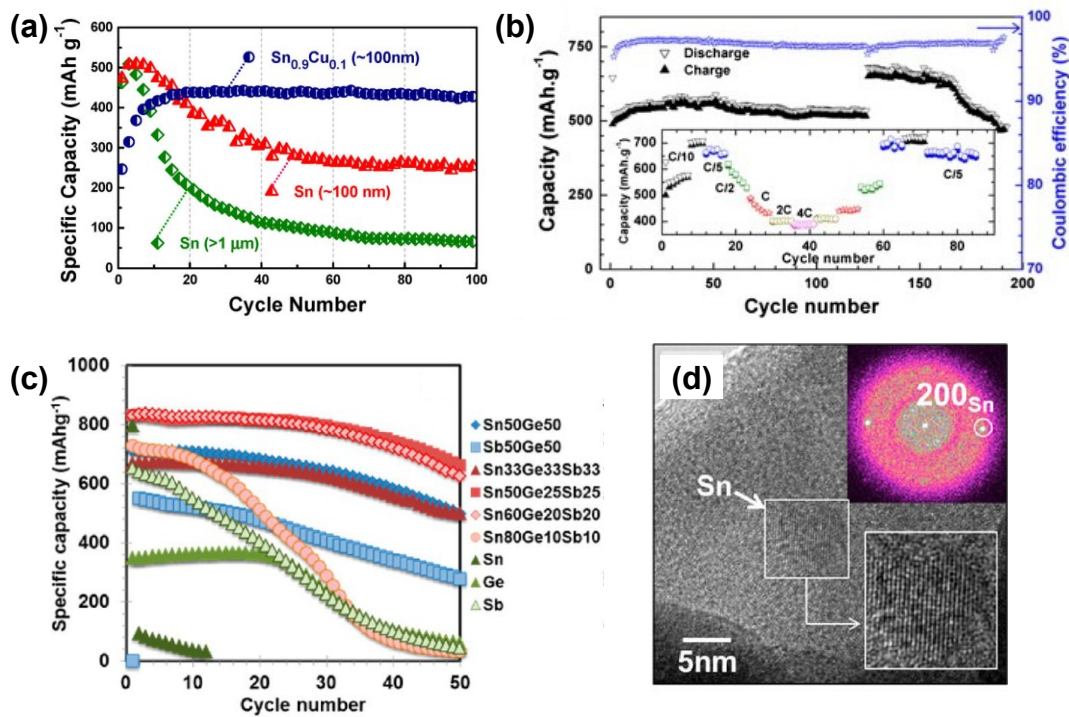


**Figure 1.7.** Cycling performance of (a) Sn and Sn–Cu alloy, (b) Sn–Sb alloy, (c) Sn–Ge–Sb alloy. (d) TEM micrograph and corresponding FFT of Sn50Ge25Sb25 alloy. Reproduced and adapted with permission from reference 48 (Copyright 2013 American Chemical Society), reference 52 (Copyright 2013 Elsevier B.V.), and reference 49 (Copyright 2014 American Chemical Society).

### 1.3.4 Sb-based Alloys

The equilibrium phase diagram of Na–Sb shows two phases at room temperature, including the NaSb and Na<sub>3</sub>Sb (Figure 1.8).<sup>62</sup> The formation of Na<sub>3</sub>Sb corresponds to a theoretical specific capacity of 660 mAh/g and volumetric capacity of 4420 mAh/cm<sup>3</sup>. The galvanostatic voltage profile of Sb exhibits two plateaus at ~0.7 and ~0.6 V (vs Na/Na<sup>+</sup>) during sodiation, and ~0.75 and 0.80 V (vs Na/Na<sup>+</sup>) during desodiation, as shown in Figure 1.9.

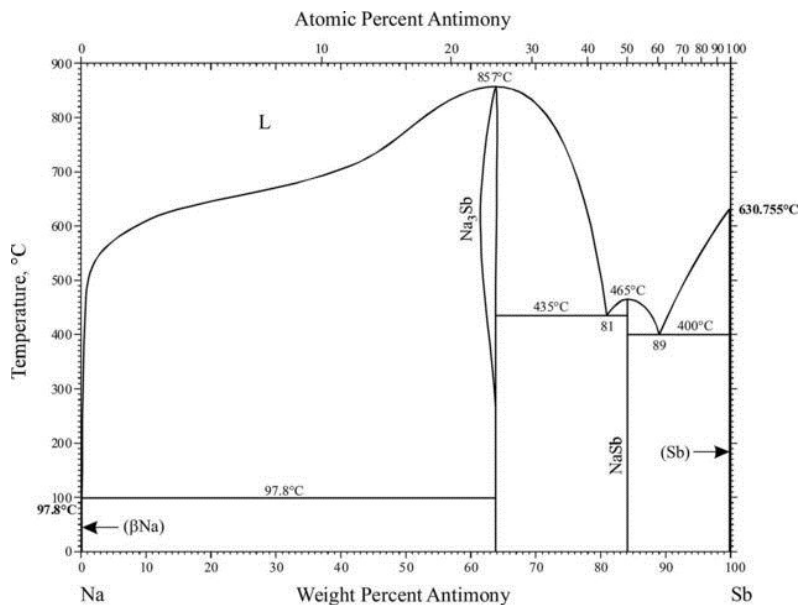


**Figure 1.8.** Phase diagram of Na–Sb. Reproduced with permission from reference 62 (Copyright 2016 ASM International).

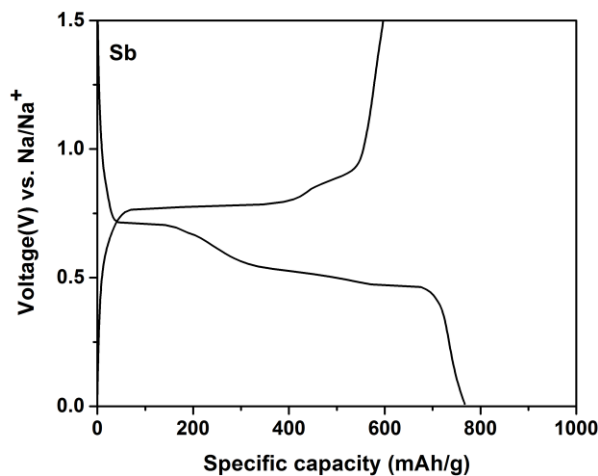
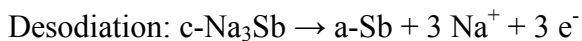
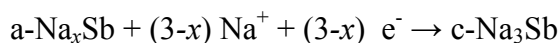


**Figure 1.9.** Galvanostatic voltage profile of a Sb thin film electrode tested using Na foil as the counter and reference electrode. The testing current density is 200 mAh/g.

The sodiation–desodiation mechanism of crystalline Sb (c-Sb) investigated by in-situ XRD studies is summarized as the following (“c-” denotes crystalline and “a-” denotes amorphous or nanocrystalline that are not detectable by XRD):<sup>67</sup>



Upon sodiation, crystalline Sb forms an amorphous  $\text{Na}_x\text{Sb}$  intermediate phase, instead of crystalline  $\text{NaSb}$ , as predicted by the phase diagram of  $\text{Na-Sb}$ . Further sodiation leads to the formation of crystalline  $\text{Na}_3\text{Sb}$ , which is consistent with the phase diagram. During desodiation, the  $c\text{-Na}_3\text{Sb}$  converts to amorphous Sb. Allan et al. also investigated the phase transition of  $\text{Na-Sb}$  during sodiation–desodiation by ex-situ solid-state nuclear magnetic resonance (NMR) spectroscopy and operando pair distribution function analysis, and they identified two intermediate amorphous phases, including  $a\text{-Na}_{1.7}\text{Sb}$  and  $a\text{-Na}_{(3-x)}\text{Sb}$  ( $x \approx 0.4\text{--}0.5$ ).<sup>68</sup>

Some studies of Sb show a good cycling stability as the anode for SIBs. For example, Darwiche et al. reported that Sb in SIBs outperforms its cycling performance in LIBs, despite the significantly larger volume change during sodiation (293%) than lithiation (135%).<sup>67</sup> When tested at a rate of 0.5 C, the Sb in SIBs shows a reversible capacity of around 575 mAh/g and negligible capacity degradation after 160 charge/discharge cycles, as shown in Figure 1.10 (a). However, the cycle lives of Sb powders were not reported to be higher than 100 cycles in all studies, and methods to further improve the cycling stability are needed.<sup>38,49,50</sup> A  $\text{Zn}_4\text{Sb}_3$  thin film anode shows a reversible capacity of around 450 mAh/g and a good cyclability (>250 cycles).<sup>45</sup> A  $\text{Zn}_4\text{Sb}_3$  nanowire also has been reported to exhibit ultrafast sodiation, which is ascribed to the observed layer structure of  $\text{NaZnSb}$ ; it is promising for high rate anode materials for SIBs.<sup>69</sup> Bi–Sb alloys also show an excellent rate capability and significantly improved cycling stability compared to the elemental Sb baseline.<sup>50,70</sup> Specifically, a nanoporous  $\text{Bi}_2\text{Sb}_6$  alloy shows an ultra-long cycle life (over 10000 cycles) when tested at a current density of 1 A/g, although the average reversible capacity exhibited is only  $\sim 200$  mAh/g.<sup>70</sup> The electrochemical performance of  $\text{Mo}_3\text{Sb}_7$ ,<sup>71</sup>  $\text{AlSb}$ ,<sup>72</sup> and  $\text{Cu}_2\text{Sb}$ <sup>44</sup> thin films (0.2–1.1  $\mu\text{m}$ ) as anodes for SIBs also has been investigated and shows excellent rate capability, but their reversible specific capacity and cycle life are only moderate. Recent work from our group shows that by alloying with Si, both the reversible capacity and the cycle life of Sb was improved significantly.<sup>61</sup> With only 7 at % addition of Si, the experimental reversible capacity increased from 625 mAh/g for elemental Sb to 663 mAh/g, and the  $\text{Si}_{0.07}\text{Sb}_{0.93}$  does not show obvious capacity degradation after 200 charge/discharge cycles.

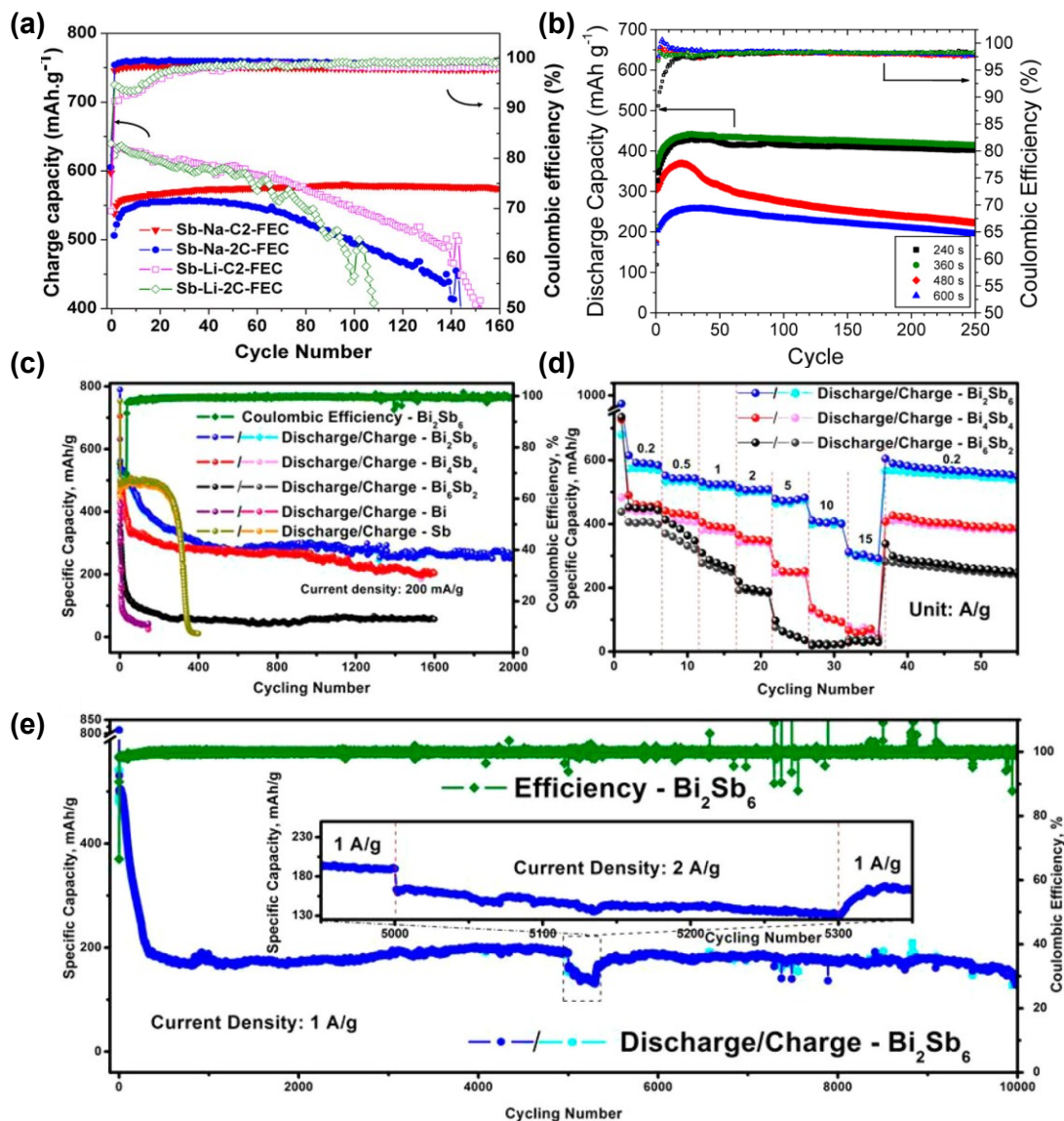


**Figure 1.10.** Specific capacity and corresponding Coulombic efficiency vs cycle number of (a) bulk Sb, (b)  $Zn_4Sb_3$  alloys prepared with a different deposition time, (c) nanoporous Bi–Sb alloys, pure Bi and pure Sb, and (e) nanoporous  $Bi_2Sb_6$  alloy. (d) Rate capability of the nanoporous Bi–Sb alloys. Reproduced and adapted with permission from reference 67 (Copyright 2012 American Chemical Society), reference 45 (Copyright 2015 American Chemical Society), and reference 70 (Copyright 2018 American Chemical Society).

### 1.3.5 Challenges of Alloying Anodes Towards Practical Applications

Although significant improvement in terms of cycle life has been achieved for alloying anodes, to date, most of the alloying anodes for SIBs have a cycle life below 500 cycles and when tested at practical conditions in a full cell, their cycle life will be even shorter.<sup>21,22</sup> Besides, there is still a lack of understanding or consensus on the

sodiation/desodiation mechanism of most alloy anodes; this holds back their further improvement. An in-depth understanding of the reaction and degradation mechanisms, as well as comprehensive design and fabrication strategies of alloying anodes, are required for developing the alloying anodes further and eventually applying them in commercial SIBs.

## **1.4 Silicon-based Anodes for Lithium-ion Batteries**

For commercial LIBs, many types of cathode materials, including  $\text{LiCoO}_2$ ,  $\text{LiFePO}_4$ ,  $\text{LiMn}_2\text{O}_2$ ,  $\text{LiNi}_x\text{Mn}_y\text{Co}_{1-x-y}\text{O}_2$ , and  $\text{LiNi}_{0.80}\text{Co}_{0.15}\text{Al}_{0.05}\text{O}_2$ , have been developed and applied.<sup>73</sup> On the anode side, graphite, which has only moderate intrinsic gravimetric and volumetric capacities of 372 mAh/g and 747 mAh/cm<sup>3</sup>, has been used in commercial LIBs for decades.<sup>74</sup> Silicon, on the other hand, has about 10 times higher theoretical capacity (3579 mAh/g and 8334 mAh/cm<sup>3</sup> based on  $\text{Li}_{3.75}\text{Si}$ ) than graphite. Even in the lithiated state, the theoretical capacity of lithiated silicon is still significantly higher than that of lithiated graphite, as shown in Table 1.3. Moreover, Si has a low discharge potential (0.4 V vs  $\text{Li/Li}^+$ ) and a large elemental abundance (second highest in earth's crust). Replacing graphite with silicon theoretically will lead to around a 40% increase in gravimetric energy density for LIBs.

**Table 1.3.** Comparison of Delithiation Potential, Theoretical Capacity, and Volume Change of Graphite and Silicon.

Materials	Graphite	Silicon
Average delithiation potential (V vs Li/Li <sup>+</sup> )	0.05	0.4
Lithiated phase	LiC <sub>6</sub>	Li <sub>3.75</sub> Si
Theoretical gravimetric capacity in delithiated state (mAh/g)	372	3579
Theoretical gravimetric capacity in lithiated state (mAh/g)	339	1857
Theoretical volumetric capacity in delithiated state (mAh/cm <sup>3</sup> )	837	8334
Theoretical volumetric capacity in lithiated state (mAh/cm <sup>3</sup> )	747	2193
Volume change (%)	12	280

The research of silicon as an anode started in the 1970s. In 1976, Sharma and Seefurth reported that Li<sub>x</sub>Si alloys reversibly formed in a high-temperature cell operating between 377 °C and 452 °C.<sup>75,76</sup> The intermediate phases of the Li–Si system at 415 °C was determined as Li<sub>12</sub>Si<sub>7</sub>, Li<sub>7</sub>Si<sub>3</sub>, Li<sub>13</sub>Si<sub>4</sub>, and Li<sub>22</sub>Si<sub>5</sub>.<sup>77</sup> The formation of Li<sub>22</sub>Si<sub>5</sub> corresponds to a specific capacity of 4200 mAh/g and is associated with a large volume change of 320%.<sup>78,79</sup> However, at room temperature, the lithiation behavior of Si is very different. At room temperature, crystalline Si is amorphized during the first lithiation, and the only crystalline phase observed is Li<sub>15</sub>Si<sub>4</sub> (Li<sub>3.75</sub>Si) when the cut-off voltage is below 50 mV.<sup>80–82</sup> By using in situ Li NMR analysis, the phase transitions of Si at room temperature during (de)lithiation were found to go through amorphous a-Li<sub>2.0</sub>Si, a-Li<sub>3.5</sub>Si, and crystalline c-Si<sub>3.75</sub>Si.<sup>81</sup> The formation of c-Si<sub>3.75</sub>Si corresponds to a 280% volume change for the Si electrode.<sup>78–80</sup> The large volume change during repeated charge/discharge cycles leads to a continuous fracture and pulverization of the Si electrode and loss of electrical contact, resulting in a poor cycle life (Figure 1.11).<sup>83–86</sup> Moreover, the large volume change exacerbates the growth of the solid electrode interphase (SEI) because

it will break the previously formed SEI (Figure 1.11).<sup>83–86</sup> The continuous growth of SEI will deplete the electrolyte, increase charge transfer resistance, and eventually result in capacity degradation of the battery.<sup>83–86</sup> To address these problems, many methods have been developed in recent decades, including constructing nanoscale Si with various structures (nanoparticles,<sup>87,88</sup> nanowires,<sup>89,90</sup> nanotubes,<sup>91,92</sup> core-shell structures,<sup>93–96</sup> to name a few), compositing metal or carbonaceous materials,<sup>97–105</sup> and integrating effective binders.<sup>106–111</sup> Some of the work achieved long term cycling stability while it maintained the high capacity of Si. However, for widespread application of Si in commercial LIBs, there are still some challenges, including low initial Coulombic efficiency, low packing density, and high processing cost, and more research is required to overcome these challenges.<sup>85,86</sup>

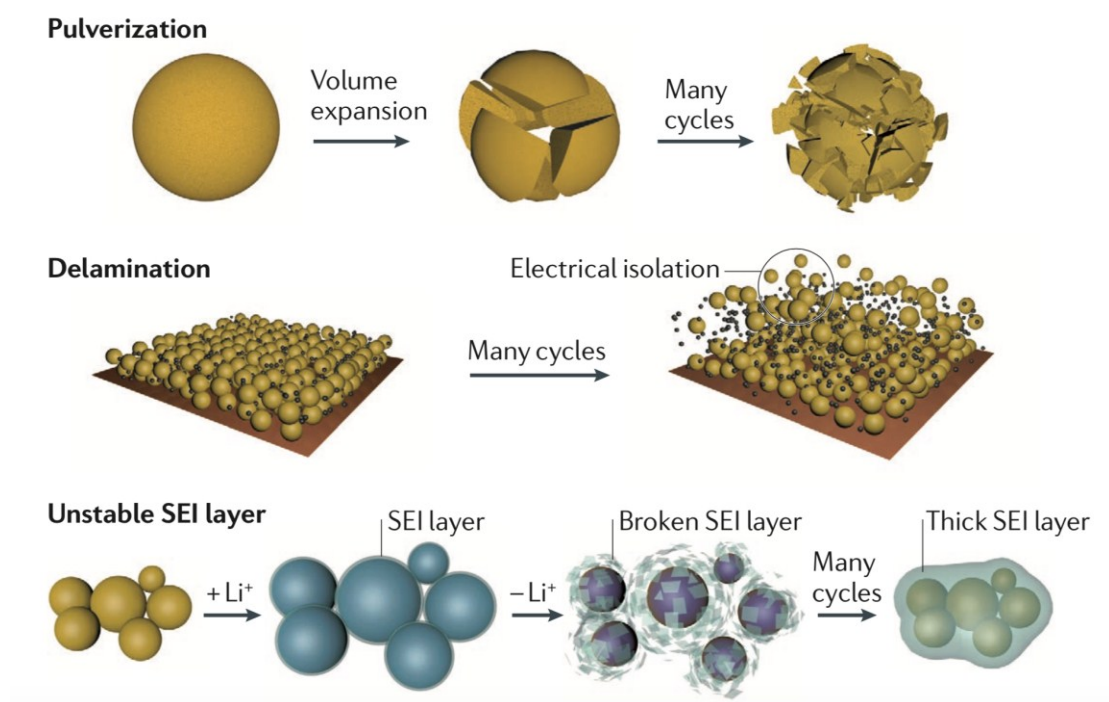


**Figure 1.11.** Schematic illustration of the main degradation mechanism of the Si anode. Reproduced with permission from reference 83 (Copyright 2016 Macmillan Publishers Limited).

## **1.5 Scope of the Thesis**

The focus of this thesis is to develop and fundamentally understand high capacity alloying anodes for advanced lithium-ion and sodium-ion batteries. It consists of the following five chapters, with the scope of each chapter provided.

### **1.5.1 Chapter 1 Scope**

This chapter provides an overview of the motivation, working principles, evaluation criteria, and development of lithium-ion and sodium-ion batteries. It highlights the advantages, challenges, and research development of high capacity alloying anodes for SIBs and silicon-based anodes for LIBs.

### **1.5.2 Chapter 2 Scope**

Chapter 2 reports the microstructure and electrochemical performance of three series of Sn–Bi–Sb alloys, as well as pure Sn, Bi, and Sb, as anodes for SIBs. Alloying was utilized as an approach to modify the morphology and active phases in an effort to improve the cycling stability of elemental anodes of Sn or Sb while maintaining high capacity. The films were prepared via sputtering, which enabled the study of a broad swath of compositional space. The cycling performance of the Sb-rich compositions surpassed that of all other alloys tested as anodes for SIBs. The best performing alloy had a composition of 10 at% Sn, 10 at% Bi, and 80 at% Sb (called Sn<sub>10</sub>Bi<sub>10</sub>Sb<sub>80</sub>, here), and maintained 99% of its maximum capacity during cycling (621 mA h g<sup>-1</sup>) after 100 cycles. The stability of these anodes dropped as the quantity of Sb decreased; in contrast, Sn<sub>20</sub>Bi<sub>20</sub>Sb<sub>60</sub>, Sn<sub>25</sub>Bi<sub>25</sub>Sb<sub>50</sub>, and Sn<sub>33</sub>Bi<sub>33</sub>Sb<sub>33</sub> were increasingly less stable as anodes in SIBs as the molar quantity of Sb in the films dropped to 60%, 50%, and 33%, respectively. The Sn<sub>10</sub>Bi<sub>10</sub>Sb<sub>80</sub> electrode was found to possess a single phase as-deposited microstructure of Sn and Bi in substitutional solid solution with the Sb lattice, and the sodiation sequence was found to be significantly different from that of pure Sb. Numerous possible mechanisms for the improvement in capacity retention were discussed, of which the modification and material response to internal stresses by changes in the Sb chemical potential and solid solution

strengthening were found to be the most likely. A version of this chapter was published in the *Journal of Materials Chemistry A*.<sup>19</sup>

### 1.5.3 Chapter 3 Scope

Chapter 3 details the sodiation–desodiation mechanism of  $\beta$ -SnSb. It is known to be a highly stable anode for sodium-ion batteries during cycling, but its sodiation–desodiation alloying reactions are understood poorly. By combining in situ TEM with electroanalytical methods, we demonstrated that  $\beta$ -SnSb forms  $\text{Na}_3\text{Sb}$  and  $\text{Na}_{15}\text{Sn}_4$  in sequence upon sodiation and re-forms as  $\beta$ -SnSb upon desodiation. The negative enthalpy of mixing for Sn and Sb is sufficient to cause sequentially deposited bilayers of Sn/Sb to transform into  $\beta$ -SnSb, resulting in comparable cycling stability. The good cycling stability of  $\beta$ -SnSb results from the complex two-phase amorphous–nanocrystalline microstructure in the partially charged–discharged states, as well as the intrinsic mechanical toughness of the  $\beta$  phase. Per the in situ TEM results, the sequential phase transformation shows minimal fracturing of the  $\beta$ -SnSb, indicating facile buffering of stresses. Extensively cycled specimens eventually show crystalline Sn phase segregation, which may be the source of the ultimate capacity fade in the alloy and bilayers. The work of this chapter has been published in *ACS Energy letters*.<sup>60</sup>

### 1.5.4 Chapter 4 Scope

Chapter 4 discusses the effect of the adhesion layer and surface coating on the suppression of the c- $\text{Li}_{3.75}\text{Si}$  phase and SEI growth in the Si-based anode for LIBs. Ni, C, and  $\text{TiO}_2$  were used as models. The formation of c- $\text{Li}_{3.75}\text{Si}$  was found to be detrimental to electrode integrity because of the associated internal stress accompanied with the amorphous-phase and crystalline-phase transition, leading to faster capacity degradation. The Ni adhesion layer and C and  $\text{TiO}_2$  surface coatings were found to suppress the formation of c- $\text{Li}_{3.75}\text{Si}$ , resulting in improved capacity retentions and Coulombic efficiency. The carbon and titanium dioxide surface coatings also were found to influence the growth and composition of SEI.

### **1.5.5 Chapter 5 Scope**

Chapter 5 summarizes this thesis and proposes future research directions. Challenges for practical applications of the high capacity alloying anodes are summarized, and several strategies are introduced to guide their development toward practical applications for advanced lithium-ion and sodium-ion batteries.

## Chapter 2<sup>†</sup>

### Sn–Bi–Sb Alloys as Anode Materials for Sodium Ion Batteries

#### 2.1 Introduction

A number of group 14 and 15 elements, including Ge, Sn, Sb, and Bi, are attractive candidates as anodes for SIBs because of their high theoretical capacity.<sup>112–120</sup> Theoretically, Ge should be able to store 3Na/Ge,<sup>62</sup> corresponding to 1108 mAh/g, but this stoichiometry has never been reached electrochemically. In practice, the capacity of elemental Ge is limited to approximately 370 mAh/g.<sup>113,114</sup> In theory, Sn has the highest gravimetric capacity at 847 mAh/g at a stoichiometry of Na<sub>15</sub>Sn<sub>4</sub>. However, capacity retention of pure Sn is generally very poor,<sup>118,119,121</sup> although limiting the upper voltage limit during cycling to below 0.68 V has been shown to improve capacity retention with cycling greatly.<sup>122</sup> Alloying with, for instance, Cu and Ge has also been shown to improve capacity retention of Sn greatly,<sup>123,124</sup> but at the cost of reducing the capacity to about half the theoretical capacity in the case of Cu,<sup>124</sup> whereas Ge contributed 1 Na/Ge.<sup>123</sup> On the other hand, for a group of ternary Sn-rich Sn–Ge–Sb alloys, it has been shown that all constituent elements can contribute their full theoretical capacity, i.e., 3.75 Na/Sn, 3 Na/Sb, and 3 Na/Ge.<sup>121</sup> The substantial improvement in cycling stability with respect to pure Sn was ascribed to the materials being composites with a high amorphous fraction, which may help to alleviate material pulverization resulting from the large volume expansion (420% for Sn going to Na<sub>15</sub>Sn<sub>4</sub>). Bismuth also has been investigated as a SIB anode,<sup>117,125,126</sup> but it also suffers rapid capacity decay when used in its elemental form<sup>117,126</sup> as a consequence of its high volume expansion of ~250% upon alloying to Na<sub>3</sub>Bi. Decreasing the crystallite size from ~130 to ~34 nm resulted in a marked improvement of the capacity retention from 20 to 80% of the theoretical value after

---

<sup>†</sup> The contents of this chapter have been reproduced and/or adapted from the following publication: Xie, H.; Kalisvaart, W. P.; Olsen, B. C.; Lubner, E. J.; Mitlin, D.; Buriak, J. M. Sn–Bi–Sb Alloys as Anode Materials for Sodium Ion Batteries. *J. Mater. Chem. A* **2017**, 5 (20), 9661–9670.

100 cycles.<sup>125</sup> Cycling stability being improved via grain size refinement is a well-documented phenomenon for a wide range of SIB and LIB anode materials.<sup>127–129</sup> Alloying has a large positive impact on the capacity retention of Bi as well, improving from 20% to 78% after 50 cycles upon alloying Bi with 43 at% Sb.<sup>130</sup>

Among the group of Na-alloying materials, Sb may be the most promising. It was found by Darwiche et al. that its cycling stability as a SIB anode even surpassed its performance as a LIB anode,<sup>115</sup> retaining >550 mAh/g after 160 cycles, despite the considerably higher expansion for Na<sub>3</sub>Sb vs Li<sub>3</sub>Sb (293% vs 135%). However, the performance of pure Sb powder is not found always to be stable over 100 or more cycles,<sup>126,128</sup> and ways to improve its cycling performance further still should be sought. Alloying with Al, Cu, Zn, and Mo has been found to endow thick Sb films (0.5–1.5 micron range) and nanowires with extraordinary rate capability.<sup>131–134</sup> Sb–Bi alloys outperform baseline elemental Sb in terms of cycling stability as well.<sup>130</sup> SbSn intermetallic can store ~700 mAh/g reversibly,<sup>135</sup> close to its theoretical capacity of 754, for over 100 cycles, although the total capacity and capacity retention are dependent on the particle size.<sup>136,137</sup>

A common finding that clearly emerges from previous works is that alloys outperform pure elements in cycling stability and often rate capability as well.<sup>127</sup> Given the promising results on some binary alloys in the Sn–Sb and Sb–Bi systems in particular, extending to ternary compositions is a logical step. In the present chapter, we report on the structure, electrochemical cycling stability and rate capability of three series of ternary Sn–Bi–Sb alloys and attempt to elucidate the relationships between microstructure and electrochemical performance. Compositions varied from 33–100 at% of the majority element, and the ratio of the minority elements was always 1:1. Sputtered films, rather than powders, were chosen as they allow for greater ease and flexibility with respect to varying the composition and for rapidly screening new materials.<sup>121,132,138,139</sup> Although sputter deposition often results in metastable materials, such as supersaturated solid solutions,<sup>121,123</sup> several techniques for making bulk materials, such as mechanical milling<sup>130</sup> and melt-spinning<sup>140</sup>, also are capable of producing non-equilibrium alloys. Therefore, our results should serve

as a useful guide for formulating new anode compositions in bulk form and to better understand how to optimize materials for SIBs.

## 2.2 Results and Discussion

The capacities as a function of cycle number for the different alloy series studied in this work are shown in Figure 2.1a–c. The theoretical capacities for each of the studied compositions, based on a simple rule of mixtures, are summarized in Table 2.1, together with the maximum measured capacities. It should be noted that the presence of a thin layer of oxide, as detected by XPS (see Figure 2.2), will lower the coulombic efficiency in the first cycle but not influence the capacity as the alloying reaction with sodium still will proceed after decomposition of the oxide.

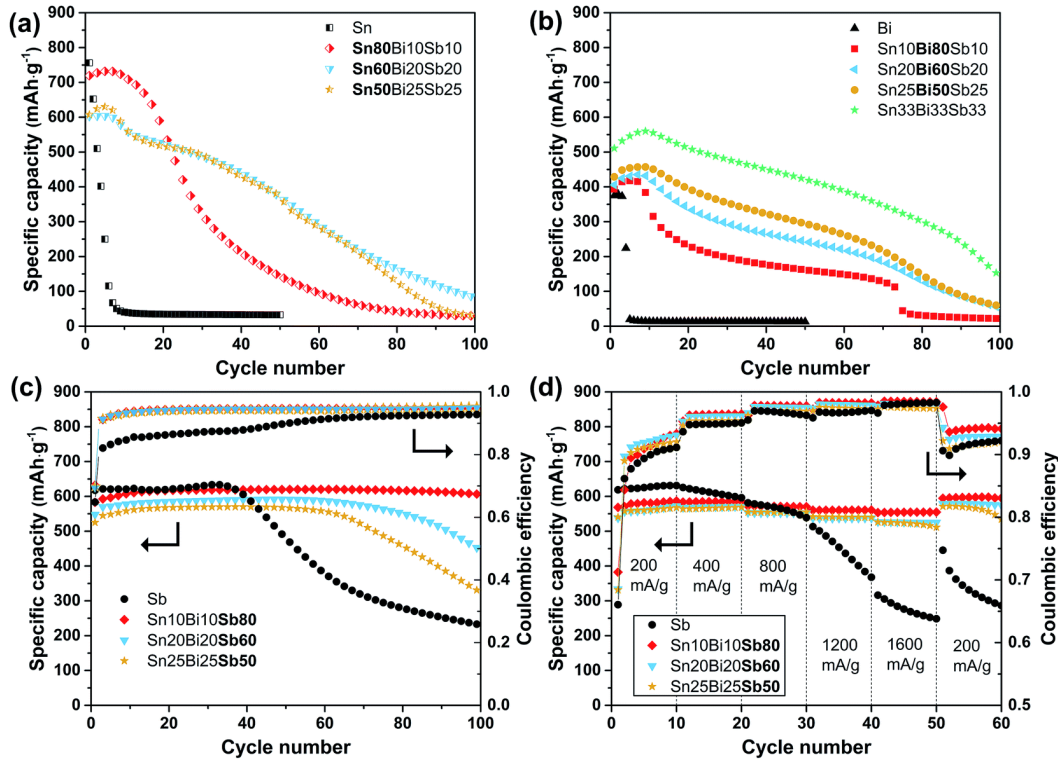


**Figure 2.1.** Specific capacity versus cycling number of (a) Sn-rich compositions (b) Bi-rich compositions (c) Sb-rich compositions. Coulombic efficiencies also are depicted for the Sb-rich compositions. (d) Rate tests and corresponding coulombic efficiency of Sb-rich compositions.

**Table 2.1.** Comparison Between Maximum Measured Capacities and Maximum Theoretical Capacities Based on a Rule of Mixtures Calculation for Each Composition.

Sample	Theoretical specific capacity (mAh/g)	Experimental specific capacity (mAh/g)
<b>Sn</b>	847	760
<b>Bi</b>	385	380
<b>Sb</b>	660	635
<b>Sn80Bi10Sb10</b>	754	745
<b>Sn60Bi20Sb20</b>	673	610
<b>Sn50Bi25Sb25</b>	637	630
<b>Sn10Bi80Sb10</b>	431	430
<b>Sn20Bi60Sb20</b>	487	445
<b>Sn25Bi50Sb25</b>	519	460
<b>Sn33Bi33Sb33</b>	633	621
<b>Sn10Bi10Sb80</b>	609	592
<b>Sn20Bi20Sb60</b>	603	575
<b>Sn25Bi25Sb50</b>	581	560

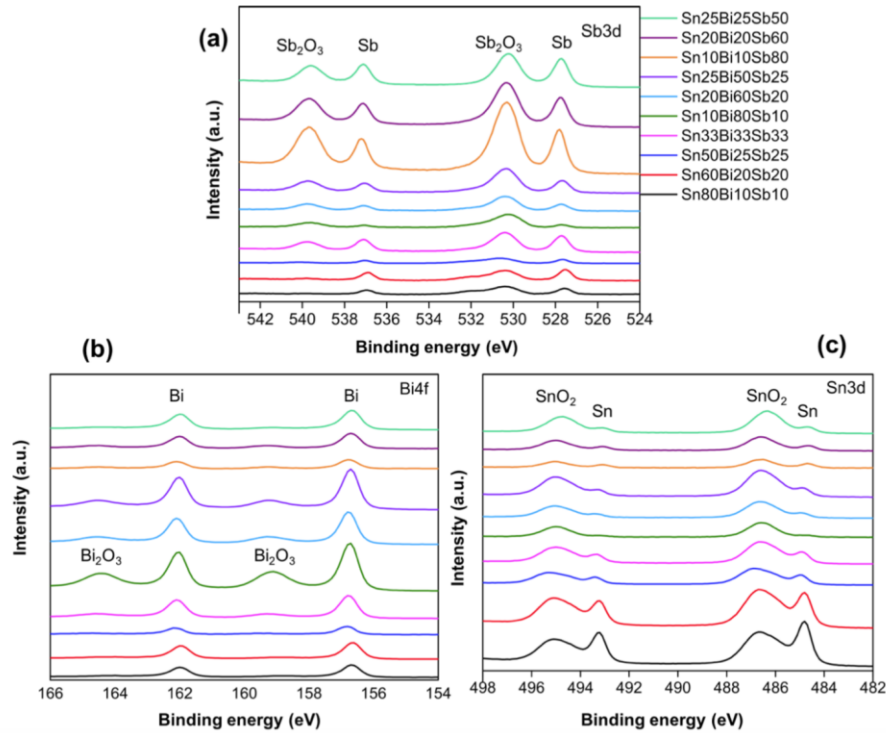


**Figure 2.2.** High resolution XPS spectra of Sb3d, Sn3d, and Bi4f of as-deposited thin films for all the alloy compositions investigated in this work.

As expected, pure Sn and the **Sn80Bi10Sb10** alloys have the highest initial capacities. Both degrade very quickly; this often is observed for pure Sn and very Sn-rich thin films.<sup>119,121</sup> **Sn80Bi10Sb10** achieves a maximum reversible capacity of 745

mAh/g, which is within experimental error of its theoretical maximum of 754 mAh/g (~1% difference). The alloys with 60 at% Sn and pure Sn show a somewhat larger negative deviation from their theoretical capacity, whereas **Sn50Bi25Sb25** is close to its theoretical maximum with a measured maximum capacity of 630 mAh/g. Consistent with general trends from literature,<sup>121,123,124</sup> the Sn-rich alloys show improved cycling stability compared to pure Sn, and a higher content of alloying elements improves the capacity retention past cycle 25. All Sn-rich compositions degrade to <100 mAh/g after 100 cycles.

Similar to pure Sn, the capacity of pure Bi degrades very rapidly. Here too, alloying improves the capacity retention. Alloying with Sn and Sb naturally increases the theoretical capacity of the materials since Bi has the lowest capacity by a wide margin among Sn (847 mAh/g), Sb (660 mAh/g), and Bi (385 mAh/g). However, the measured maximum reversible capacity stays approximately constant at 425–450 mAh/g for the alloys with 80, 60, and 50 at% Bi, which is near the theoretical capacity only in the case of **Sn10Bi80Sb10** (431 mAh/g). The **Sn33Bi33Sb33** alloy approaches its theoretical maximum capacity again (see Table 2.1). Capacity retention remains poor for all Bi-rich compositions, and past cycle 75, the capacity degrades to nearly zero for the alloys with 80, 60, and 50 at% Bi. **Sn33Bi33Sb33** has a capacity of ~150 mAh/g after 100 cycles but also is rapidly degrading at that point.

Of all the alloys tested, Sb and Sb-rich alloys show the best cycling performance by far, as is obvious from comparing Figure 2.1a,b with Figure 2.1c. The maximum reversible capacity for pure Sb reaches 635 mAh/g, which is close to its theoretical maximum of 660. The Sb-rich alloys all have a small negative deviation from their theoretical capacity that increases slightly with decreasing Sb content from 12 to 17 and eventually 28 mAh/g for 80, 60, and 50 at% Sb, respectively. Interestingly, all compositions other than **Sn10Bi10Sb80** show a stable capacity for a few tens of cycles from 35 for pure Sb to 60–80 cycles for **Sn20Bi20Sb60** and **Sn25Bi25Sb50**, after which they steadily degrade. In terms of cycling retention, **Sn10Bi10Sb80** shows a stable capacity of ~620 mAh/g for 100 cycles and thus outperforms both pure Sb and the alloys with higher Sn and Bi contents. Capacity retention after 100 cycles is 450, 320, and 225 mAh/g for 60, 50, and 100 at% Sb, respectively.

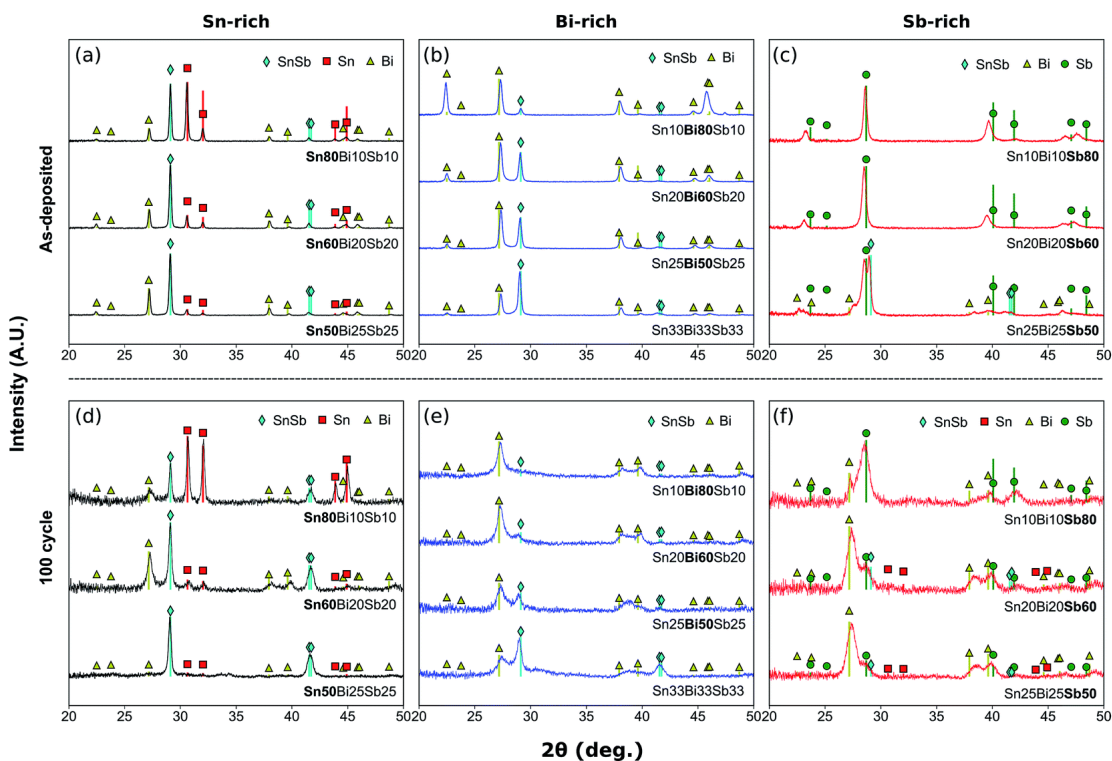


**Figure 2.3.** XRD patterns of as-deposited alloy films (top row) and after 100 electrochemical cycles (bottom row). Reference diffraction patterns: Sn (PDF no. 04-004-7747), Bi (PDF no. 00-005-0519), Sb (PDF no. 00-035-0732) and  $\beta$ -SnSb (PDF no. 04-014-6042).

**Table 2.2.** Phases Present in All As-deposited Films and Corresponding Cycled Films, as Determined by XRD.

Alloy composition	Phases present (as-deposited)	Phases present (cycled)
<b>Sn80Bi10Sb10</b> , <b>Sn60Bi20Sb20</b> , <b>Sn50Bi25Sb25</b>	(Sn), (Bi), $\beta$ -SnSb	(Sn), (Bi), $\beta$ -SnSb
<b>Sn10Bi80Sb10</b> , <b>Sn20Bi60Sb20</b> , <b>Sn25Bi50Sb25</b>	(Bi), $\beta$ -SnSb	(Bi), $\beta$ -SnSb
<b>Sn33Bi33Sb33</b>	(Bi), $\beta$ -SnSb	(Bi), $\beta$ -SnSb
<b>Sn10Bi10Sb80</b>	(Sb)	(Sb), (Bi)
<b>Sn20Bi20Sb60</b>	(Sb)	(Sb), (Bi), (Sn), $\beta$ -SnSb
<b>Sn25Bi25Sb50</b>	(Sb), (Bi), $\beta$ -SnSb	(Sb), (Bi), (Sn), $\beta$ -SnSb

From the XRD patterns in Figure 2.3, the grain sizes (measured perpendicular to the film surface) were estimated using the Scherrer equation<sup>141,142</sup> after correcting for instrumental broadening:

$$D = \frac{K_s \lambda}{\beta_{2\theta} \cos(\theta_0)}$$

where  $K_s = 1.07$  is the Scherrer constant for spherical particles,  $\lambda = 0.154$  nm is the wavelength of the X-ray source,  $\beta_{2\theta}$  is the integral breadth of a given peak, and  $\theta_0$  is the peak position. Scherrer equation relates the size of a crystallite to the peak width in a diffraction pattern. However, it is worth noting that many other factors, such as instrumental broadening and strain broadening can also contribute to the peak broadening. In order to analyze the size of a crystallite, the peak needs to be deconvoluted and different contributions need to be separated. In addition, the Scherrer equation assumes that all crystallites have the same size and shape, but in reality, the crystallites may have a broad size distribution and different shapes. Moreover, the grain size calculated by Scherrer equation is the grain height perpendicular to the lattice plane and the grain size of a specimen in different directions may be very different, such as a monocrystalline thin film material.<sup>141,142</sup>

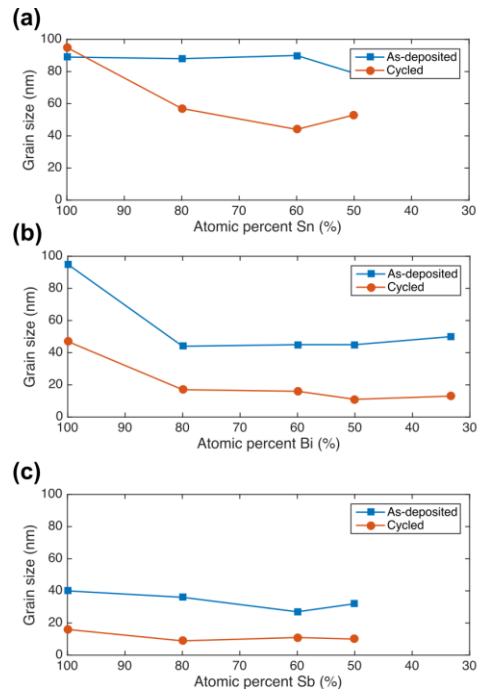


**Figure 2.4.** Average grain sizes of as-sputtered and cycled films, as determined by the Scherrer equation applied to the XRD patterns in Figure 2.3.

Given that most alloy compositions contain multiple phases, the calculated grain sizes in Figure 2.4 are given as the grain size of the majority phase(s). In general, the grain sizes of different phases for a given alloy were found to be within 10% of each other, with only a few exceptions.

A complete list of all of the grain sizes of each phase for each sample is given in Table 2.3 and 2.4. For the as-deposited films, with the exception of pure Bi, it is found that the grain size does not change significantly with composition (given that the same as-deposited phases are present), where Sn-rich, Bi-rich and Sb-rich films have average grain sizes on the order of 90, 45, and 30 nm respectively. After electrochemical cycling, it is observed that the grain sizes are refined and are found to be roughly half to a third of the as-deposited sizes. Investigation of the film morphologies via SEM reveals similar trends in lateral grain size with alloying, majority element, and cycling (Figures 2.5 and 2.6).

**Table 2.3.** Grain Sizes of All Phases in As-deposited Films (As Determined by XRD Using the Scherrer Equation).

Sample	(Sn) grain size (nm)	(Bi) grain size (nm)	(Sb) grain size (nm)	$\beta$ -SnSb grain size (nm)
Sn	89			
<b>Sn80Bi10Sb10</b>	88	85		99
<b>Sn60Bi20Sb20</b>	90	87		91
<b>Sn50Bi25Sb25</b>	77	85		81
Bi		95		
Sn10 <b>Bi80</b> Sb10		41		47
Sn20 <b>Bi60</b> Sb20		42		47
Sn25 <b>Bi50</b> Sb25		42		46
Sn33 <b>Bi33</b> Sb33		50		50
Sb			40	
Sn10Bi10 <b>Sb80</b>			36	
Sn20Bi20 <b>Sb60</b>			27	
Sn25Bi25 <b>Sb50</b>		9.3	22	42

**Table 2.4.** Grain Sizes of All Phases after 100 Constant Current Charge/Discharge Cycles.

Sample	(Sn) grain size (nm)	(Bi) grain size (nm)	(Sb) grain size (nm)	$\beta$ -SnSb grain size (nm)
Sn	95			
<b>Sn80Bi10Sb10</b>	54	11		60
<b>Sn60Bi20Sb20</b>	19	21		44
<b>Sn50Bi25Sb25</b>				53
Bi		47		
<b>Sn10Bi80Sb10</b>		17		
<b>Sn20Bi60Sb20</b>		16		9.2
<b>Sn25Bi50Sb25</b>		11		15
<b>Sn33Bi33Sb33</b>		7.1		19
Sb			16	
<b>Sn10Bi10Sb80</b>		33	8.9	
<b>Sn20Bi20Sb60</b>		11	8.2	
<b>Sn25Bi25Sb50</b>		10	11	

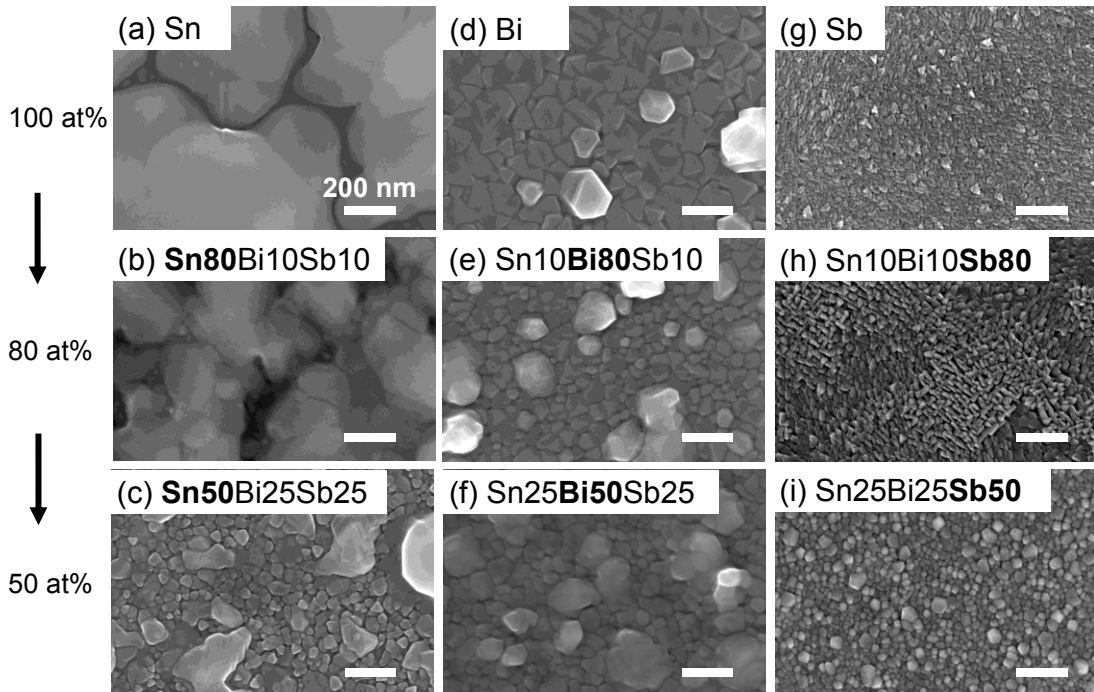


**Figure 2.5.** SEMs of as-deposited elemental films and alloys. (a) Sn, (b) **Sn80Bi10Sb10**, (c) **Sn50Bi25Sb25**, (d) Bi, (e) **Sn10Bi80Sb10**, (f) **Sn25Bi50Sb25**; (g) Sb, (h) **Sn10Bi10Sb80**, (i) **Sn25Bi25Sb50**. All scale bars are 200 nm. The numbers following the elements represent the molar percent of elements in the film.

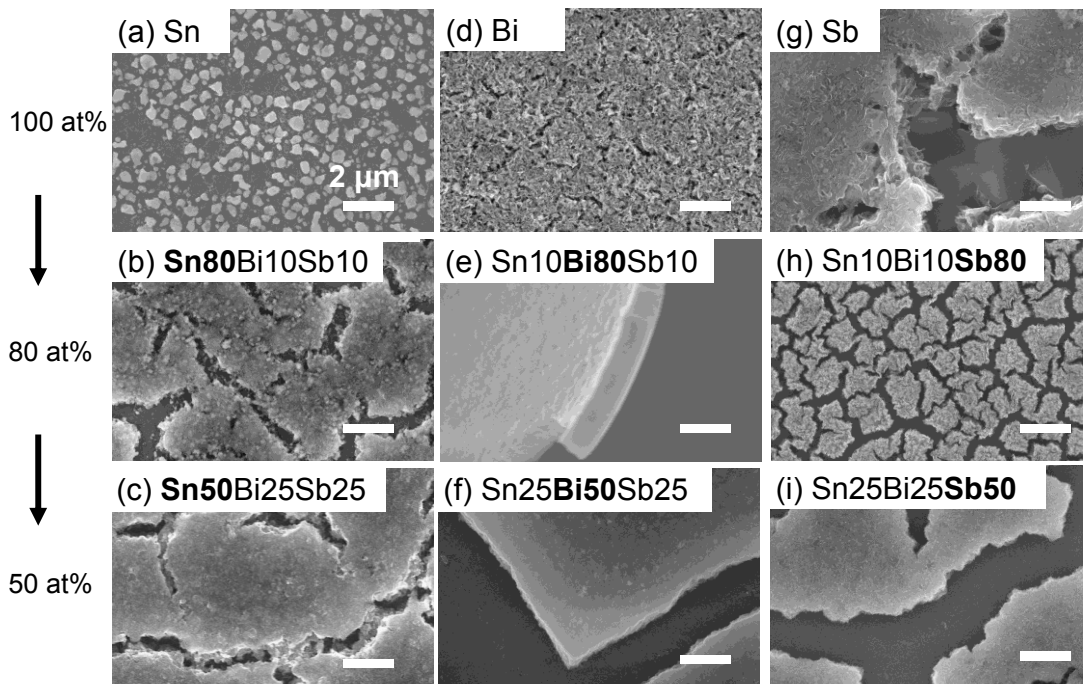


**Figure 2.6.** SEM micrographs of the cycled elemental films and alloys. (a) Sn (b) **Sn80Bi10Sb10**, (c) **Sn50Bi25Sb25**; (d) Bi, (e) Sn10**Bi80**Sb10, (f) Sn25**Bi50**Sb25; (g) Sb, (h) Sn10Bi10**Sb80**, (i) Sn25Bi25**Sb50**. Pure Sn and Bi were cycled 50 times, and all other electrodes 100 times. All scale bars are 2  $\mu\text{m}$ .

Voltage profiles and  $dQ/dV$  plots for all Sn-rich alloy compositions are shown in Figure 2.7, Bi-rich in Figure 2.8, and Sb-rich in Figure 2.9. As shown in the XRD patterns in Figure 2.3 and their summary in Table 2.2, Sn and Bi-rich alloys consist of (Sn), (Bi), and  $\beta$ -SnSb phases in their as-deposited state. One would, therefore, expect to find characteristic features of these phases in the voltage profiles and  $dQ/dV$  plots. Elemental Sn stores a large amount of Na at potentials below 0.1 V, which shows up as a long, relatively flat plateau in the sodiation voltage profile and a large peak in  $dQ/dV$ . All Sn-rich alloys display this feature very clearly. A Bi phase also was found in all Sn-rich compositions, and a sharp peak at  $\sim 0.7$  V, increasing with increasing Bi and Sb content, is observed in the sodiation branch. In the region between 0.6 and 0.3 V, there are a large number of overlapping features related to elemental Sn (0.4 V, see Figure 2.7) and  $\beta$ -SnSb,<sup>43</sup> in accordance with the XRD results. The Bi-rich alloys consist of Bi and  $\beta$ -SnSb phases. The  $dQ/dV$  plots all show the dual-peak structure of pure Bi in both the sodiation and desodiation branch with small shifts towards more negative potentials for sodiation and more positive potentials for desodiation.

Compared to elemental Bi, the peaks also are broader and have increasingly large shoulders at  $\sim 0.3$  V (sodiation) and  $\sim 0.55$  V (desodiation), as well as a minor peak below 0.1 V with increasing Sn and Sb content. This sodiation peak below 0.1 V is attributed to the  $\beta$ -SnSb phase, which is consistent with previous results.<sup>135</sup> This is especially clear for Sn<sub>33</sub>Bi<sub>33</sub>Sb<sub>33</sub> where the feature below 0.1 V is suddenly much larger compared to all the other Bi-rich alloys and was, together with Sn<sub>10</sub>Bi<sub>80</sub>Sb<sub>10</sub>, the only Bi-rich alloy to reach its theoretical capacity. These results suggest that the sodiation behavior of the  $\beta$ -SnSb phase is very strongly dependent on the microstructure and that it does not always sodiate to its maximum extent of 3 Na/Sb and 3.75 Na/Sn. For example, studies investigating anodes made from colloidal  $\beta$ -SnSb nanocrystals did not reach full capacity,<sup>136,137</sup> while anodes made from ball-milled powders of  $\beta$ -SnSb reached full capacity.<sup>135</sup>

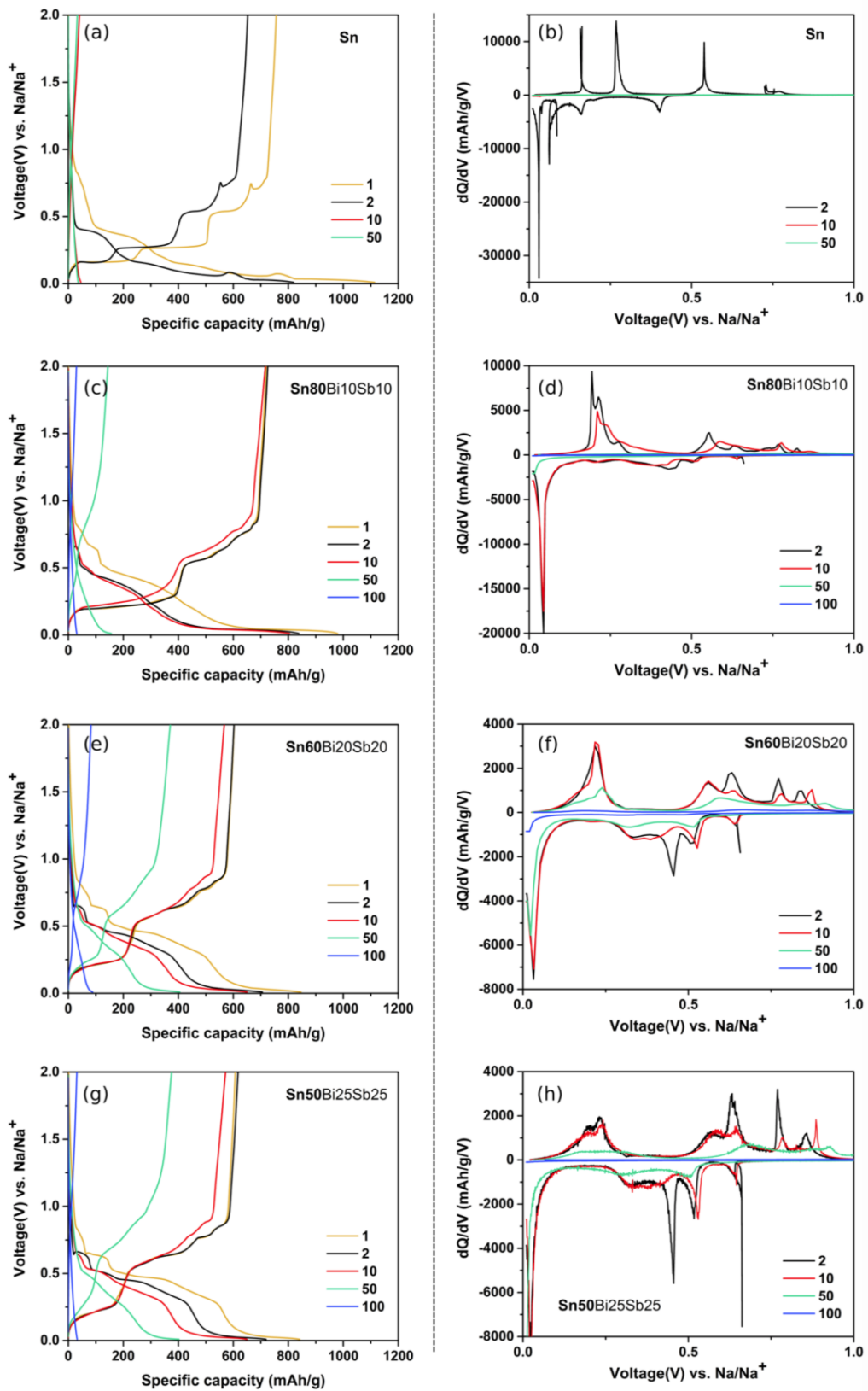


**Figure 2.7.** Voltage profiles (left) and corresponding  $dQ/dV$  plots (right) for (a,b) elemental Sn, (c,d)  $\text{Sn}_{80}\text{Bi}_{10}\text{Sb}_{10}$ , (e,f)  $\text{Sn}_{60}\text{Bi}_{20}\text{Sb}_{20}$  and (g,h)  $\text{Sn}_{50}\text{Bi}_{25}\text{Sb}_{25}$ .

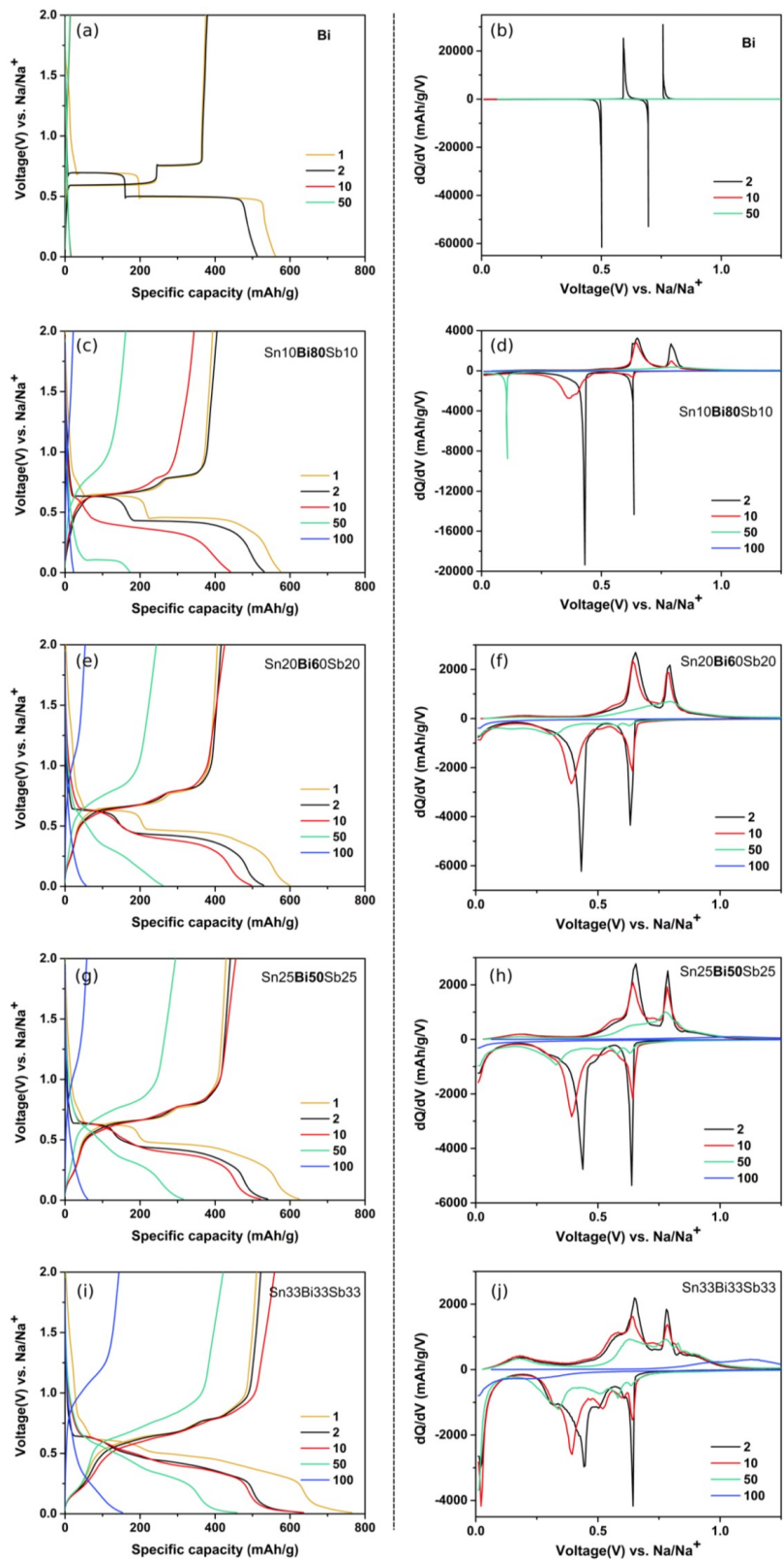


**Figure 2.8.** Voltage profiles (left) and corresponding  $dQ/dV$  plots (right) for (a,b) elemental Bi, (c,d)  $\text{Sn}_{10}\text{Bi}_{80}\text{Sb}_{10}$ , (e,f)  $\text{Sn}_{20}\text{Bi}_{60}\text{Sb}_{20}$ , (g,h)  $\text{Sn}_{25}\text{Bi}_{50}\text{Sb}_{25}$  and (i,j)  $\text{Sn}_{33}\text{Bi}_{33}\text{Sb}_{33}$ .

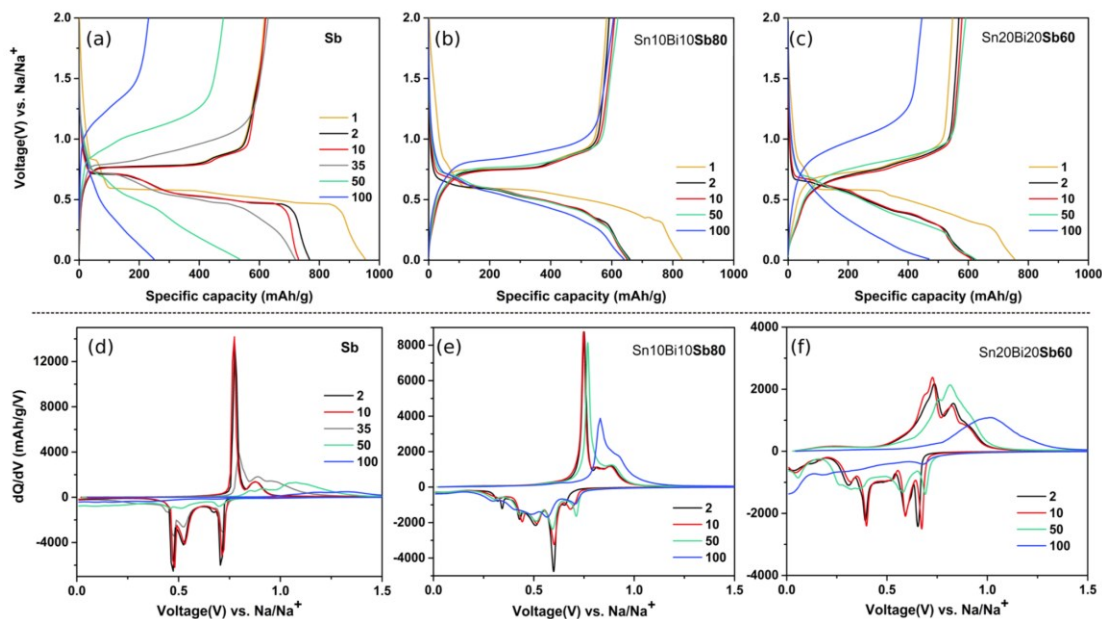


**Figure 2.9.** Voltage profiles (a)–(c) and corresponding dQ/dV plots for elemental Sb (a and d), Sn10Bi10Sb80 (b and e) and Sn20Bi20Sb60 (c and f).

Figure 2.9 shows the voltage profiles and dQ/dV curves for selected cycles of pure Sb, Sn10Bi10Sb80, and Sn20Bi20Sb60. The second sodiation profile of pure Sb shows two flat plateaus at  $\sim 0.7$  and  $\sim 0.5$  V and sloping regions in-between. To understand and quantify the sodiation/desodiation pathways better, the dQ/dV curves are fit using a series of Voigt functions (see Figure 2.10 and Table 2.5). The first phase transformation to occur during sodiation of the pure Sb film takes place at 0.71 V, which has a very narrow peak with a width of 9 mV (width is taken as the integral breadth of the peak). Next, there are two broad peaks at 0.68 and 0.52 V with widths of 101 and 97 mV, respectively. Last in the sodiation sequence is another sharp peak at 0.48 V with a width of 4 mV. Given the large differences in peak widths observed, corresponding to variance in sodiation site energies, the sodiation of these pure Sb films is believed to proceed via the following sequence: a) crystalline Sb to crystalline NaSb, b) crystalline NaSb to amorphous  $\text{Na}_x\text{Sb}$  ( $1 < x < 3$ ), and c) amorphous  $\text{Na}_x\text{Sb}$  to the terminal  $\text{Na}_3\text{Sb}$  crystalline phase. This is slightly different from what typically is reported in previous literature, where the peak at 0.71 V is broader, the small feature at 0.68 V is not resolved, and the final sharp peak often is found at much lower voltages, around 0.3 V.<sup>115,116,120</sup> In these cases, the first sodiation

peak is ascribed to the formation of an amorphous NaSb phase. It is believed that the crystalline NaSb phase is observed in this work due to the lower kinetic limitations for the thin films used (100 nm) compared to thicker thin films (1000 nm)<sup>120</sup> or films prepared from a nanoparticle slurry.<sup>116</sup> From the whole pattern fitting of the dQ/dV, it also is possible to estimate the relative sodiation capacity of each peak/reaction (Table 2.5). It should be noted that the majority of charge (46%) is stored during the formation of amorphous Na<sub>x</sub>Sb.

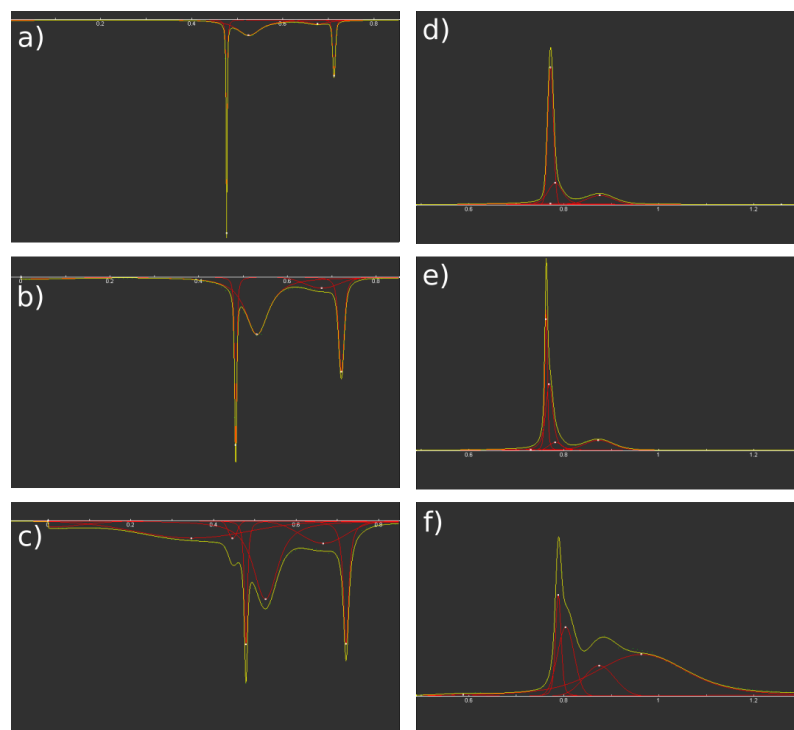


**Figure 2.10.** Curve fitting of dQ/dV the sodiation/desodiation profiles of pure Sb. (a–c) sodiation curves for cycles 2,10, and 35. (d–f) desodiation curves for cycles 2, 10, and 35.

**Table 2.5.** Peak Fit Parameters dQ/dV Curves of Pure Sb Films.**Sb - sodiation**

Cycle	Center (V)	Width (mV)	Area (%)
2	0.00	165	3.3
2	0.48	4	23.4
2	0.52	97	46.0
2	0.68	101	12.6
2	0.71	9	14.5
2	0.90	78	0.3
10	0.00	139	2.6
10	0.48	8	13.1
10	0.53	97	54.7
10	0.68	96	10.6
10	0.72	20	18.2
10	0.87	107	0.8
35	0.00	105	2.8
35	0.35	345	24.9
35	0.45	27	2.0
35	0.48	13	6.8
35	0.53	104	34.1
35	0.67	139	13.0
35	0.72	24	12.2
35	0.93	454	4.3

**Sb - desodiation**

Cycle	Center (V)	Width (mV)	Area (%)
2	0.77	15	59.3
2	0.77	344	12.3
2	0.88	80	15.6
2	1.25	1324	12.9
10	0.73	317	8.1
10	0.77	18	59.4
10	0.87	91	18.2
10	1.41	1485	14.4
35	0.59	111	0.8
35	0.79	17	22.8
35	0.87	82	12.0
35	0.96	288	56.1
35	1.59	1149	8.3

Fitting of the desodiation dQ/dV branch reveals a single sharp peak at 0.77 V (width = 15 mV), followed by a peak at 0.88 V with a larger width of 80 mV. Lastly, there is a very broad peak centered at 1.25 V, which accounts for a non-trivial portion of the desodiation capacity (13%). This desodiation profile is very similar to what has been observed by Darwiche et al<sup>115</sup> where the first peak at 0.77 V is ascribed to the transformation of crystalline Na<sub>3</sub>Sb to amorphous Na<sub>x</sub>Sb. The broad feature at 0.88 V has been assigned occasionally to the partial crystallization of Sb,<sup>116</sup> although other

reports find that the Sb is amorphous after desodiation.<sup>115,143</sup> The amorphous Sb structure has been ascribed to incomplete desodiation of the Sb due to kinetic limitations of sluggish Na diffusion.<sup>120</sup> On the other hand, we have found our cycled Sb film to be crystalline. A possible explanation is the reduced kinetic limitation of the very thin films (100 nm) and higher desodiation cut-off voltage of 2.0 V (previous works were limited to 1.5 V). The broad feature centered at 1.25 V may thus be associated with a crystallization event.

As cycling proceeds, the behavior of the Sb film changes. The dQ/dV curve for the 35<sup>th</sup> cycle, right before the onset of degradation for the Sb film (see Figure 2.1), still shows the same four sodiation peaks as well as an additional broad feature centered at 0.35 V, which accounts for 25% of the sodiation capacity. The desodiation behavior also changes, with an additional broad peak appearing at 0.96 V that accounts for the majority of the desodiation capacity (56%). Although we cannot relate these additional features in the dQ/dV curves to a specific phase transformation in the material, their appearance may be related to the grain size refinement that was observed for the Sb film (see Figure 2.3). Below 20 nm grain size, the sodiation behavior of Sb has been found to change in a similar way as observed in this work.<sup>116</sup> Another contributing factor may be internal fracturing of the film parallel to the substrate, as observed before, causing parts of the film to react with greater difficulty than others<sup>144</sup> and leading to more negative sodiation and more positive desodiation potentials, as observed in Figure 2.9.

The Sb alloy films show some strong similarities as well as differences with pure Sb. Sodiation of Sn<sub>10</sub>Bi<sub>10</sub>Sb<sub>80</sub> proceeds through a large number of intermediate phases, as evidenced by the myriad of overlapping peaks in the dQ/dV curve between ~0.65 and ~0.30 V. A small amount of Na also is stored at lower potentials as the dQ/dV curve does not go to zero. Curve fitting of the dQ/dV sodiation profile (Figure 2.11 and Table 2.6) reveals the presence of six distinct peaks with widths ranging from 20 to 60 mV, where the most prominent peak occurs at 0.60 V and accounts for 25% of the sodiation capacity. None of these peaks can be assigned to those found for pure Sb, Sn, or Bi as they all occur at different voltages. These data imply that the sodiation sequence of this single phase solid solution alloy is profoundly different

from pure Sb. Although there are a large number of distinct and sharp peaks observed, curve fitting shows that a very broad peak centered at 0.49 V with a width of 235 mV is necessary to fit the profile adequately, accounting for a very large fraction of the sodiation capacity (49%). This feature is very similar to that of the pure Sb film, which has a broad peak centered at 0.52 V, suggesting that Sn10Bi10Sb80 also forms an amorphous sodium-rich phase during sodiation. However, for the Sn10Bi10Sb80 alloy, the width of this peak is over 2.5 times larger and overlaps much more strongly with the other sodiation peaks compared to the elemental film. This result implies that the volume expansion of the alloy film is much more gradual and that several distinct sodiation processes may be occurring simultaneously. This is possible because instead of two components (Na and Sb), we now have four (Na, Sb, Bi, and Sn), which increases the maximum number of phases that can coexist in equilibrium.

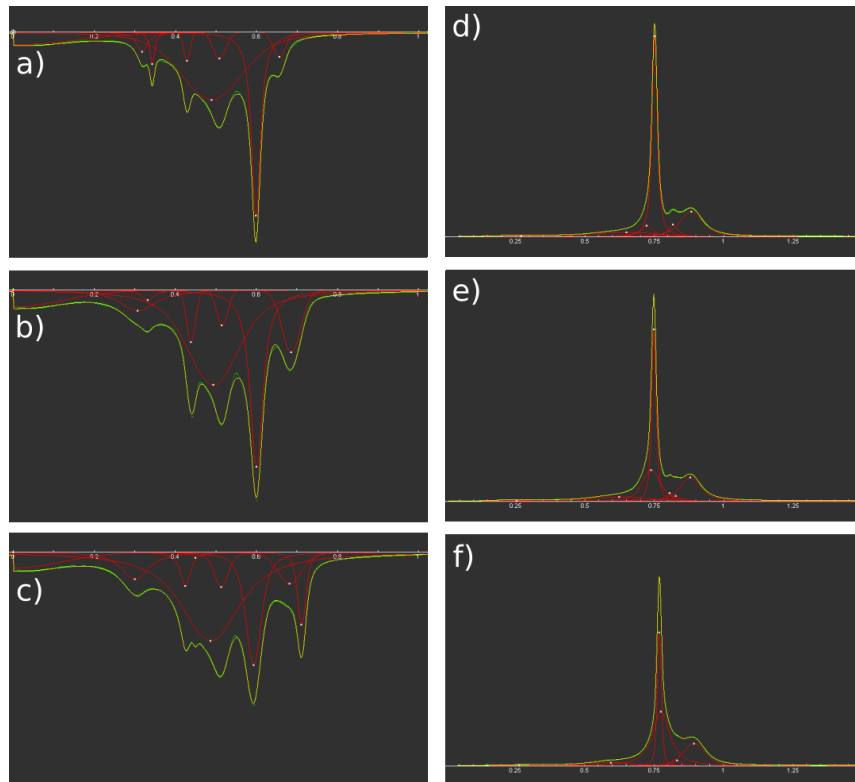


**Figure 2.11.** Curve fitting of  $dQ/dV$  the sodiation/desodiation profiles of Sn10Bi10Sb80. (a–c) sodiation curves for cycles 2, 10, and 50. (d–f) desodiation curves for cycles 2, 10, and 50.

**Table 2.6.** Peak Fit Parameters dQ/dV Curves of Sn10Bi10Sb80 Films.

**Sn10Bi10Sb80 - sodiation**

Cycle	Center (V)	Width (mV)	Area (%)
2	0.00	201	8.5
2	0.32	50	3.2
2	0.34	21	2.2
2	0.43	21	2.0
2	0.49	235	49.3
2	0.51	59	6.3
2	0.60	41	25.0
2	0.66	40	3.4
10	0.00	157	6.1
10	0.31	165	7.8
10	0.33	60	1.4
10	0.44	28	3.4
10	0.49	212	46.1
10	0.52	35	2.8
10	0.60	59	23.8
10	0.69	59	8.5
50	0.00	152	5.6
50	0.30	126	7.8
50	0.42	45	3.5
50	0.45	11	0.2
50	0.49	260	50.9
50	0.51	51	5.0
50	0.59	63	15.4
50	0.68	82	5.8
50	0.71	33	5.8

**Sn10Bi10Sb80 - desodiation**

Cycle	Center (V)	Width (mV)	Area (%)
2	0.27	292	2.9
2	0.65	318	9.5
2	0.72	53	6.3
2	0.75	33	44.6
2	0.82	64	5.2
2	0.88	137	23.2
2	1.54	1637	8.3
10	0.25	228	1.7
10	0.62	386	12.5
10	0.73	107	17.0
10	0.75	29	33.5
10	0.81	58	4.3
10	0.88	128	19.9
10	1.62	1938	11.1
50	0.26	265	1.6
50	0.60	309	7.4
50	0.77	23	19.9
50	0.78	114	40.6
50	0.83	71	2.6
50	0.89	124	18.5
50	1.75	127	9.6

Despite the significant differences in sodiation, the desodiation branch of **Sn10Bi10Sb80** appears to be very similar to that of pure Sb. Specifically, there are two major peaks at 0.75 and 0.88 V, which still account for the majority of the desodiation capacity (70%), and two broad peaks centered at 0.72 and 1.5 V, much like the Sb film. The only differences are the appearance of a small peak at 0.82 V (3% of the sodiation capacity) and a broad peak at low voltages (0.29 V). These data strongly suggest that, despite the significant differences in sodiation as evidenced by the large number of peaks in the dQ/dV curve, the terminal sodiated majority phase of **Sn10Bi10Sb80** is very similar to that of pure Sb.

Contrary to pure Sb, the sodiation/desodiation potentials do not change significantly over the first 50 cycles. Around the 50<sup>th</sup> cycle, a small peak appears at 0.71 V (6% of the sodiation capacity), which likely corresponds to the eventual segregation of Bi-phase, consistent with the XRD results in Figure 2.3. Only by the 100<sup>th</sup> cycle have the desodiation potentials shifted to higher voltages by ~120 mV, and the sodiation plateaus become less distinct.

The dQ/dV curves of **Sn20Bi20Sb60** show a much larger sodiation feature at around 0.7 V as compared to **Sn10Bi10Sb80**, in agreement with the difference in the amount of Bi phase observed in their respective XRD patterns. A broad peak at <0.1 V, most likely related to  $\beta$ -SnSb, also emerges. This trend continues with **Sn25Bi25Sb50**, which has even larger, sharper features in its dQ/dV curve related to Bi and  $\beta$ -SnSb, in accordance with the observations from XRD where the amount of Bi phase continued to increase with respect to Sb. At the same time, the cycling stability becomes worse with increasing amounts of segregated Bi. The capacities of **Sn20Bi20Sb60** and **Sn25Bi25Sb50** start to decline around cycle 60, with the capacity of **Sn25Bi25Sb50** declining substantially more rapidly (see Figure 2.1).

Of all of the alloy compositions investigated in this work, **Sn10Bi10Sb80** stands out as the most interesting one. Specifically, it has the same capacity as pure Sb while possessing much better cycling stability (minimal decrease in capacity after 100 cycles). There are a large number of possible reasons for this improvement in cycling stability, including but not limited to: nanostructuring size effects, stress-induced

voltage changes, solid solution strengthening, and solid solution modification of the Sb chemical potential.

A common strategy for improving capacity retention and rate capability is to nanostructure the electrode material,<sup>145–147</sup> where the nanostructured electrodes have faster stress relaxation and improved diffusion kinetics compared to microcrystalline materials.<sup>148,149</sup> However, for the electrode materials investigated in this work, it appears that the initial grain size is not the dominant factor affecting capacity retention. For example, the pure Sb (or Sn) and all of the Sb-rich (or Sn-rich) alloys have similar grain sizes (see Table 2.3), but the alloys exhibit a much higher degree of capacity retention.

A recently appreciated effect influencing capacity retention/fade in thin film batteries is stress-induced voltage changes, where a large compressive stress in the film during discharging (sodiation/lithiation) can cause voltage depressions up to ~200 mV.<sup>150</sup> In the case of Si and Si-based alloys, formation and crystallization of the terminal  $\text{Li}_{15}\text{Si}_4$  phase (forms at voltages less than 50 mV) is found to be highly detrimental and can be prevented as a result of stress-induced voltage effects.<sup>134,151</sup> It would appear that a similar effect is observed for the Sn-rich alloys studied in this work. Specifically, the terminal  $\text{Na}_{15}\text{Sn}_4$  phase also forms at a low sodiation voltage of ~50 mV, as can be seen by the large peak in the sodiation branch of Figure 2.7. A very clear shift and broadening of this peak can be seen for the **Sn60Bi20Sb20** (30 mV) and **Sn50Bi25Sb25** (20 mV) alloys, indicating that the  $\text{Na}_{15}\text{Sn}_4$  phase does not crystallize, as it is usually found to do.<sup>152</sup> The lack of crystallization of  $\text{Na}_{15}\text{Sn}_4$ , evidenced by the broader first desodiation peak in the  $dQ/dV$  curves of **Sn60Bi20Sb20** and **Sn50Bi25Sb25** as compared to elemental Sn and **Sn80Bi10Sb10**, is correlated strongly to capacity retention in the Sn-rich alloys, and it is the likely reason why **Sn60Bi20Sb20** and **Sn50Bi25Sb25** have markedly better capacity retention compared to pure Sn and **Sn80Bi10Sb10**. Stress-induced voltage shifts also are relevant to sodiation of  $\beta$ -SnSb, which is found to fully sodiate only at potentials around 20 mV.<sup>43</sup> As previously discussed, the **Sn10Bi80Sb10**, **Sn20Bi60Sb20** and **Sn25Bi50Sb25** alloys only see a shoulder of this low voltage sodiation peak, resulting in less-than-theoretical capacity, while **Sn33Bi33Sb33** has near-theoretical capacity

and a complete sodiation peak at  $\sim 20$  mV. Despite stress-induced shifts being observed in the majority of samples, it is unlikely to be the reason why Sn10Bi10Sb80 has improved capacity retention as all of the sodiation peaks are significantly above 0 V, resulting in complete sodiation of all phases present.

As previously discussed, the sodiation sequence of Sn10Bi10Sb80 is significantly different from pure Sb, as evidenced by the larger number of peaks in its dQ/dV curve that the presence of a small amount of free Bi cannot account for, while the desodiation behaviour is very similar. Given that both electrode materials have the same crystal structure, these data suggest that the solid solution elements (Sn and Bi) in the (Sb) phase modify the chemical potential of Sb, resulting in the different sodiation voltage profile that is observed.<sup>138</sup> Even pure Sb shows clear differences between sodiation and desodiation profiles from the second cycle onward, and the sodiation voltage profile for the first cycle is even more different (see Figure 2.9a and d), although the first and second desodiation profiles are the same. Despite these differences in the sodiation branch, the terminal phase has been found to be hexagonal Na<sub>3</sub>Sb for both the first and second sodiation of pure Sb through in-situ XRD.<sup>115</sup> Here, we observe widely different sodiation profiles but very similar desodiation profiles for elemental Sb and Sn10Bi10Sb80. In light of the aforementioned observations on pure Sb, this strongly suggests similar phase evolution during desodiation, although in-situ TEM or XRD studies should be conducted to confirm this and also to identify the intermediate sodiation stages. The high reactivity and small sample mass of the sodiated films with air prevented us from obtaining this information in ex-situ experiments.

A recent in-situ TEM investigation of nanoscale Sb revealed spatially heterogeneous sodiation behaviour, causing large stresses that can be relieved in a catastrophic manner; this is believed to play a major role in the capacity fade of Sb.<sup>144</sup> As such, it is possible that the observed changes in the sodiation sequence of Sn10Bi10Sb80 could result in a more spatially homogeneous sodiation process, in the sense that the relative expansion associated with each sodiation step is now smaller, and changes in the internal stresses and subsequent stress relaxation processes. Moreover, incorporation of Bi and Sn atoms into the Sb lattice leads to solid solution

strengthening, which can allow the electrode material to tolerate larger internal stresses.<sup>138</sup>

## 2.3 Conclusions

The addition of alloying elements into high capacity sodium-ion anode materials can be an effective approach to improving capacity retention. In this work, the ternary tin-bismuth-antimony system was investigated, where all the elemental components are active towards sodium. It was found that the capacity retention of all of the pure elemental anodes could be improved significantly, with minimal reduction in the specific capacity (relative to the pure elemental forms). The Sn<sub>10</sub>Bi<sub>10</sub>Sb<sub>80</sub> alloy was unique in terms of its outstanding capacity retention (minimal fade at 100 cycles) and single-phase as-deposited microstructure. It is believed that the excellent performance of the Sn<sub>10</sub>Bi<sub>10</sub>Sb<sub>80</sub> alloy is a result of two factors. The first is solid solution strengthening induced by substitutional dissolution of Bi and Sn in the Sb lattice, resulting in higher resistance to internal stress. The second, also related to the dissolution of Bi and Sn, is a change in the Sb chemical potential, resulting in a higher number of distinct sodiation processes, each with a much smaller material expansion compared to pure Sb, resulting in lower internal stress.

## 2.4 Experimental Section

### 2.4.1 Materials and Equipment

Si wafers (111) orientation, prime grade, p-type, B-doped, resistivity <0.005 Ω·cm, thickness = 500-600 μm) were purchased from WRS Materials, Inc. The Sn, Bi, and Sb sputtering targets were purchased from Plasmaterials, Inc. Fluoroethylene carbonate (99%) and metallic sodium (99.9%) were purchased from Sigma-Aldrich, while sodium perchlorate (NaClO<sub>4</sub>, >98%), ethylene carbonate (99% purity), diethyl carbonate (>99%), and acetonitrile (99%) were purchased from Alfa Aesar. Trilayer polypropylene-polyethylene-polypropylene separators (porosity of 39%) were purchased from Celgard, and stainless steel spacers, springs, and caps were obtained from MTI Corporation. The sputtering system used was an ATC Orion 8, AJA

International Inc. The argon gas used was 5 N purity and was supplied by Praxair Canada Inc. The microbalance, a Mettler Toledo, XP6U, had an accuracy of 0.1  $\mu\text{g}$ . Electrochemical measurements were done using an Arbin BT2000 battery testing system.

### 2.4.2 Electrode Preparation and Battery Assembly

Nominally 100 nm-thick films were (co)sputtered on highly conductive p-type silicon wafers at room temperature. Si wafers were cleaned sequentially for 10 min by sonication in methylene chloride ( $\text{CH}_2\text{Cl}_2$ ), acetone, and methanol before using for sputtering. As previously shown, Si does not have any capacity for Na at room temperature,<sup>153</sup> which is verified in Figure 2.12. Capacities are given as both areal capacity ( $\text{mAh}/\text{cm}^2$ ), which is nearly zero, and gravimetric capacity, based on the average weight of an alloy film. The weight for each sample composition is listed in Table 2.7 and varies between 48 and 83  $\mu\text{g}$  depending on the composition. The contribution of the Si substrate is never higher than  $\sim 2$   $\text{mAh}/\text{g}$ . Bi and Sn were deposited with DC-magnetron sputtering, while Sb deposition was performed by radio frequency-magnetron sputtering. Sputtering was carried out with continuous substrate rotation under argon gas at a pressure of 5 mTorr. The deposition rate of each element is 0.01–0.1 nm/s, and these rates were adjusted as necessary to achieve the desired compositions. Throughout the paper, different films are labeled by their nominal composition in molar percentages; for example, **Sn80Bi10Sb10** would have a nominal molar composition of 80% Sn, 10% Bi, and 10% Sb.

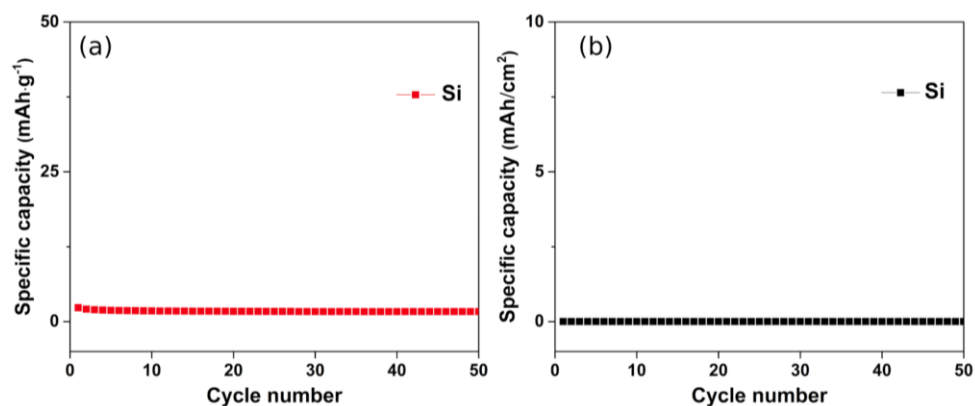


**Figure 2.12.** Specific Na storage capacity versus cycle number of the Si substrate used in this study. (a) Normalized to the average weight of a 100 nm thin film used in this study. (b) Normalized to the surface area of the substrate.

**Table 2.7.** Average Weight and Standard Deviation for Each Composition Based on 6 Different Samples.

Sample	Average weight (mg)	Standard deviation (mg)
Sn	0.0485	0.0004
<b>Sn80Bi10Sb10</b>	0.0538	0.0014
<b>Sn60Bi20Sb20</b>	0.0590	0.0006
<b>Sn50Bi25Sb25</b>	0.0586	0.0005
Bi	0.0830	0.0012
Sn10 <b>Bi80</b> Sb10	0.0742	0.0013
Sn20 <b>Bi60</b> Sb20	0.0715	0.0019
Sn25 <b>Bi50</b> Sb25	0.0692	0.0009
Sn33Bi33Sb33	0.0621	0.0012
Sb	0.0499	0.0004
Sn10Bi10 <b>Sb80</b>	0.0563	0.0008
Sn20Bi20 <b>Sb60</b>	0.0559	0.0023
Sn25Bi25 <b>Sb50</b>	0.0580	0.0010

Sodium half-cells were assembled using pure sodium foil as the counter electrode, trilayer polypropylene-polyethylene-polypropylene separators, stainless steel spacers, springs, and caps. The electrolyte used was 1 M sodium perchlorate dissolved in a mixture of ethylene carbonate and diethyl carbonate with a volume ratio of 1:1, mixed with fluoroethylene carbonate (5% by weight). The assembly process was done in an argon-filled glovebox with an oxygen level below 1 ppm and moisture level below 0.1 ppm.

### 2.4.3 Electrochemical Testing

Galvanostatic charge-discharge tests were carried out using a potential range of 0.01–2 V vs Na/Na<sup>+</sup>. Cycled batteries were disassembled in the glovebox and soaked in acetonitrile for 12 h to remove residual electrolyte.

### 2.4.4 Characterization

Scanning electron microscopy (SEM) analysis was carried out with a Hitachi S-4800 field emission SEM (Hitachi, Clarksburg, MD) at 15 kV and 20  $\mu$ A. X-ray diffraction (XRD) analysis was performed on an AXS diffractometer (Discover 8, Bruker, Madison, WI) with Cu-K $\alpha$  radiation ( $\lambda = 1.5406 \text{ \AA}$ ). The diffractometer was equipped with a Histar general-area two-dimensional detection system (GADDs) with a sample-detector distance of 15 cm. Phases were identified using the database of EVA software. The as-deposited film compositions were verified using X-ray photoelectron spectroscopy (XPS). The XPS spectra are shown in Figure 2.2 and the calculated compositions, listed in Table 2.8, are close to nominal (less than 5 at% difference). XPS was performed on an ULTRA (Kratos Analytical) spectrometer under ultrahigh vacuum ( $10^{-9}$  Torr), using monochromatic Al K $\alpha$  radiation ( $h\nu = 1486.6 \text{ eV}$ ) and operating at 210 W. The XPS data were analyzed with CasaXPS software.

**Table 2.8.** Sample Compositions of As-deposited Alloy Electrodes, Derived from XPS Spectra.

Sample	Sn (at%)	Bi (at%)	Sb (at%)
<b>Sn80Bi10Sb10</b>	76	13	11
<b>Sn60Bi20Sb20</b>	62	20	18
<b>Sn50Bi25Sb25</b>	57	22	21
Sn10 <b>Bi80</b> Sb10	33	36	31
Sn20 <b>Bi60</b> Sb20	12	75	13
Sn25 <b>Bi50</b> Sb25	23	55	22
Sn33 <b>Bi33</b> Sb33	26	50	24
Sn10Bi10 <b>Sb80</b>	11	8	81
Sn20Bi20 <b>Sb60</b>	17	25	58
Sn25Bi25 <b>Sb50</b>	26	27	47

## Chapter 3<sup>‡</sup>

# **$\beta$ -SnSb for Sodium Ion Battery Anodes: Phase Transformations Responsible for Enhanced Cycling Stability Revealed by In-situ TEM**

### **3.1 Introduction**

Alloyed materials possessing a nanoscale microstructure may exhibit improved resistance toward the severe problem of mechanical fracture and pulverization induced by internal stress buildup during repeated volume expansion and contraction.<sup>154–158</sup> Nanostructured alloyed materials are expected also to possess much better kinetics compared to their coarser counterparts due to shorter diffusion distances<sup>159–163</sup> and, in some cases, metastable phases.<sup>164</sup> In this work, we use in situ TEM to probe the sodiation and desodiation of the promising  $\beta$ -SnSb alloy, which is composed of two elements that are highly active for sodiation. The  $\beta$ -phase SnSb intermetallic is one of the most interesting binary systems in terms of structural stability and facile sodiation kinetics.<sup>52,165–168</sup> To date, however, the underlying reasons for the promising cycling stability of the  $\beta$ -SnSb have not been identified, and there is incomplete understanding of the sodiation–desodiation sequence. Per the room-temperature binary equilibrium phase diagram of Sb–Sn in the range of 46–48 atom %, there is a cubic rock salt ordered solid solution intermetallic ( $\beta$ -SnSb) with an enthalpy of formation of about  $-3$  kJ/mol.<sup>169,170</sup> Reports based on combined XRD and Mössbauer studies highlight the presence of the  $\text{Na}_3\text{Sb}$  phase at terminal sodiation and an amorphous NaSb phase at lower Na content.<sup>166</sup> For the  $\beta$ -SnSb alloy, however, XRD alone is difficult to interpret due to the highly broadened peaks of the nanocrystalline/ amorphous phases that form.<sup>171</sup> In situ TEM has been shown to be a highly powerful technique for site-specific analysis of sodiation-induced phase transformations, even when the phases are truly nanostructured.<sup>172,173</sup> Here we

---

<sup>‡</sup> The contents of this chapter have been reproduced and/or adapted from the following publication: Xie, H.; Tan, X.; Luber, E. J.; Olsen, B. C.; Kalisvaart, W. P.; Jungjohann, K. L.; Mitlin, D.; Buriak, J. M.  $\beta$ -SnSb for Sodium Ion Battery Anodes: Phase Transformations Responsible for Enhanced Cycling Stability Revealed by In Situ TEM. *ACS Energy Lett.* **2018**, 3 (7), 1670–1676.

analyze the reversible sodiation–desodiation reactions of  $\beta$ -SnSb by this technique and connect these results to the electrochemical performance of  $\beta$ -SnSb films as anodes for SIBs.

### 3.2 Results and Discussions

To investigate the SnSb system, the following films were prepared via sputtering: cosputtered SnSb (1:1 mole fraction), bilayers of Sn(top)/Sb(bottom) and Sb(top)/Sn(bottom), and the corresponding pure elemental films. The indexed XRD patterns of the as-deposited 100 nm  $\beta$ -SnSb alloy film and of the 50 nm/50 nm Sn/Sb and Sb/Sn bilayers are shown in Figure 3.1. The combination of the thermodynamic driving force and short diffusion distances in the Sn/Sb and Sb/Sn bilayer films causes partial formation of a  $\beta$ -SnSb intermetallic even in the as-deposited state. The co-sputtered film is converted fully to the  $\beta$ -SnSb phase, with no evidence of elemental Sn or Sb. As will be demonstrated by TEM and XRD (vide infra), the Sn and Sb bilayers react during desodiation cycles to form  $\beta$ -SnSb in the desodiated state. Figure 3.2 compares the electrochemical performance of the co-sputtered SnSb film, the Sn/Sb and Sb/Sn bilayers, and the elemental Sn and Sb films. We also examined a trilayer system containing a very thin silicon interdiffusion barrier sandwiched between the tin and antimony, Sb(49 nm)/Si(2 nm)/Sn(49 nm). Figure 3.2a–c shows the galvanostatic charge–discharge curves of the cosputtered SnSb film and of the bilayers at cycles 2, 10, and 50. Galvanostatic data for baseline elemental Sn, Sb, and the trilayer Sn/Si/Sb films are shown in Figure 3.3. It is evident that the galvanostatic voltage versus capacity plateaus for the bilayers are very similar to that of the co-sputtered SnSb alloy film, especially in later cycles, all the while being distinct from both the elemental Sn and Sb films. The shapes and positions of the plateaus for the co-sputtered SnSb versus Sn/Sb bilayers show only minor differences in the region of the reaction overpotentials.

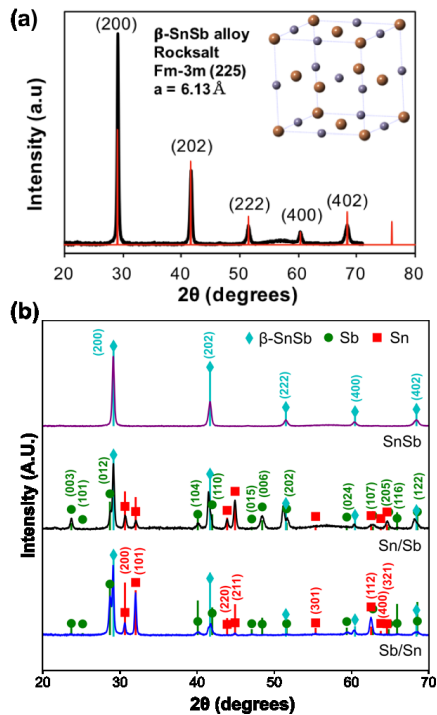


**Figure 3.1.** (a) Simulated diffraction patterns of  $\beta$ -SnSb alloy, indicating that  $\beta$ -SnSb has a cubic rocksalt crystal structure. (b) Indexed X-ray diffraction patterns of the as-deposited 100 nm  $\beta$ -SnSb alloy film and the Sn/Sb and Sb/Sn bilayer films.

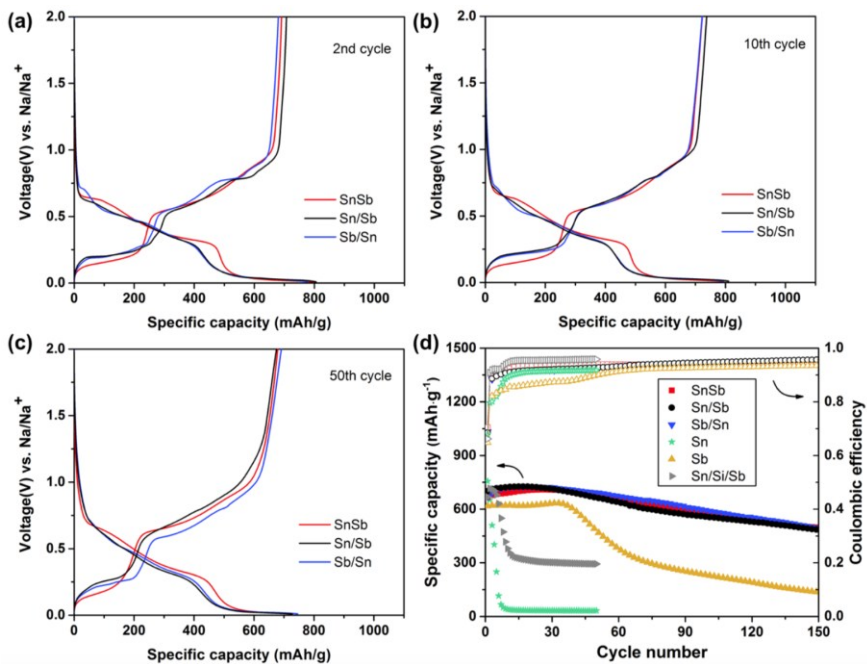


**Figure 3.2.** Galvanostatic charge–discharge curves of co-sputtered SnSb and bilayer Sn/Sb and Sb/Sn at cycles (a) 2, (b) 10, and (c) 50. (d) Associated cycling performance and CEs, which also include baseline elemental films of Sn and Sb as well as a trilayer Sn/Si(2 nm)/Sb film. All batteries were tested at 200 mA/g.

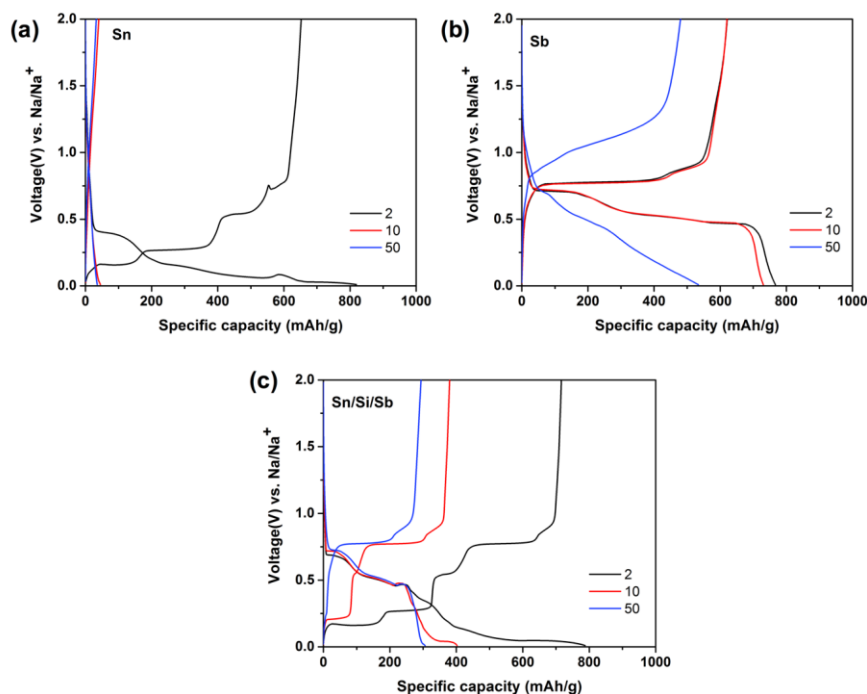


**Figure 3.3.** Galvanostatic sodiation-desodiation voltage profiles of (a) Sn, (b) Sb, and (c) Sn/Si(2 nm)/Sb films at cycles 2, 10, and 50.

Figure 3.2d shows the cycling performance and the associated Coulombic efficiency (CE) of all of the films tested. It should be noted that the elemental Sn and Sb films degrade rapidly—the Sn immediately and the Sb after  $\sim 40$  cycles. The co-sputtered SnSb and Sn/Sb bilayer films exhibit much better capacity retention, with similar cycling stability with 70% capacity retention after 150 cycles. In fact, they demonstrate analogous initial reversible capacity near 700 mAh/g, increasing to 740 mAh/g over the first 20 cycles and slowly decaying afterward. The Sn/Sb bilayer with a sandwiched 2 nm Si interdiffusion barrier does not show the same level of extended stability, fading rapidly after fewer than 10 cycles. This result with the trilayer sandwich suggests that the  $\beta$ -SnSb alloy reaction sequence is an essential microstructural feature necessary for the material to withstand repeated cycling.

XRD analysis of the films after extended cycling reveals which phases are formed preferentially, as shown in Figure 3.4. After 45 cycles, the only phase detected for the co-sputtered SnSb film in the desodiated state was the  $\beta$ -SnSb intermetallic (Figure 3.4a). After 150 cycles, the SnSb, Sn/Sb, and Sb/Sn bilayer films all show the

presence of the  $\beta$ -SnSb intermetallic, although crystalline Sn also is observed; crystalline Sb, however, was not seen even after 150 cycles. Two possible scenarios could explain these observations: (i) upon extended cycling, the composition of  $\beta$ -SnSb may become more Sb-rich, resulting in precipitation of Sn as a second phase, or (ii) cycling may induce precipitation of Sb, which could remain amorphous in the desodiated state and hence remain invisible to XRD. The presence of a secondary Sn phase may be the explanation for the observed onset of capacity decay at around 150 cycles; as per the cycling results of elemental Sn, the crystalline Sn phase is highly unstable during cycling. The presence of Sn as a separate phase could be the initiation point for electrode failure, which is manifested as fracture and largescale separation of the film from the current collector in pure Sn films.<sup>49,158</sup> It appears that the key to cycling stability is the presence of  $\beta$ -SnSb in the desodiated state because near room temperature elemental Sn creeps at much higher rates than its solid solution alloy counterparts.<sup>174</sup>

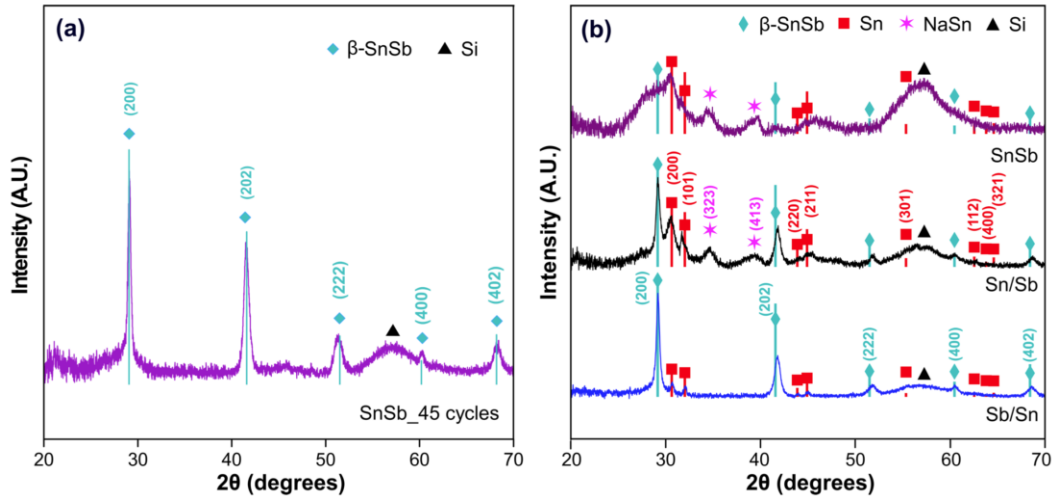


**Figure 3.4.** (a) Indexed XRD pattern of the SnSb film after 45 cycles in the desodiated state showing the presence of only  $\beta$ -SnSb, without either Sn or Sb peaks being present. (b) Indexed XRD patterns of SnSb, Sn/Sb, and Sb/Sn after 150 cycles, indicating the even after extensive cycling  $\beta$ -SnSb is still present in the desodiated state, although the crystalline Sn phase is also present. The broad peak at  $2\theta \approx 57^\circ$  is from the (311) reflection of the Si substrate. This peak is broadened because the sample is close but slightly out of the Bragg condition, which is due to the in-plane rotation of the single-crystal substrate.

To provide detailed insights into the nature of the sodiation–desodiation of SnSb films, in situ TEM analysis was carried out on a co-sputtered SnSb film and both Sn/Sb bilayer films. Figure 3.5 shows the image of a co-sputtered SnSb film analyzed

at the first cycle of sodiation–desodiation. To sodiate and desodiate the film, a voltage of  $-0.5$  and  $+5$  V vs Na was applied, respectively. The bright-field TEM (BF-TEM) micrographs of the pristine SnSb film deposited on Ge/TiN nanowires revealed three distinct layers, from external to internal: the SnSb film, the TiN barrier layer, and the supporting Ge nanowire. The SnSb was not expected to be reactive with the stable TiN underlayer (vide infra). By comparing experimental selected area diffraction (SAED) patterns of pristine SnSb with the simulated pattern shown (Figure 3.5), it was confirmed that the as-deposited SnSb film is a polycrystalline single-phase  $\beta$ -SnSb intermetallic with a rocksalt cubic crystal structure ( $Fm\bar{3}m$  [225]).

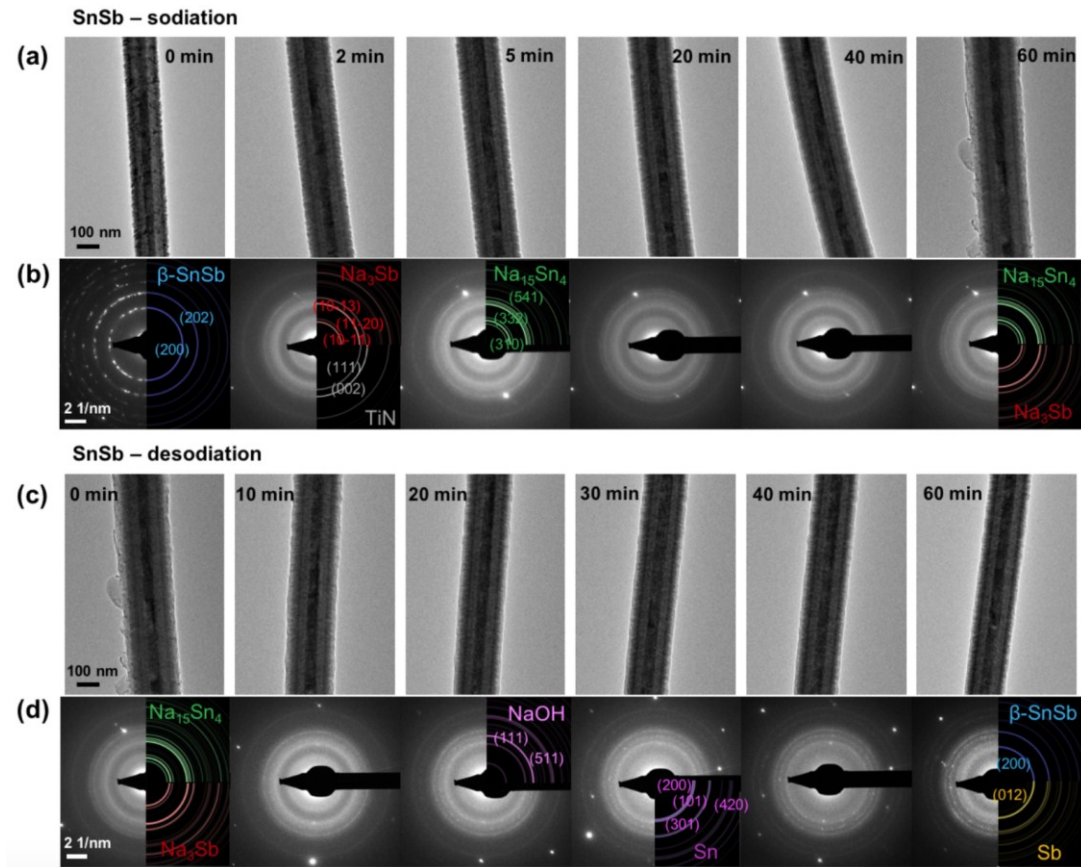


**Figure 3.5.** In situ TEM analysis of the sodiation–desodiation of a co-sputtered SnSb film during the first cycle. (a) Bright-field micrographs and (b) associated measured electron diffraction patterns as well simulations during sodiation. (c,d) Same analyses during desodiation.

As expected, inspection of the BF-TEMs (Figure 3.5) shows that the diameter of the nanowire increases during sodiation due to Na uptake in the SnSb film. The

volume expansion is measured as a function of (de)sodiation time and is shown in Figure 3.6a (see the experimental section and Figure 3.6b,c for details on how volume expansion was measured). We see that there is a very rapid initial volume expansion of 85% (2 min), followed by a gradual increase to 135% (40 min), and then a final more rapid increase to 210% (60 min). This data suggests that the Sb sodiates first (as is expected from the equilibrium sodiation potentials), while the Sn begins to sodiate much more slowly and is likely a mixture of amorphous- $\text{Na}_x\text{Sn}_y$  and crystalline- $\text{Na}_{15}\text{Sn}_4$  phases by the end of 60 min of in situ sodiation. This hypothesis is validated by analyzing the TEM micrographs for the sodiation of Sn/Sb bilayers (Figure 3.7), where the Sn particles on the free surface experience only a volume increase of  $\sim 100\%$  after 65 min of in situ sodiation, which is much less than the 420% of fully sodiated Sn. Therefore, if we assume that the Sb is fully sodiated (290%) after 60 min and the Sn has experienced a 100% volume increase, the estimated volume expansion would be  $\sim 190\%$  (see the experimental section for calculations details), which agrees well with the measured value of 210%.

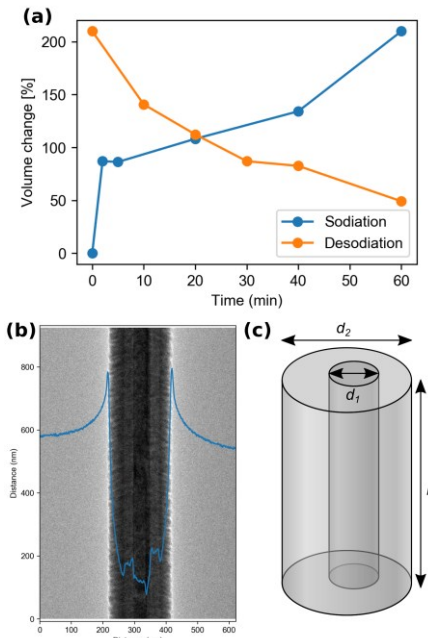


**Figure 3.6.** (a) Volume changes of SnSb film during in-situ (de)sodiation as a function of time. Sodiation is done potentiostatically at  $-0.5$  V and desodiation at  $+5$  V. (b) BF-TEM micrograph of an in-situ sodiated SnSb film, with the image rotated so that the wire axis is parallel to the vertical axis. Overlaid on the image is the average image intensity along the vertical direction. (c) Schematic of geometry assumed for volume calculations of the SnSb film.

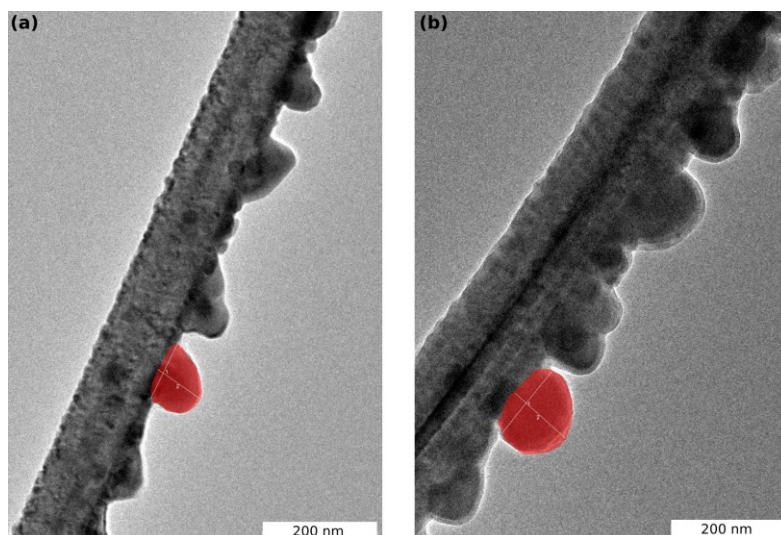


**Figure 3.7.** (a) BF-TEM of Sn/Sb multilayer (25 nm/25 nm) in the as-deposited state, with a single Sn particle marked in red. (b) The same particle marked in red after 65 min of in-situ sodiation.

After 2 min of sodiation, the  $\beta$ -SnSb pattern disappeared. New peaks centered at around  $2.4$  and  $3.6 \text{ nm}^{-1}$  were observed, corresponding to the (1011) and (1120)/(1013) reflections of  $\text{Na}_3\text{Sb}$  (P63/mmc [194]). The sharp peaks centered at  $4.0$  and  $4.7 \text{ nm}^{-1}$  correspond to the (111) and (002) reflections of the TiN barrier (Fm $\bar{3}$ m [225]). These remain invariant during sodiation–desodiation cycling, confirming that TiN is indeed nonreactive toward Na and thus serving as a useful in situ calibration marker. The single-crystal Ge nanowire is purposely off its zone axis. After 5 min of sodiation, three peaks at  $2.5$ ,  $3.6$ , and  $5.0 \text{ nm}^{-1}$  appear in the SAED. These features correspond to (310), (332), and (541) reflections of the cubic  $\text{Na}_{15}\text{Sn}_4$  phase (I $\bar{4}$ 3d [220]). The (541) peak at  $5.0 \text{ nm}^{-1}$ , in particular, cannot be ascribed to any other phase besides  $\text{Na}_{15}\text{Sn}_4$ . Its position is isolated from any  $\text{Na}_3\text{Sb}$  peaks, making it the most clearly visible feature. The relative intensity of these peaks increases after 5–60 min of sodiation. At longer times, the relative intensity remains approximately constant, indicating that the sodium content of the material has reached its maximum.

During desodiation, the (541) reflection of  $\text{Na}_{15}\text{Sn}_4$ , the last to appear in the SAED pattern, disappeared first after 10 min, as shown in Figure 3.8, further supporting the attribution of this feature to the (541) reflection of  $\text{Na}_{15}\text{Sn}_4$ . The overlapping peaks between  $2.0$  and  $3.0 \text{ nm}^{-1}$  significantly diminished after 30 min, and two main peaks and a small peak of Sn at  $3.4$ ,  $3.6$ , and  $7.7 \text{ nm}^{-1}$ , corresponding to the (200), (101),

and (420) reflections, respectively, of tetragonal Sn, were observed. The observed segregation of a small amount of  $\text{Na}_{15}\text{Sn}_4$  during sodiation, converting to elemental Sn upon desodiation, is in agreement with the XRD results (Figure 3.4).

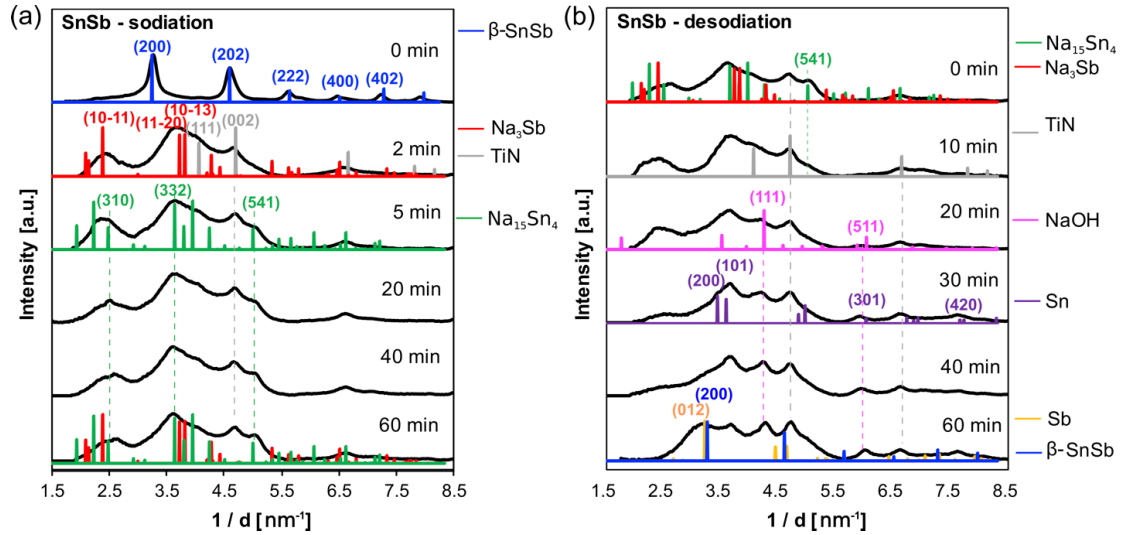


**Figure 3.8.** Azimuthally averaged in situ electron diffraction patterns (Figure 3.5) of the SnSb during (a) sodiation and (b) desodiation.

Two peaks at 4.2 and 6.0  $\text{nm}^{-1}$  also appeared after 20 min of desodiation and became more distinct as the desodiation time increased. We ascribe these peaks to the (111) and (511) reflections of orthorhombic NaOH ( $Cmcm$  [63]), which may form when the Na metal is transferred to the TEM column and may migrate quickly on the surface, along the length of the nanowire.<sup>156,175–178</sup> The peak at 6.0  $\text{nm}^{-1}$  also coincides with the (301) reflection of elemental Sn. From 30 to 60 min, the overlapping peaks centered at 2.5  $\text{nm}^{-1}$  further decreased, and the (200) peak of rocksalt  $\beta\text{-SnSb}$  and/or the (012) peak of rhombohedral Sb ( $R\bar{3}m$  [166]) near 3.2  $\text{nm}^{-1}$  was observed. As the peak obviously is broadened, this observation suggests that nanocrystalline  $\beta\text{-SnSb}$  and/or Sb forms. The assignment of this nanocrystalline feature is supported further by HRTEM micrographs of the desodiated SnSb film, shown in Figure 3.9. The interplanar distance of 0.31 nm matches the d-spacing of the {200} planes of the cubic SnSb phase. As desodiation progresses, the BF-TEM micrographs show that the sodiated SnSb film gradually shrinks as a result of extraction of Na.

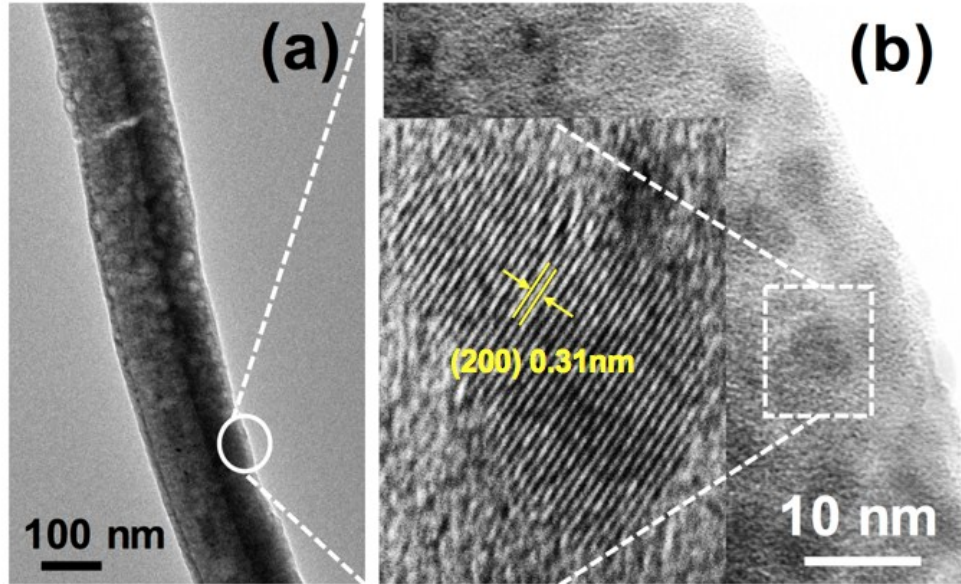


**Figure 3.9.** HRTEM analysis of the SnSb film after four in situ sodiation–desodiation cycles. (a) BF-TEM of the film and (b) corresponding HRTEM showing nanocrystallites, which are attributed to  $\beta$ -SnSb.

To study the reaction mechanism of  $\beta$ -SnSb further, multicycle in situ TEM analyses were performed, which are shown in Figure 3.10. As previously discussed, during the first cycle, the sodiation process induces segregation of the  $\beta$ -SnSb alloy by forming nanocrystalline  $\text{Na}_3\text{Sb}$  and  $\text{Na}_{15}\text{Sn}_4$  in sequence. During the first desodiation, a small amount of crystalline Sn and nanocrystalline  $\beta$ -SnSb is formed in sequence. From the second cycle onward, the phase transformations are basically consistent and reversible. Figures 3.11–3.14 show the in situ TEM characterization of Sb/Sn and Sn/Sb films during one full discharge–charge cycle. Unlike the cosputtered SnSb film, bilayer films are composed of relatively larger particles, especially for Sb/Sn, which shows the largest particle size among the three. This observation is consistent with the calculated grain size based on XRD, shown in Table 3.1. The SAED patterns show that pristine Sb/Sn and Sn/Sb films are composed of Sn, Sb, and  $\beta$ -SnSb phases. During sodiation, the same broad features observed for the SnSb film appear first after 2 min, and crystalline  $\text{Na}_3\text{Sb}$  and  $\text{Na}_{15}\text{Sn}_4$  are observed in sequence with the SAED peaks, becoming sharper over time as sodiation progresses. During desodiation,  $\text{Na}_{15}\text{Sn}_4$  decomposes first and the (200), (101), (211), and (420) peaks of

elemental Sn are visible after 30 min. Subsequently, Sb or  $\beta$ -SnSb was observed, although they are difficult to distinguish from each other. As shown in Figure 3.12, the simulated peak position of  $\beta$ -SnSb is closer to the observed center of the peak at  $3.3 \text{ nm}^{-1}$ , and therefore, the formed phase is likely  $\beta$ -SnSb.

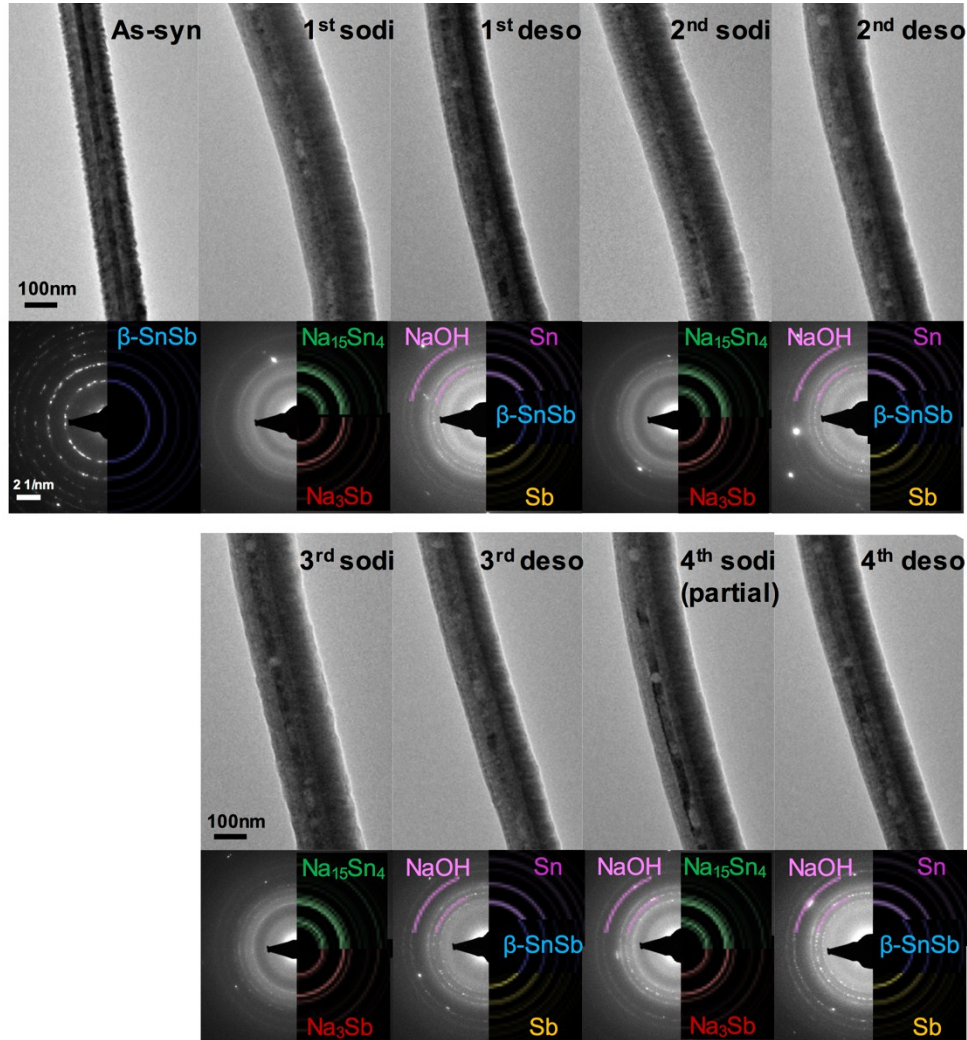


**Figure 3.10.** In situ TEM analysis of a co-sputtered SnSb film during multicycle sodation–desodiation. Each sodiation micrograph is acquired after 60 min at  $-0.5 \text{ V}$  and desodiation micrographs after 60 min at  $+5.0 \text{ V}$ . Corresponding SAED patterns and relevant simulations are shown below each micrograph.

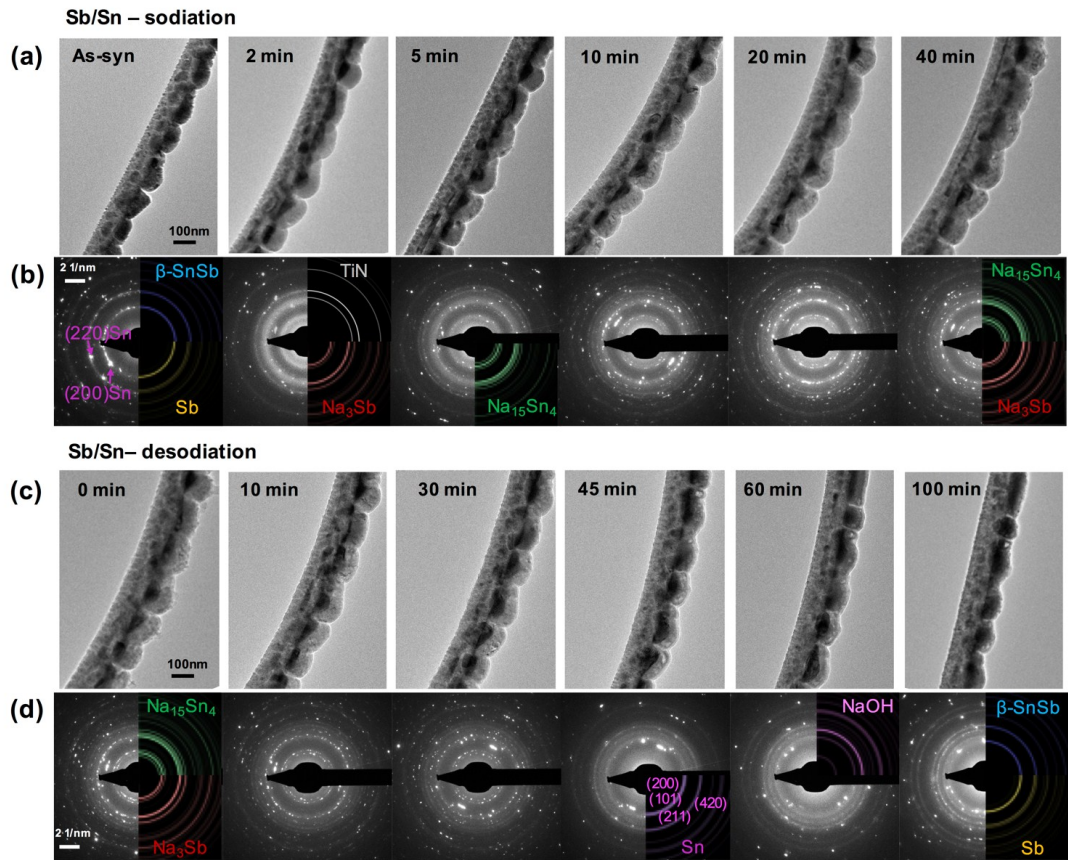


**Figure 3.11.** In situ TEM analysis of the sodiating–desodiating Sb(top)/Sn(bottom) bilayer film. Figures (a) and (b) show bright field micrographs and associated experimental and simulated SAED patterns during sodiation done potentiostatically at  $-0.5$  V. Figures (c) and (d) show these results during desodiation, done potentiostatically at  $+5.0$  V.

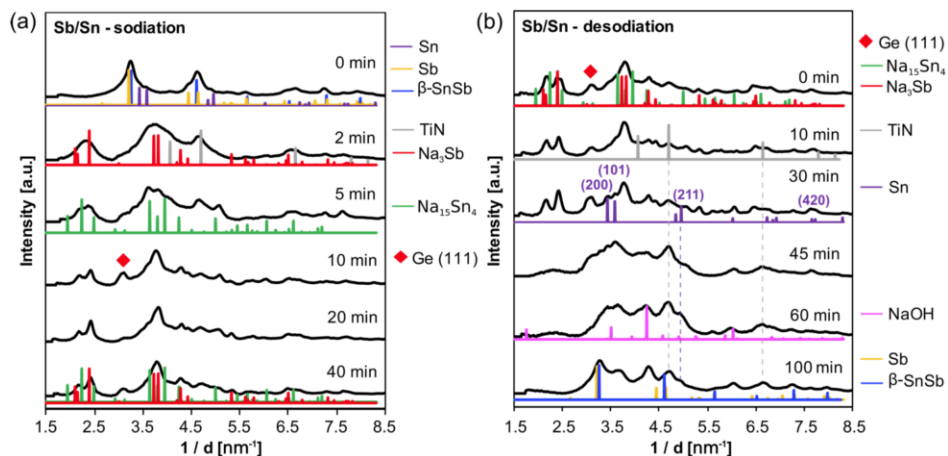


**Figure 3.12.** Azimuthally averaged in situ electron diffraction patterns (Figure 3.11) of the Sb(top)/Sn(bottom) film during first (a) sodiation and (b) desodiation. Each profile is independently normalized.

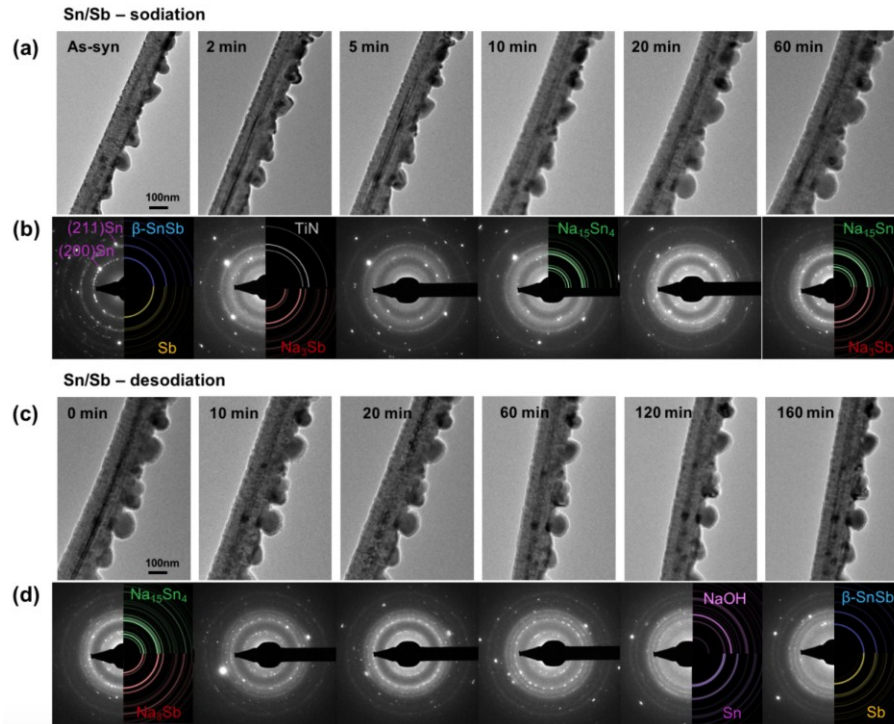


**Figure 3.13.** In situ TEM analysis of the sodiating–desodiating Sn(top)/Sb(bottom) bilayer film. Figures (a) and (b) shows bright field micrographs and associated experimental and simulated SAED patterns during sodiation done potentiostatically at  $-0.5$  V. Figures (c) and (d) show these results during desodiation, done potentiostatically at  $+5.0$  V.

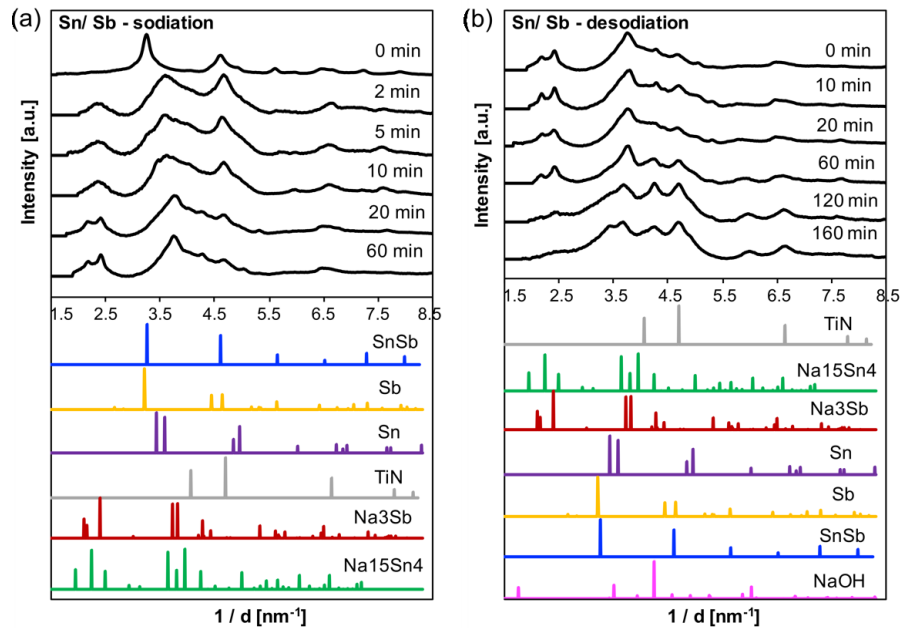


**Figure 3.14.** Azimuthally averaged in-situ electron diffraction patterns (Figure 3.13) of the bilayer Sn(top)/Sb(bottom) during first (a) sodiation and (b) desodiation. Each profile is independently normalized.

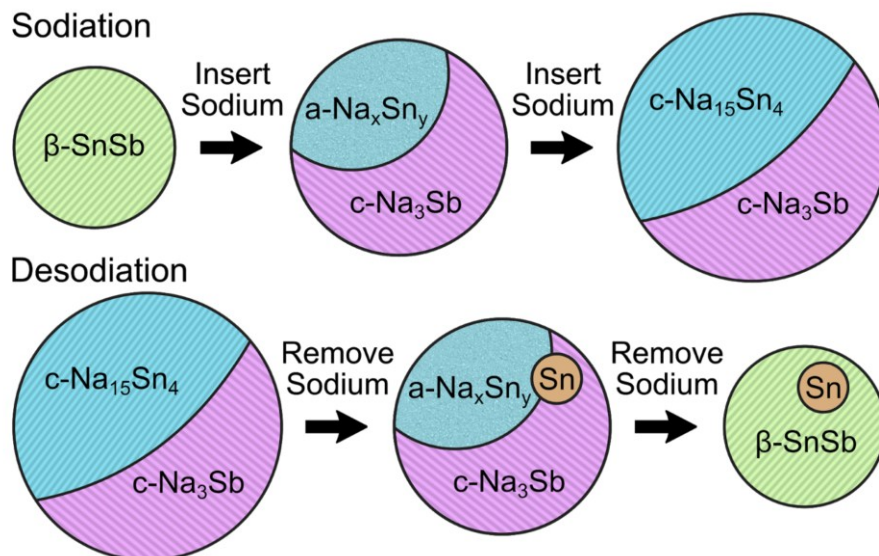
**Table 3.1.** Grain Sizes Measured by XRD via the Scherrer Equation for As-deposited Films and the Same Films After 150 Cycles of Electrochemical Battery Testing.

Composition	Phase	As-deposited film grain size [nm]	Desodiated film grain size [nm] after 150 cycles
<b>SnSb</b>	$\beta$ -SnSb	$18 \pm 7$	$1.9 \pm 0.2$
	Sn	N/A	$5.4 \pm 0.4$
	Sb	N/A	N/A
<b>Sn/Sb</b>	$\beta$ -SnSb	$41 \pm 7$	$15.3 \pm 1.0$
	Sn	$32 \pm 4$	$16.0 \pm 1.7$
	Sb	$19 \pm 6$	N/A
<b>Sb/Sn</b>	$\beta$ -SnSb	$53 \pm 9$	$10.3 \pm 1.0$
	Sn	$49 \pm 4$	$7.3 \pm 0.8$
	Sb	$18 \pm 5$	N/A

From the in situ TEM diffraction data, it appears that both Sn/Sb and Sb/Sn bilayer films followed a very similar sodiation–desodiation reaction sequence as co-sputtered SnSb. The  $\beta$ -SnSb pattern is much sharper in the desodiated Sb/Sn film compared to that for the co-sputtered SnSb, showing that it is re-formed upon desodiation. Elemental Sn is recognizable in the SAED patterns of both SnSb and Sb/Sn. Elemental Sb, on the other hand, is very hard to discern as the strongest peak in the pristine bilayer overlaps with a broadened  $\beta$ -SnSb peak, as well as that of NaOH. These results suggest that Sn/Sb bilayers mix and form  $\beta$ -SnSb during the sodiation–desodiation cycle, and do so every cycle.

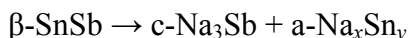
### 3.3 Conclusions

To summarize, the in situ TEM analysis results are in accordance with the XRD and the electrochemical results. On the basis of the observations and analyses above, the following overall reaction mechanism is proposed, which is illustrated in Scheme 3.1. The label “c-” denotes a crystalline phase with a distinctly identifiable diffraction pattern. The label “a-” denotes amorphous or sufficiently nanocrystalline as not to yield indexable TEM SAED or XRD reflections.

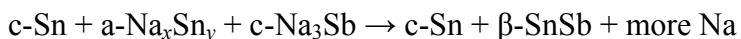


**Scheme 3.1.** Schematic illustration of the proposed phase transition of  $\beta$ -SnSb during the sodiation–desodiation cycle.

Sodiation ( $\beta$  decomposes):



Desodiation ( $\beta$  re-forms):



As written above, the sodiation process induces decomposition of the  $\beta$ -SnSb phase by forming  $\text{Na}_3\text{Sb}$  and  $\text{Na}_{15}\text{Sn}_4$  in sequence. Desodiation occurs in the  $\text{Na}_{15}\text{Sn}_4$  phase first. Then, as the  $\text{Na}_3\text{Sb}$  desodiates, the Sb reversibly alloys with the already desodiated Sn and re-forms nanocrystalline  $\beta$ -SnSb. There is a possibility of intermediate  $\text{Na}_x\text{Sb}_y$  amorphous phases as well, akin to the reaction in pure Sb films,<sup>36</sup> but these phases are very difficult to detect by TEM or XRD in a composite electrode such as the one examined here. With increased cycling number, the Sn element does not alloy fully with Sb and rather precipitates out as a distinct crystalline phase. This

process drives the composition of the remaining  $\beta$ - phase to be richer in Sb, which is thermodynamically allowable because at room temperature the  $\beta$ -phase spans 46–48 atom % Sb. Moreover, beyond these compositions, the  $\beta$ -phase may become supersaturated or precipitate out as minority Sb. To conclude, by connecting the phase diagram of SbSn intermetallics with detailed in situ TEM, electrochemistry, and ex situ XRD, a fundamental understanding of the behavior of this interesting compound as an anode for SIBs was realized, enabling optimization in future iterations.

## **3.4 Experimental Details**

### **3.4.1 Materials and Equipment**

In this study, we employed thin films prepared by sputtering as a model system. Thin films are particularly useful to address the questions analyzed in this paper since there are no binders or additives employed. High-purity Sn and Sb sputtering targets were supplied by Plasmaterials, Inc., and the sputtering system used was an ATC Orion 8, AJA International Inc. Argon gas (purity of 99.999%) was supplied by Praxair Canada Inc. Highly conductive p-type Si wafers with a resistivity of  $<0.005 \Omega\cdot\text{cm}$  (prime grade, thickness = 500–600  $\mu\text{m}$ ) were purchased from WRS Materials. Ethylene carbonate (EC, 99%), diethyl carbonate (DEC,  $>99\%$ ) and sodium perchlorate ( $\text{NaClO}_4$ ,  $>98\%$ ), were purchased from Alfa Aesar, while fluoroethylene carbonate (FEC, 99%) and metallic sodium (99.9%) were purchased from Sigma-Aldrich. Stainless steel spacers, caps, springs and trilayer polypropylene-polyethylene-polypropylene separators with a porosity of 39% (Celgard 2325) were obtained from MTI Corporation. The microbalance, a XP6U, Mettler Toledo, had a manufacturer quoted readability of 0.1  $\mu\text{g}$ .

### **3.4.2 Electrode Preparation and Electrochemical Testing**

Nominally 100 nm-thick SnSb films were deposited on silicon chips with an area of 1 x 1  $\text{cm}^2$  via DC-magnetron co-sputtering at room temperature. Bilayers were sputtered sequentially with nominal thicknesses of 50 nm for both the Sb and Sn layers. The materials are referred to as SnSb, Sb/Sn and Sn/Sb to denote the co-

sputtered alloy, the bilayer with Sb on top and Sn on top, respectively. Sputtering was carried out with deposition rates of 0.20 (5 watts) and 0.22 nm/s (5 watts) for Sn and Sb, respectively, under argon gas at a pressure of 5 mTorr. The Si substrate was shown not to have any appreciable capacity for Na at room temperature.<sup>158</sup> Prior to deposition, Si wafers were sonicated in methylene chloride (CH<sub>2</sub>Cl<sub>2</sub>), acetone, and methanol for 10 min in sequence, then dried under a stream of N<sub>2</sub>. Coin cells (CR2032-type) were assembled within an argon-filled glovebox with a moisture level below 0.1 ppm and an oxygen level below 1 ppm. Pure sodium foil was used as the counter electrode. The electrolyte used was 1 M NaClO<sub>4</sub> in EC/DEC, with a volume ratio of 1:1, mixed with FEC (5% by weight). Galvanostatic charge–discharge tests were performed at 200 mA/g for cycle life testing within a potential range of 0.01–2 V vs Na/Na<sup>+</sup>. Cycled coin cells were disassembled in a glovebox and soaked in DEC for approximately 12 h to remove residual electrolyte and salts before doing ex situ characterization. Galvanostatic charge–discharge tests were carried out using an Arbin BT2000 battery testing system.

### 3.4.3 Microstructural Characterization

Conventional bright field, dark field, and selected-area diffraction (SAED) analysis were conducted on an FEI Tecnai G2 F30 TEM (FEI, Hillsboro, OR) operating at 300 keV. X-ray diffraction (XRD) analysis was carried out using a Bruker AXS diffractometer (Discover 8) equipped with a Histar general-area two-dimensional detection system (GADDs) and using Cu-K $\alpha$  radiation ( $\lambda = 1.5406 \text{ \AA}$ ) and an incident angle of 15 degrees. The Crystallography Open Database, EVA software and simulated diffraction patterns were used for phase identification. The commercial software program Crystal Maker<sup>TM</sup> was used to simulate the crystal structures of the materials that are concerned in this work. Crystal Diffract<sup>TM</sup> and Diffraction-Ring-Profiler<sup>51</sup> were used to simulate the X-ray and electron diffraction patterns, respectively. Specifically, the following materials have been simulated:  $\beta$ -SnSb with a rocksalt cubic structure (Fm-3m, space group 225,  $a = 0.613 \text{ nm}$ ); SnSb with rhombohedral structure (R3m, space group 166,  $a = c = 0.3065 \text{ nm}$ ); Sb with a rhombohedral structure (R3m, space group 166,  $a = 0.4307 \text{ nm}$ ,  $c = 1.1273 \text{ nm}$ ); Sn

with a tetragonal structure (I41/amd, space group 141,  $a = 0.5819$  nm,  $c = 0.3175$  nm);  $\text{Na}_3\text{Sb}$  with a hexagonal structure (P63/mmc, space group 194,  $a = 0.5355$  nm,  $c = 0.9496$  nm);  $\text{Na}_{15}\text{Sn}_4$  with a cubic structure (I43d, space group 220,  $a = 1.314$  nm);  $\text{NaSb}$  with a monoclinic structure (P21/c, space group 14,  $a = 0.6802$  nm,  $b = 0.6342$  nm,  $c = 1.2484$  nm,  $\beta = 117.62^\circ$ );  $\text{NaSn}_5$  with a tetragonal structure (P421m, space group 113,  $a = 0.6285$  nm,  $c = 0.8794$  nm);  $\text{Na}_7\text{Sn}_{12}$  with a monoclinic structure (P2/c, space group 13,  $a = 1.3375$  nm,  $b = 0.9329$  nm,  $c = 1.7976$  nm,  $\beta = 90.15^\circ$ );  $\text{NaSn}$  with a tetragonal structure (I41/acd, space group 142,  $a = 1.046$  nm,  $c = 1.739$  nm);  $\text{Na}_9\text{Sn}_4$  with a orthorhombic structure (cmcm, space group 63,  $a = 0.542$  nm,  $b = 0.939$  nm,  $c = 2.962$  nm);  $\text{TiN}$  with a cubic structure (Fm-3m, space group, 225,  $a = 0.4235$  nm);  $\text{Na}_2\text{O}$  with a cubic structure (Fm-3m, space group 225,  $a = 0.555$  nm);  $\text{NaOH}$  with a orthorhombic structure (cmcm, space group 63,  $a = 0.3401$  nm,  $b = 1.138$  nm,  $c = 0.3398$  nm); and  $\text{Ge}$  with a cubic structure (Fd-3m, space group 227,  $a = 0.5758$  nm).<sup>175</sup>

### 3.4.4 In-situ TEM

A general platform was developed previously for in-situ TEM electrochemical testing to investigate electrode materials in thin film form.<sup>175</sup> An array of Ge nanowires coated with a conformal layer of titanium nitride serves as an electrically conductive, but Na-inactive, substrate to electrode materials that are subsequently deposited. SnSb films with a nominal planar thickness of 50 nm are co-sputtered onto the support surface using magnetron sputtering, as described above. Since sputtering is a highly directional physical vapor deposition process that results in shadowing, there was some local variation in film thicknesses. For labeling simplicity, the SnSb-on-TiN-on-Ge nanowire material is hereafter referred to as SnSb. This label is compared to bilayer Sn(top)/Sb(bottom) and Sb(top)/Sn(bottom) films that were studied in parallel, being labeled as Sn/Sb and Sb/Sn.

The prepared electrode was mounted onto a commercial scanning tunneling microscopy (STM) TEM holder (Nanofactory Instruments) as the working electrode. Bulk Na metal was mounted on the other side of the holder as a counter electrode. The assembly procedure was conducted in a helium-filled glovebox with moisture

and oxygen content less than 3 ppm. Next, the STM holder was then sealed in a helium-filled plastic bag and quickly transferred and loaded into the TEM column. A thin layer of Na<sub>2</sub>O and NaOH was formed during the loading procedure that serves as the solid electrolyte in the in-situ experiments. Inside the TEM, the working electrode was controlled by a piezo-positioner to contact with the counter electrode. Sodiation and desodiation was achieved by applying a bias of -0.5 V vs. Na and +5 V vs. Na to the working electrode. To minimize the electron-beam damage to the microstructure during in-situ TEM analysis, the electron beam was blanked except for when images were taken. For the magnification (i.e. 35k) we used for imaging, the typical electron dose rate was about 7.74 e<sup>-</sup>/Å<sup>2</sup> s.

### 3.4.5 Calculations

#### 3.4.5.1 SnSb Film Volume

The following method was used to estimate the volume changes of the SnSb film during in-situ (de)sodiation. First the BF-TEM images were rotated such that the nanowire is parallel to the vertical axis of the image (Figure 3.6b). Next, the image is integrated (or summed) along the vertical axis, producing a line profile of the average intensity along the vertical directions, which is overlaid on top of Figure 3.6b). Given the different contrast between the Ge-NW, TiN, and SnSb, the maxima/minima of the line profiles could be used to identify all of the relevant layer thicknesses. The volume,  $V_t$ , of the SnSb film at time t is calculated by assuming a geometry of embedded cylinders as shown in Figure 3.6c, where the volume is given by

$$V_t = \frac{\pi(d_{2,t}^2 - d_{1,t}^2)h}{4}$$

If it is assumed that the film only expands radially outwards from the nanowire axis, the percentage volume change,  $\Delta V$ , with respect to the initial volume,  $V_0$ , is given by

$$\Delta V = \left( \frac{V_t}{V_0} - 1 \right) (100\%) = \left( \frac{d_{2,t}^2 - d_{1,t}^2}{d_{2,0}^2 - d_{1,0}^2} - 1 \right) (100\%)$$

#### 3.4.5.2 Sn Volume Changes

Using the BF-TEM micrographs of the in-situ sodiated bilayer Sn/Sb films, it was

possible to obtain a rough estimate of the volume expansion of the Sn particles on the free surface of the film. Due to the irregular and non-planar nature of the Sn films it was difficult to estimate the Sn volumes accurately, however, specific particles were found to have shapes and orientations that could be used to estimate the volumes effectively. Shown in Figure 3.7a is a BF-TEM micrograph of a Sn/Sn bilayer in the as-deposited state, where a hemi-ellipsoid Sn particle is marked in red. The diameter of the base,  $b$ , and the height of particle,  $h$ , also are measured and marked. The volume of the particle,  $V$ , is assumed to be a hemi-ellipsoid given by

$$V = \frac{1}{6}\pi b^2 h$$

This same process is applied to the same particle after it has been sodiated in-situ for 65 min (Figure 3.7b). From these two images, the volume change is found to be ~100%.

### 3.4.5.3 Estimating Volume Change of SnSb Film During Sodiation

Given that SnSb phase separates into  $\text{Na}_{15}\text{Sn}_4$  and  $\text{Na}_3\text{Sb}$ , the theoretical volume of expansion of SnSb during sodiation is estimated well for a simple weighted average (or rule of mixtures) of the respective expansions of Sn and Sb. If the composition is given by  $\text{Sn}_x\text{Sb}_{1-x}$ , then the expected percentage volume expansion,  $\Delta V^*$ , of both phases being fully sodiated is given by

$$\Delta V^* = \left( \frac{xV_m^{\text{Sb}}}{xV_m^{\text{Sb}} + (1-x)V_m^{\text{Sn}}} \right) \Delta V^{\text{Sn}} + \left( \frac{(1-x)V_m^{\text{Sn}}}{xV_m^{\text{Sb}} + (1-x)V_m^{\text{Sn}}} \right) \Delta V^{\text{Sb}}$$

Where  $V_m^{\text{Sb}}$  and  $V_m^{\text{Sn}}$  are the molar volumes of Sb and Sn, and  $\Delta V^{\text{Sb}}$  and  $\Delta V^{\text{Sn}}$  are the percentage volume changes of Sb and Sn with respect to the initial volume upon terminal sodiation. Therefore, in our case of  $x = 0.5$ , the theoretical maximum volume expansion of SnSb will be

$$\Delta V^* = \left( \frac{18.19}{18.19 + 16.29} \right) (420\%) + \left( \frac{16.29}{18.19 + 16.29} \right) (290\%) = 358.6\%$$

In the scenario of partially sodiated Sn to 100% volume increase and fully sodiated Sb, the predicted volume expansion is

$$\Delta V^* = \left( \frac{18.19}{18.19 + 16.29} \right) (100\%) + \left( \frac{16.29}{18.19 + 16.29} \right) (290\%) = 189.8\%$$

## Chapter 4

### Adhesion and Surface Layers on Silicon Anodes Suppress Formation of Both c-Li<sub>3.75</sub>Si and the Solid Electrolyte Interphase

#### 4.1 Introduction

Si forms crystalline c-Li<sub>3.75</sub>Si at room temperature when it is fully lithiated.<sup>81</sup> The formation of c-Li<sub>3.75</sub>Si has been found to be detrimental to the electrode integrity because of the internal stress accompanied with the amorphous–crystalline phase transition, leading to faster capacity degradation.<sup>179–181</sup> To suppress the formation of the c-Li<sub>3.75</sub>Si phase, Obrovac et al. studied a series of alloys of Si with transition metals, including Ti, Ni, and Cu. They found that the c-Li<sub>3.75</sub>Si can be suppressed initially due to stress-voltage coupling, which results in a better capacity retention of the Si electrode.<sup>182–185</sup> By inducing stress in the Si electrode, the lithiation voltage curve of Si can be lowered by ~100–120 mV/GPa.<sup>186</sup> Since the c-Li<sub>3.75</sub>Si forms below 50 mV vs Li/Li<sup>+</sup>, a voltage of 100–120 mV will be enough to suppress its formation.<sup>82</sup> In addition, Obrovac et al. reported that the compressive stress from a substrate also can suppress the formation of the c-Li<sub>3.75</sub>Si phase temporarily.<sup>2</sup> To further minimize the formation of the c-Li<sub>3.75</sub>Si phase, we recently designed a series of alternating Si and C multilayer structures and found that the multilayer structure can minimize the formation of c-Li<sub>3.75</sub>Si phase to a degree that is proportional to the thickness ratio of Si to C layers.<sup>82</sup>

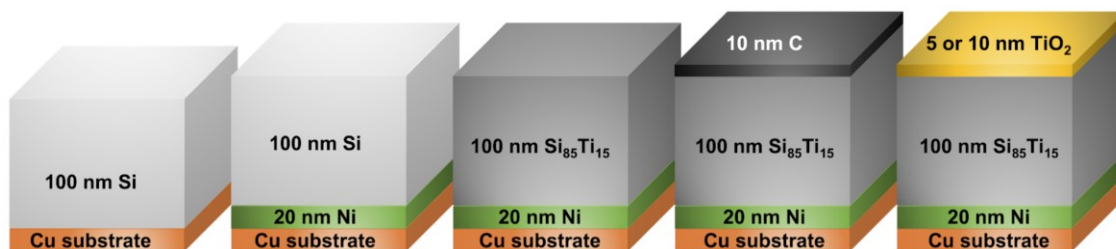
Han et al. also found that the metastable c-Li<sub>3.75</sub>Si is particularly reactive towards the electrolyte, suggesting that the formation of the c-Li<sub>3.75</sub>Si phase may exacerbate the growth of solid electrolyte interphase (SEI) on the Si electrode.<sup>180</sup> The continuous growth of SEI will deplete the electrolyte and increase the resistance of the electrode, leading to capacity loss. Capping a Si electrode with a different material, such as Al<sub>2</sub>O<sub>3</sub>,<sup>187,188</sup> C,<sup>189</sup> TiO<sub>2</sub>,<sup>190,191</sup> and TiN,<sup>190</sup> has been shown to be effective in alleviating the continuous growth of SEI and improving the Coulombic efficiency (CE) of the Si electrode. However, further understanding, detailed examination, and

comparison of different surface coatings on the formation of SEI are required to understand the origin of this effect.

In this work, we study the effect of both an adhesion layer and a surface coating on the suppression of the c- $\text{Li}_{3.75}\text{Si}$  phase and cycling stability. A proper adhesion layer or a surface coating should induce compressive stress and suppress the formation of the c- $\text{Li}_{3.75}\text{Si}$  phase. Sandwich structures of silicon and an 85:15 silicon-titanium alloy were prepared on a copper foil by sputtering, as shown in Scheme 4.1; the influence of a nickel adhesion layer on the copper and an optional surface layer of carbon or titania were examined. In addition, the effect of carbon and titania surface coatings on the growth and composition of SEI were investigated.

## 4.2 Results and Discussions

To study the effect of the adhesion layer and surface coatings, six different electrodes were prepared by magnetron sputtering on copper substrates, as shown in Scheme 4.1. X-ray diffraction (XRD) analysis of the as-deposited films shows that with the exception of the 20-nm Ni layer, the other components of the as-deposited films are amorphous (Figure 4.1).



**Scheme 4.1.** Schematic illustration of the electrodes prepared via magnetron sputtering.

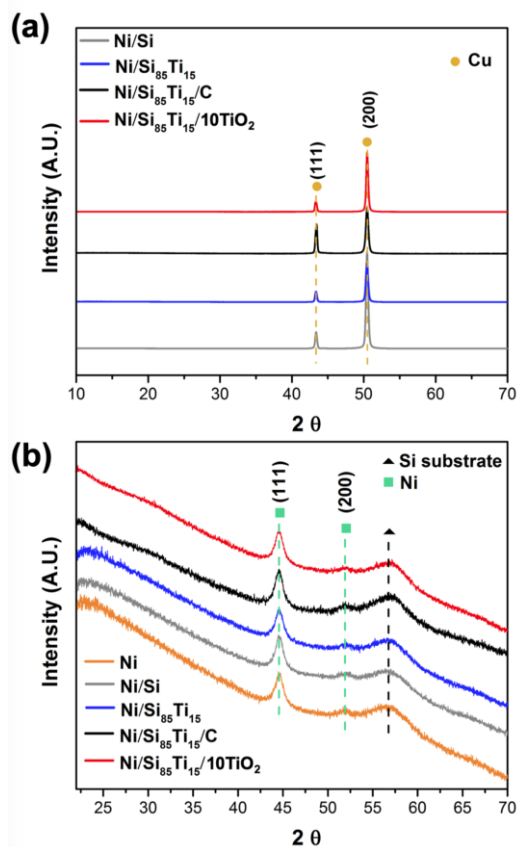


**Figure 4.1.** XRD patterns of as-deposited films on (a) Cu substrate and (b) Si substrate.

The morphologies of the as-deposited samples investigated via scanning electron microscopy (SEM) are not obviously different (Figure 4.2). However, after only 10 lithiation–delithiation cycles, the silicon film directly deposited on a Cu substrate undergoes a high degree of delamination (and an accompanying loss of electrical contact), as shown in Figure 4.3a. The Ni/Si electrode, however, shows much better integrity compared with the Si electrode, although cracks still occurred (Figure 4.3b). Compared to the Ni/Si electrode, the Ni/Si<sub>85</sub>Ti<sub>15</sub> electrode exhibits fewer cracks and better overall integrity of the film (Figure 4.3c). The Ni/Si<sub>85</sub>Ti<sub>15</sub>/C, Ni/Si<sub>85</sub>Ti<sub>15</sub>/10TiO<sub>2</sub>, and Ni/Si<sub>85</sub>Ti<sub>15</sub>/5TiO<sub>2</sub> electrodes show even less fragmentation (Figure 4.3d-f). The trend, even though it is only the tenth cycle, is consistent with the capacity retention of the electrodes, which will be discussed.

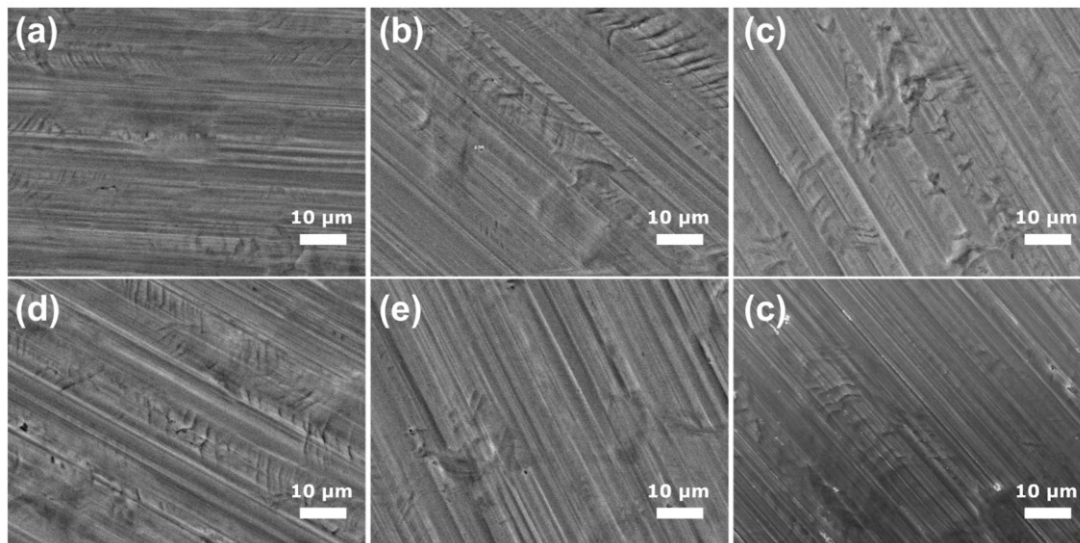


**Figure 4.2.** SEM images of as-deposited (a) Si, (b) Ni/Si, (c) Ni/Si<sub>85</sub>Ti<sub>15</sub>, (d) Ni/Si<sub>85</sub>Ti<sub>15</sub>/C, (e) Ni/Si<sub>85</sub>Ti<sub>15</sub>/10TiO<sub>2</sub>, and (f) Ni/Si<sub>85</sub>Ti<sub>15</sub>/5TiO<sub>2</sub> electrodes.

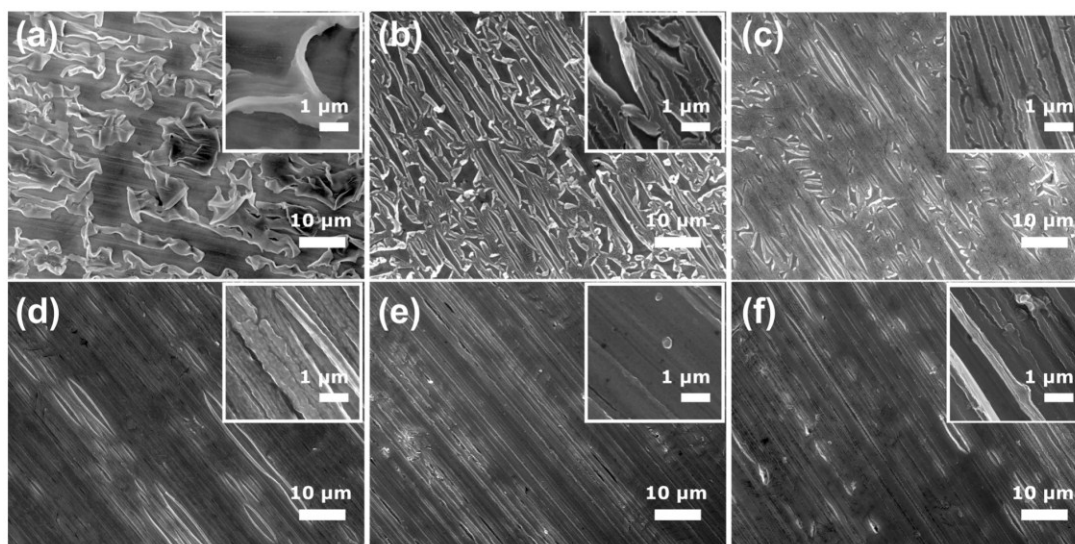


**Figure 4.3.** SEM micrographs of delithiated (a) Si, (b) Ni/Si, (c) Ni/Si<sub>85</sub>Ti<sub>15</sub>, (d) Ni/Si<sub>85</sub>Ti<sub>15</sub>/C, (e) Ni/Si<sub>85</sub>Ti<sub>15</sub>/10TiO<sub>2</sub>, and (f) Ni/Si<sub>85</sub>Ti<sub>15</sub>/5TiO<sub>2</sub> electrodes after 10 cycles.

Figure 4.4 shows the specific capacity, Coulombic efficiency (CE), and capacity retention of all six electrodes prepared. The results in Figure 4.4a-c were obtained under a constant-current constant-voltage (CCCV) protocol with a cut-off voltage of 5 mV and 1.0 V vs Li/Li<sup>+</sup> for lithiation and delithiation, respectively. The CCCV protocol is used for charging the commercial lithium-ion batteries.<sup>192</sup> A constant-voltage (CV) step also is used when performing thorough fundamental analyses to

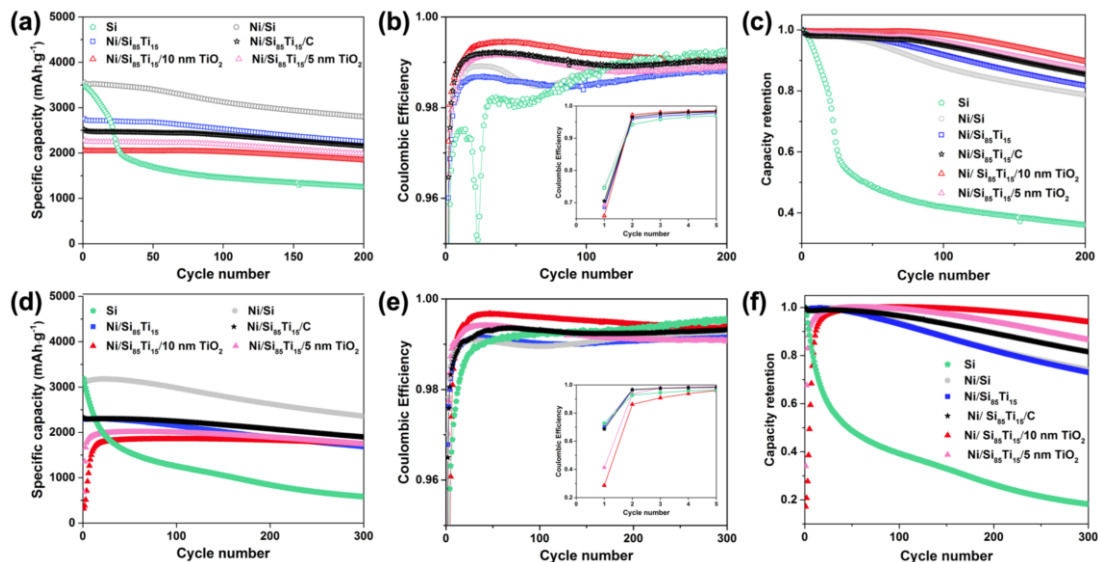


**Figure 4.4.** Specific capacity (a,d), associated Coulombic efficiency (b,e), and capacity retention (c,f) vs cycle number. The inset in (b,e) shows the CE for the first five cycles. (a–c) were tested first at a constant current step with a rate of 0.4 C, followed by a constant voltage step of 5 mV and 1.0 V for lithiation and delithiation, respectively. The current limit for constant voltage steps is 0.01 C. (d–f) were tested with only a CC step under the same rate.

investigate the inherent polarization for both charging and discharging for different compositions of Si-based electrodes.<sup>193,82</sup> As shown in Figure 4.4a–c, both Si and Ni/Si electrodes show similar specific capacities of  $\sim 3500$  mAh/g for the first cycle, which is close to the theoretical capacity of Si at room temperature (3579 mAh/g based on  $\text{Li}_{3.75}\text{Si}$ ). However, elemental Si directly deposited on a Cu substrate shows rapid capacity degradation during the first 25 cycles. In the presence of an interfacial layer of 20 nm Ni between the Cu substrate and the Si, the Ni/Si electrode exhibits a significant improvement in capacity retention, from  $\sim 38\%$  (without a Ni layer) to  $\sim 80\%$  of the initial capacity after 200 cycles. A similar improvement in capacity retention also was observed by Iaboni et al. using Ni foil as a substrate.<sup>179</sup> Ni and Si form a large number of intermetallics with stoichiometries ranging from  $\text{NiSi}_2$  to  $\text{Ni}_3\text{Si}$ , so strong bonding is expected between the Ni layer and the freshly deposited Si.<sup>62</sup> It is worth mentioning that we have not seen any signals for nickel silicides in the XRD plots, which might be due to subnanometer thicknesses of these phases or its amorphous nature if any is formed. The  $\text{Ni/Si}_{85}\text{Ti}_{15}$  electrode shows relatively better capacity retention than the Ni/Si electrode; this is expected because alloying with  $\geq 15$

at% Ti can suppress the formation of  $c\text{-Li}_{3.75}\text{Si}$  effectively, resulting in better cyclability, as reported by Wang et al.<sup>182</sup> Compared to the Ni/Si<sub>85</sub>Ti<sub>15</sub> electrode, the electrode with a 10-nm carbon capping layer, Ni/Si<sub>85</sub>Ti<sub>15</sub>/C, exhibits further improvement in capacity retention as well as CE. The improvement in CE might indicate less SEI formation. In addition, upon cycling, the samples with 5- and 10-nm coatings of TiO<sub>2</sub> both show better capacity retention and higher CE compared to the Ni/Si<sub>85</sub>Ti<sub>15</sub> electrode. The anode with the nickel adhesion layer and titania capping layer, Ni/Si<sub>85</sub>Ti<sub>15</sub>/10TiO<sub>2</sub>, shows the highest average CE and capacity retention among all the electrodes prepared.

To compare the battery performance using a constant current (CC) protocol, all the electrodes were tested and compared, as shown in Figure 4.4d-f. Compared to the CCCV results, the results carried out at CC show slightly lower gravimetric capacity, but the trends in terms of capacity retention and CE between different samples are almost the same. The addition of the nickel adhesion layer still shows a significantly better capacity retention compared to its absence. The Ni/Si<sub>85</sub>Ti<sub>15</sub>/C electrode also shows improved capacity retention and CE compared to the Ni/Si<sub>85</sub>Ti<sub>15</sub> electrode. Moreover, the Ni/Si<sub>85</sub>Ti<sub>15</sub>/10TiO<sub>2</sub> and Ni/Si<sub>85</sub>Ti<sub>15</sub>/5TiO<sub>2</sub> electrodes exhibit higher capacity retention compared with the other electrodes. In addition, it is worth mentioning that without applying CV steps (Figure 4.4d), an increase in the initial capacities is observed during the first 20 cycles for the TiO<sub>2</sub> coated samples; this might be due to the degree of diffusion of Li ions in the coating layer that improves upon cycling, presumably due to the creation of more percolation sites for Li ions in the coating layer. Applying a constant voltage step (Figure 4.4a), however, resulted in the absence of any initial uprise in the initial capacities for the TiO<sub>2</sub> coated samples. The prolonged cycling tests of the best performing electrode, i.e., Ni/Si<sub>85</sub>Ti<sub>15</sub>/10TiO<sub>2</sub>, also were carried out at higher rates of 2 and 4 C under both the CCCV and CC protocols (Figure 4.5), and they show about 80% capacity retention after 600 cycles, with a CE close to 100%. The improvements in capacity retention and CE observed in charge–discharge cycling tests at 0.4 C indicate that the Ni adhesion layer and C/TiO<sub>2</sub> surface coatings play important roles in cycling stability and SEI growth.

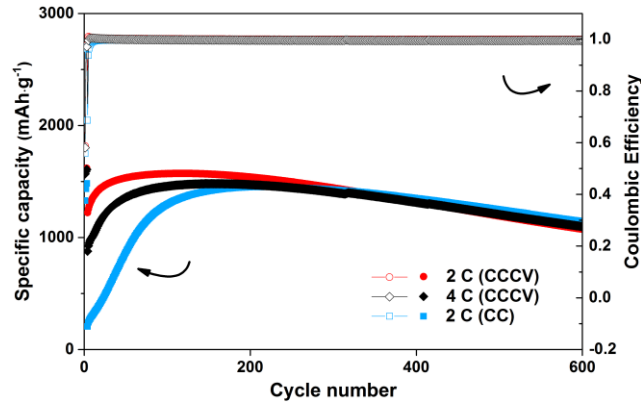


**Figure 4.5.** Specific capacity and associated Coulombic efficiency vs cycle number for the Ni/Si<sub>85</sub>Ti<sub>15</sub>/10TiO<sub>2</sub> electrode tested at 2 or 4 under both CC and CCCV protocol. The samples were tested first at 0.1 C for three cycles, then the testing rate was increased to 2 or 4 C. For the CV step, the limit current is one-tenth of the rate of the CC step, (e.g., 0.2 C for 2 C at the CC step).

Figure 4.6 shows the differential capacity plots ( $dQ/dV$  vs voltage) associated with the results in Figure 4.4a-c (their corresponding galvanostatic charge–discharge curves can be found in Figure 4.7). All electrodes exhibit two broad peaks during lithiation and delithiation at the second cycle, which is a typical behavior of amorphous silicon.<sup>194,195</sup> After 18 cycles, Si shows a sharp peak at around 0.42 V vs Li/Li<sup>+</sup>, which is attributed to the formation of c-Li<sub>3.75</sub>Si, a phase that is believed to be detrimental to the film integrity.<sup>82,179,180</sup> By adding the 20 nm-thick Ni adhesion layer, the onset of this c-Li<sub>3.75</sub>Si peak occurs after ~35 cycles, as shown in Figure 4.6 b. The suppression of the c-Li<sub>3.75</sub>Si phase likely is due to the compressive stress induced by the strong bonding between Ni and Si.<sup>179</sup> The Ni/Si<sub>85</sub>Ti<sub>15</sub> electrode starts to show the c-Li<sub>3.75</sub>Si peak after around 42 cycles, while the Ni/Si<sub>85</sub>Ti<sub>15</sub>/C, Ni/Si<sub>85</sub>Ti<sub>15</sub>/10TiO<sub>2</sub>, and Ni/Si<sub>85</sub>Ti<sub>15</sub>/5TiO<sub>2</sub> electrodes show onsets for this peak after around 65, 62, and 65 cycles, respectively. It has been proven that the capacity retention is correlated to the formation of c-Li<sub>3.75</sub>Si by Wang et al.,<sup>179,182,82</sup> which might explain our improved capacity retention from Si to Ni/Si as well as the further improvement by the inclusion of Ti and top coatings of carbon and TiO<sub>2</sub>.

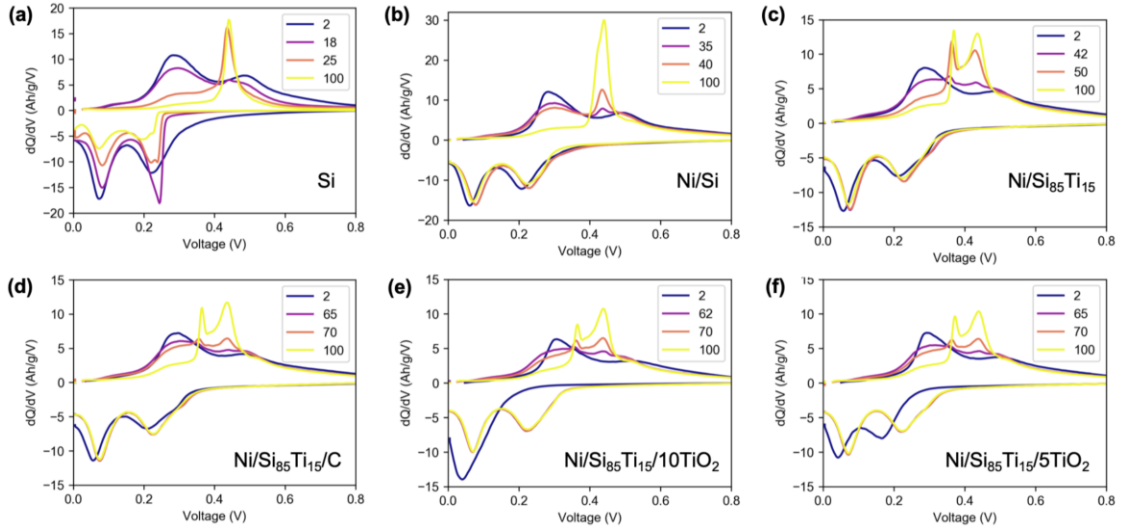


**Figure 4.6.** Differential capacity vs voltage of (a) Si, (b) Ni/Si, (c) Ni/Si<sub>85</sub>Ti<sub>15</sub>, (d) Ni/Si<sub>85</sub>Ti<sub>15</sub>/C, (e) Ni/Si<sub>85</sub>Ti<sub>15</sub>/10TiO<sub>2</sub>, and (f) Ni/Si<sub>85</sub>Ti<sub>15</sub>/5TiO<sub>2</sub> electrodes for selected cycles tested at CCCV protocol. The corresponding galvanostatic charge–discharge curves are shown in Figure 4.7.

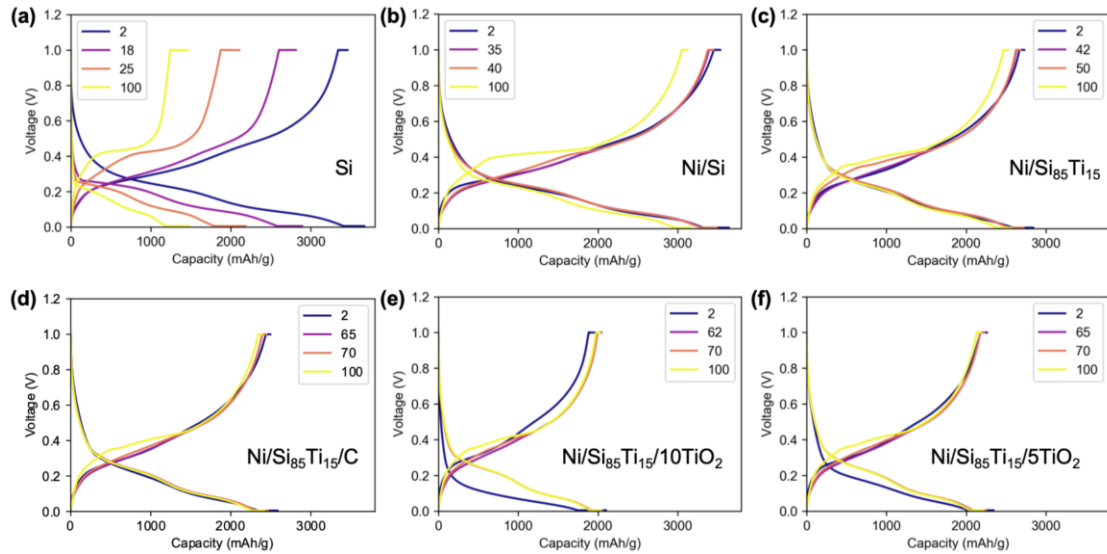


**Figure 4.7.** Galvanostatic charge–discharge curves of (a) Si, (b) Ni/Si, (c) Ni/Si<sub>85</sub>Ti<sub>15</sub>, (d) Ni/Si<sub>85</sub>Ti<sub>15</sub>/C, (e) Ni/Si<sub>85</sub>Ti<sub>15</sub>/10TiO<sub>2</sub>, and (f) Ni/Si<sub>85</sub>Ti<sub>15</sub>/5TiO<sub>2</sub> electrodes for selected cycles. The results are tested at CCCV protocol and associated with the results presented in Figure 4.6.

To investigate the correlation between capacity degradation and the appearance of the c-Li<sub>3.75</sub>Si peak further, the area of this peak at different cycles was fitted (see Figure 4.8 for details) and plotted with the capacity retention, as shown in Figure 4.9.

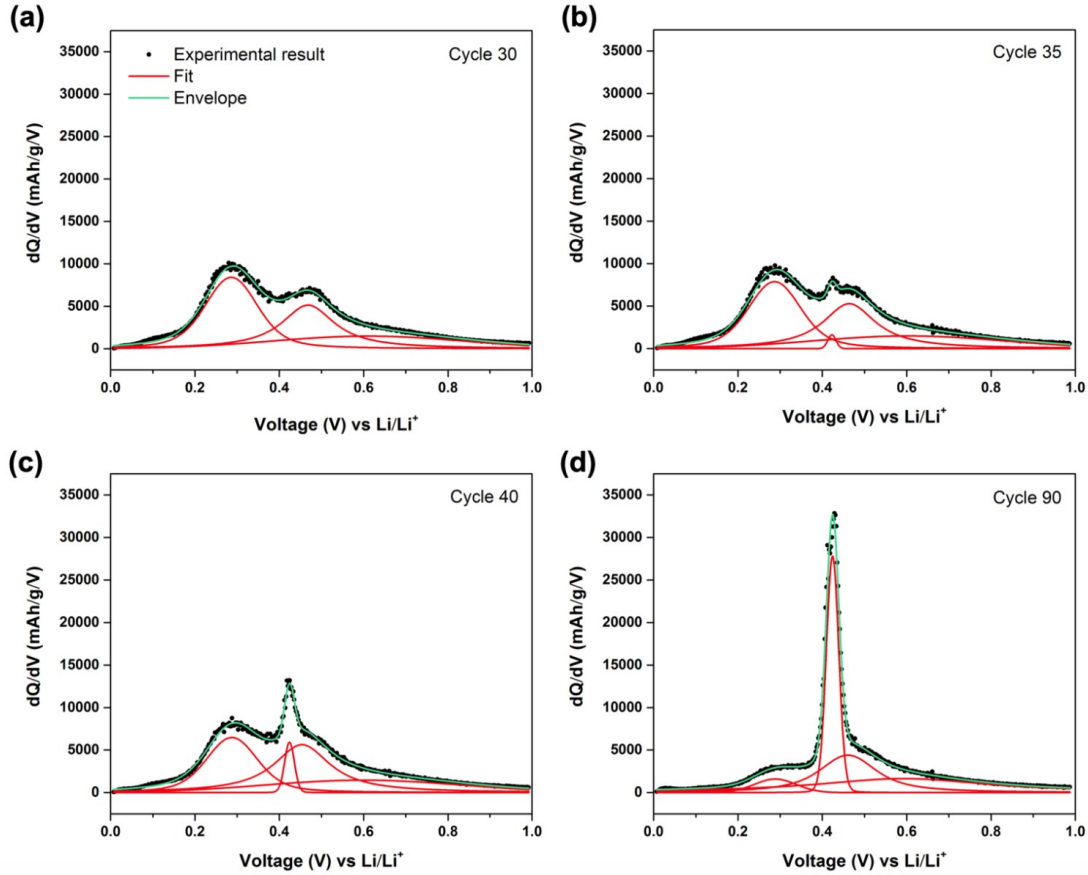


**Figure 4.8.** Curve fitting of the delithiation branch in the  $dQ/dV$  plots of the Ni/Si electrode for cycle 30, 35, 40, and 90.

The area of the  $c\text{-Li}_{3.75}\text{Si}$  peak was normalized to the weight of Si in the film as expressed below:

$$\text{Normalized Area of the } c\text{-Li}_{3.75}\text{Si peak} = \frac{\text{Fitted area of the } c\text{-Li}_{3.75}\text{Si peak}}{\text{Weight fraction of Si in the electrode}}$$

As shown in Figure 4.9a, the capacity retention of the Si degrades dramatically before the onset of the  $c\text{-Li}_{3.75}\text{Si}$  peak; this degradation is due to the delamination of the Si film, as observed in Figure 4.3a. For the other electrodes, the  $c\text{-Li}_{3.75}\text{Si}$  peak starts to appear before the inflection point in the capacity retention curve, suggesting that the formation of the  $c\text{-Li}_{3.75}\text{Si}$  peak is not correlated linearly to the capacity degradation. This observation may be due to the fact that when the  $c\text{-Li}_{3.75}\text{Si}$  phase begins to appear, the expanded Si still does not lose its electrical contact right away. Moreover, the Ni/Si electrode shows a larger area of the  $c\text{-Li}_{3.75}\text{Si}$  peak compared to

Si but better capacity retention, as shown in Figure 4.9a. Similarly, the Ni/Si<sub>85</sub>Ti<sub>15</sub> electrode also shows a relatively larger area of the c-Li<sub>3.75</sub>Si peak compared to the Ni/Si electrode but has better capacity retention (Figure 4.9). In contrast, the Ni/Si<sub>85</sub>Ti<sub>15</sub>/C, Ni/Si<sub>85</sub>Ti<sub>15</sub>/10TiO<sub>2</sub>, and Ni/Si<sub>85</sub>Ti<sub>15</sub>/5TiO<sub>2</sub> electrodes exhibit a less maximum amount of c-Li<sub>3.75</sub>Si and better capacity retention than that of the Ni/Si<sub>85</sub>Ti<sub>15</sub> electrode. This result indicates that the area of the c-Li<sub>3.75</sub>Si peak is not proportional to the capacity retention.

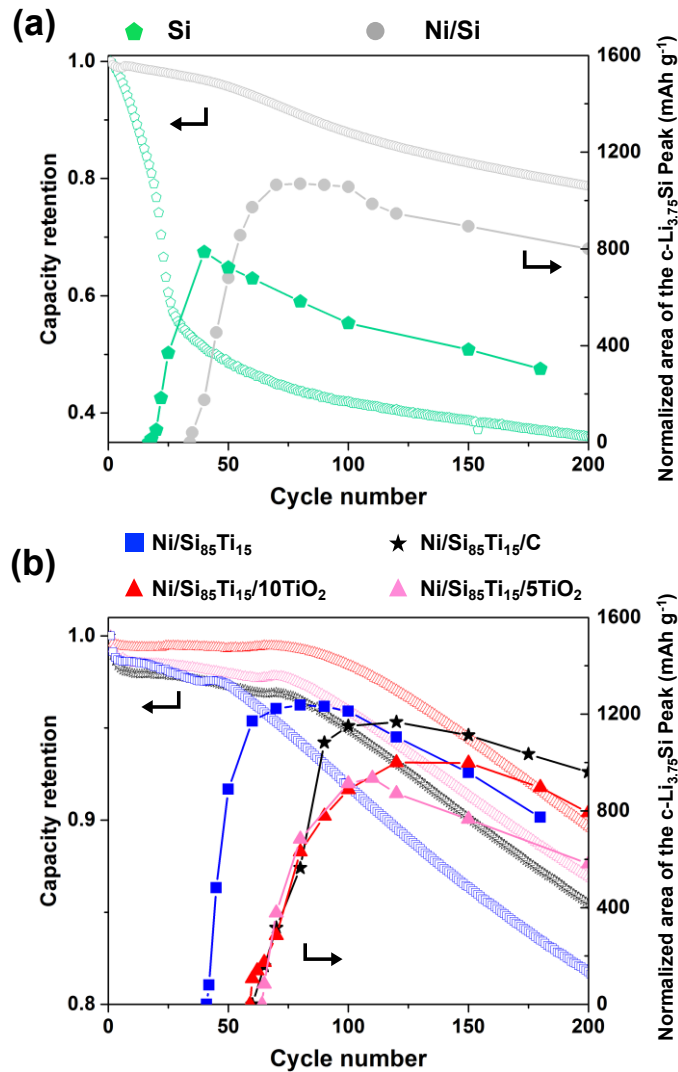


**Figure 4.9.** The normalized area of the Li<sub>3.75</sub>Si peak and capacity retention vs cycle number of Si, Ni/Si, Ni/Si<sub>85</sub>Ti<sub>15</sub>, Ni/Si<sub>85</sub>Ti<sub>15</sub>/C, Ni/Si<sub>85</sub>Ti<sub>15</sub>/10TiO<sub>2</sub>, and Ni/Si<sub>85</sub>Ti<sub>15</sub>/5TiO<sub>2</sub> electrodes.

According to the study by Iaboni et al., c-Li<sub>3.75</sub>Si will form in parts of the film that have delaminated and are thus no longer under the compressive stress exerted by the substrate but that have retained electrical contact with the rest of the film.<sup>179</sup> Both the substrate and the coating can induce a clamping effect, inhibiting c-Li<sub>3.75</sub>Si formation. According to the SEM pictures in Figure 4.3, the coating layers also lessen fragmentation of the film in the xy-plane. The trend in the maximum amount of c-Li<sub>3.75</sub>Si and capacity retention can now be understood as follows: The Si film on the Cu substrate has both poor adhesion and a high degree of fragmentation. The parts of the film that form c-Li<sub>3.75</sub>Si in any given cycle are also highly likely to completely disconnect from the rest of the film, keeping the total amount of c-Li<sub>3.75</sub>Si relatively low, at a maximum of ~800 mAh/g. The Ni adhesion layer increases clamping by the substrate as well as adhesion and thus delays the onset of Li<sub>3.75</sub>Si formation as well as improving the capacity retention. This allows more c-Li<sub>3.75</sub>Si to be formed in total, up to 1000 mAh/g. The Si<sub>85</sub>Ti<sub>15</sub> electrode starts to form c-Li<sub>3.75</sub>Si at approximately the same cycle as the Ni/Si electrode, indicating an equally large effect of clamping but showing less disintegration (see Figure 4.3). This further increases the maximum amount of c-Li<sub>3.75</sub>Si to ~1200 mAh/g. Compressive stress induced by the coatings further delays the onset of c-Li<sub>3.75</sub>Si formation relative to that of the Ni/Si<sub>85</sub>Ti<sub>15</sub> electrode for the C and TiO<sub>2</sub> coated electrodes. Moreover, the relatively less maximum amount of c-Li<sub>3.75</sub>Si for the C and TiO<sub>2</sub> coated films indicates that the coating material remains attached to parts of the film and keeps suppressing the formation of c-Li<sub>3.75</sub>Si during cycling, which leads to better integrity of the electrode, consistent with the SEM results.

To study the effect of the C and TiO<sub>2</sub> coating on SEI formation, the cumulative relative irreversible capacity attributed to the formation of SEI (RIC<sub>SEI</sub>) of all the samples was calculated using the same method described in previous work.<sup>82,196</sup> The cumulative RIC<sub>SEI</sub> is calculated as expressed below:

$$\sum \text{RIC}_{\text{SEI}} = \sum_{n=1}^N \frac{Q_{n+1}^{\text{Lith}} - Q_n^{\text{Delith}}}{Q_n^{\text{Delith}}}$$

where  $Q_{n+1}^{\text{Lith}}$  is the lithiation capacity at cycle  $n+1$ , and  $Q_n^{\text{Delith}}$  is the delithiation capacity at cycle  $n$ . The calculated results are shown in Figure 4.10a. The Ni/Si<sub>85</sub>Ti<sub>15</sub>

electrode shows the highest  $\text{RIC}_{\text{SEI}}$ , even higher than Si and Ni/Si electrodes, which may be because the addition of Ti increases the surface area of the electrode or the Ti catalyzes the decomposition of the electrolyte. The Ni/Si<sub>85</sub>Ti<sub>15</sub>/C, Ni/Si<sub>85</sub>Ti<sub>15</sub>/10TiO<sub>2</sub>, and Ni/Si<sub>85</sub>Ti<sub>15</sub>/5TiO<sub>2</sub> electrodes show relatively smaller  $\text{RIC}_{\text{SEI}}$  than the Ni/Si<sub>85</sub>Ti<sub>15</sub> electrode, indicating that the SEI grow slower on these samples.

The relative composition of SEI was analyzed by XPS and is shown in Figure 4.10b and Figure 4.11. The fitting model is self-consistent for all the samples examined, and the peak assignment is similar to some previous work.<sup>197–201</sup>

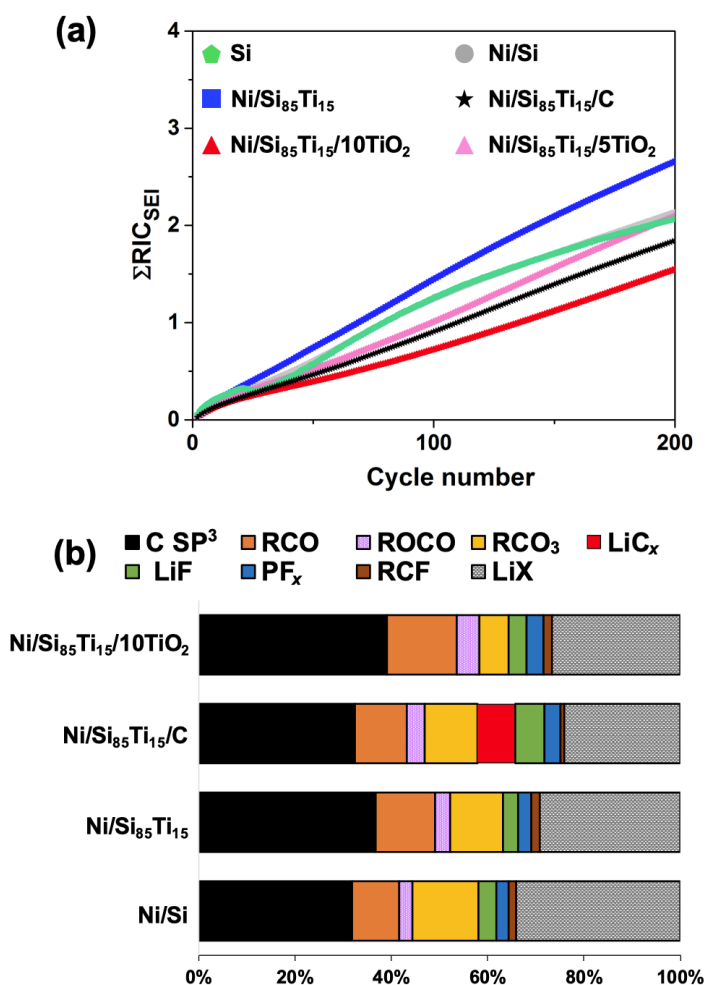


**Figure 4.10.** (a) Cumulative relative irreversible capacity due to the formation of SEI vs cycle number. (b) Relative composition of SEI in the outer 10 nm after 10 cycles of lithiation–delithiation. The results were calculated based on the XPS spectra of F 1s, C 1s, and Li 1s. All samples were tested under CCCV protocol.

The identified organic functionalities include aliphatic carbon (labelled as “C SP<sup>3</sup>”), alkoxy groups (“RCO”, contained in ethers and alkoxides), carboxyl groups and/or oxalates (“ROCO”, contained in carboxylates, esters, or oxalates), carbonates (“RCO<sub>3</sub>”, contained in carbonic esters and ionic carbonate salts), and organofluorines (“RCF”). Inorganic components include LiC<sub>x</sub> compounds (“LiC<sub>x</sub>”), lithium fluoride (“LiF”), and phosphoro-fluoride compounds (“PF<sub>x</sub>”, contained in Li<sub>x</sub>PF<sub>y</sub> and Li<sub>x</sub>PO<sub>y</sub>F<sub>z</sub>). The other components that cannot be distinguished in Li 1s, such as alkyl lithium, LiO, and Li<sub>2</sub>O, were labeled as “LiX”. As shown in Figures 4.10b and 4.11, only the Ni/Si<sub>85</sub>Ti<sub>15</sub>/C electrode shows a Li—C bond in C 1s, which is ascribed to the LiC<sub>x</sub> formed via lithiating amorphous carbon.<sup>202</sup> Besides, the Ni/Si<sub>85</sub>Ti<sub>15</sub>/C electrode shows a relatively higher concentration of LiF compared to the other three samples. A higher concentration LiF has been reported to promote rapid Li transport and may indicate more stable SEI.<sup>199,203</sup> The Ni/Si<sub>85</sub>Ti<sub>15</sub>/10TiO<sub>2</sub> electrode shows a relatively higher composition of aliphatic carbon, RCO, and ROCO, but lower RCO<sub>3</sub> compared with the other samples. Also, both the Ni/Si<sub>85</sub>Ti<sub>15</sub>/10TiO<sub>2</sub> and Ni/Si<sub>85</sub>Ti<sub>15</sub>/C electrodes show higher relative concentration of PF<sub>x</sub>, which suggests that LiPF<sub>6</sub> may prefer to decompose on the C and TiO<sub>2</sub> coated surface. The Ni/Si and Ni/Si<sub>85</sub>Ti<sub>15</sub> electrodes, on the other hand, show a more similar composition to each other except for the difference in aliphatic carbon and LiX. These results indicate that surface coatings influence the composition of SEI, possibly by making some components of the electrolyte decompose preferably.

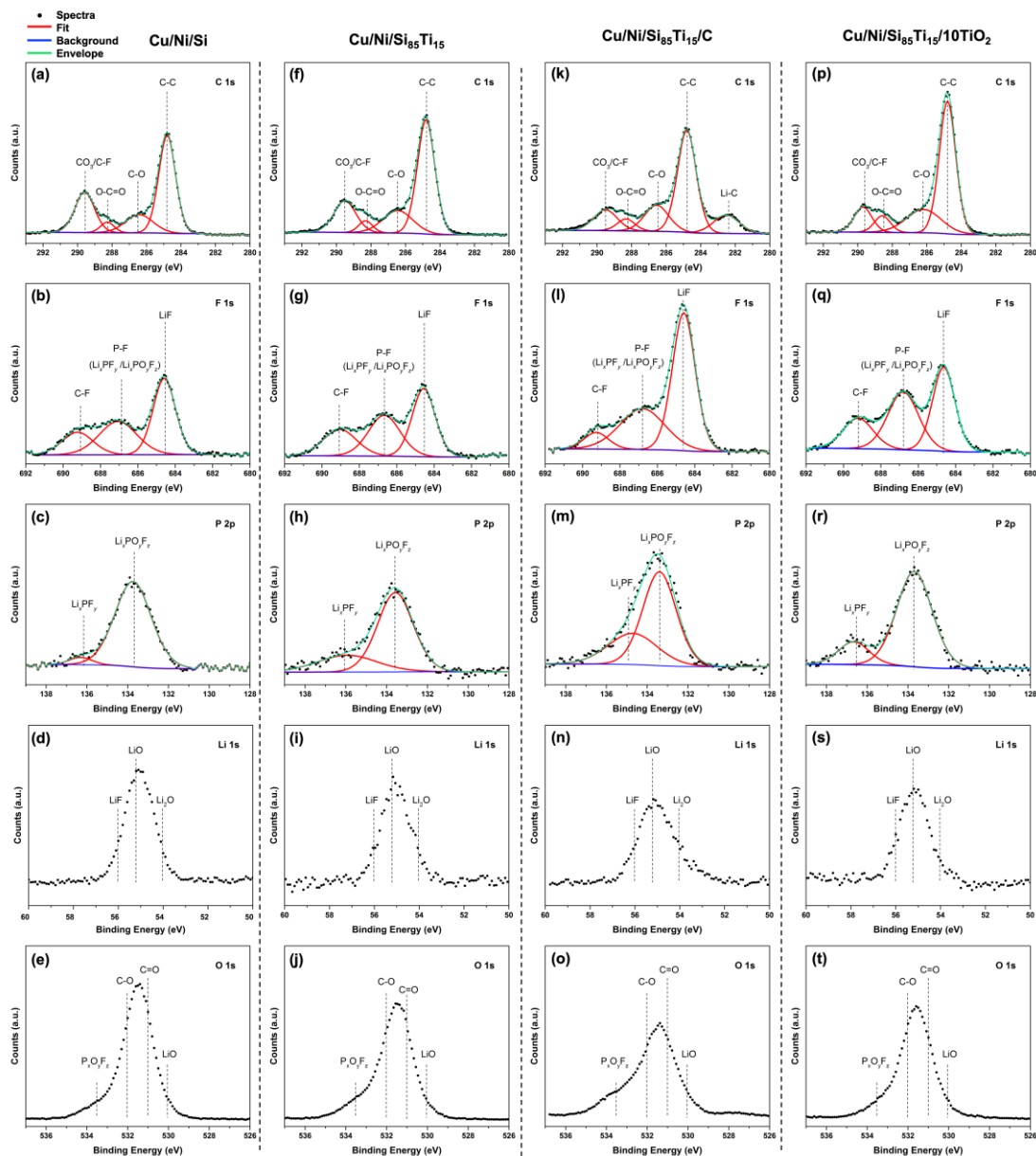


**Figure 4.11.** XPS spectra and Voigt function fits of the SEI composition, in the C 1s, F 1s, P 2p, Li 1s, and O 1s regions.

To further investigate the growth of SEI on different samples, in-operando neutron reflectometry (NR) analysis also was carried out. Neutrons are highly penetrating and non-destructive, which makes in-operando diagnostics of undisturbed SEI layers possible.<sup>204</sup> To conduct the in-operando NR experiment, an electrochemical cell was designed as shown in Figure 4.12. However, due to the unexpected large resistance of the cell, the prepared electrodes did not complete the lithiation–delithiation process

properly and the collected reflectivity profiles do not show an obvious difference at different times of the charge–discharge cycling test, as shown in Figure 4.13 and 4.14.

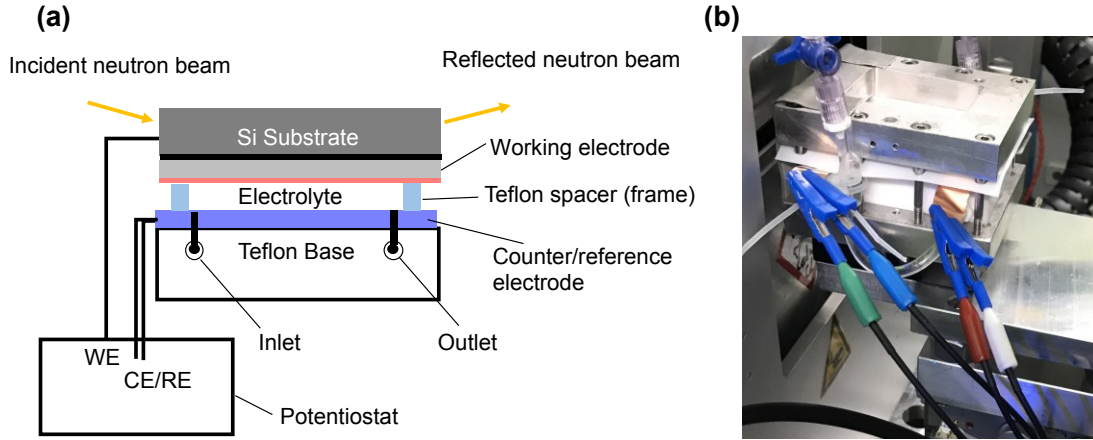


**Figure 4.12.** (a) Schematic sketch and (b) optical image of the in operando neutron reflectometry experimental setup.

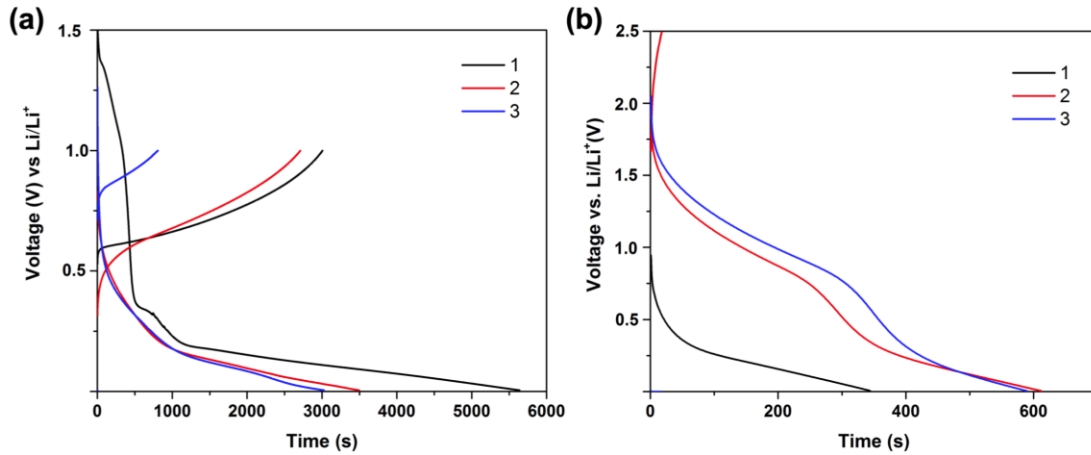


**Figure 4.13.** Voltage profiles of (a) Ni/Si<sub>85</sub>Ti<sub>15</sub> electrode tested at 0.4 C, and (b) Ni/Si<sub>85</sub>Ti<sub>15</sub>/10TiO<sub>2</sub> electrode tested at 0.1 C for the first three cycles. The samples were tested using the customized electrochemical cell, as shown in Figure 4.12.

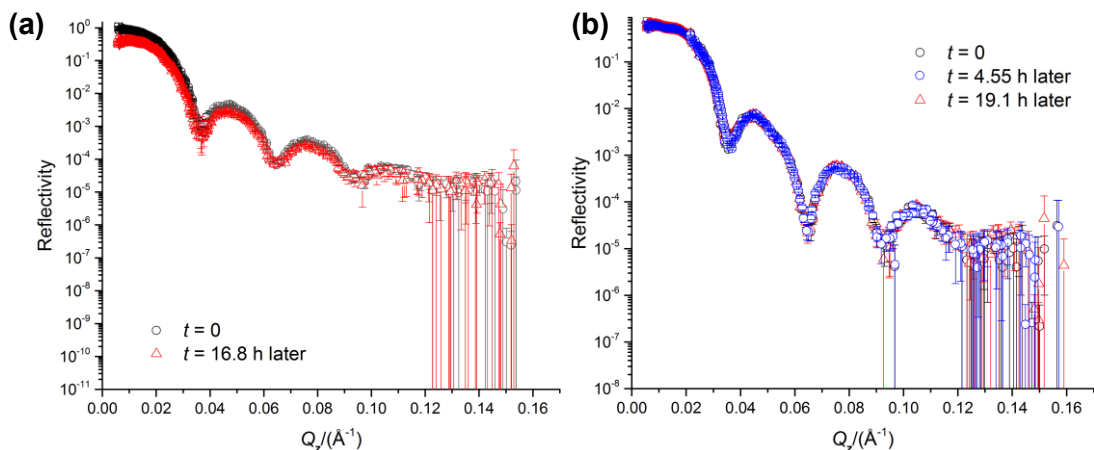


**Figure 4.14.** Neutron reflectivity vs  $Q$  for sample Ni/Si<sub>85</sub>Ti<sub>15</sub> and Ni/Si<sub>85</sub>Ti<sub>15</sub>/10TiO<sub>2</sub> electrodes at different times of cycling tests.

### 4.3 Conclusions

In this work, the adhesion layer and surface coatings were found to suppress the formation of c-Li<sub>3.75</sub>Si, resulting in improved capacity retentions and Coulombic efficiency. In addition, surface coatings were found to influence the growth rate and composition of SEI. Further research on different materials for the adhesion layers and surface coatings are interesting directions. Our results provide a further understanding of surfacing coating and adhesion layer on stabilization of Si-based anodes and can help guide the design of electrodes for advanced lithium-ion batteries.

## 4.4 Experimental Details

### 4.4.1 Materials and Equipment

Copper foil was obtained from McMaster Carr. CR2032 caps, stainless steel spacers, and springs were purchased from MTI Corporation. A 1.0 M lithium hexafluorophosphate (LiPF<sub>6</sub>) solution in ethylene carbonate and diethyl carbonate (EC/DEC=50/50 v/v%, battery-grade), fluoroethylene carbonate (FEC) (99%), diethyl carbonate (anhydrous, ≥99%), and metallic Li foil (99.9%) were purchased from Sigma-Aldrich. Trilayer polypropylene–polyethylene–polypropylene separators (2325) with a porosity of 39% were obtained from Celgard. Sputtering targets were

obtained from Plasmaterials, Inc., and the sputtering system used was an ATC Orion 8, AJA International Inc. The argon gas used for the sputtering system was of 5-N purity and was supplied by Praxair Canada Inc. A microbalance (XP6U) with an accuracy of 0.1  $\mu\text{g}$ , purchased from Mettler Toledo, was used to determine the weight of our samples. Electrochemical measurements were carried out with an Arbin BT2000 battery testing system.

#### 4.4.2 Electrode Preparation and Battery Assembly

Copper foils with a diameter of 15 mm were cleaned by sequential sonication in acetone and isopropanol for 10 min prior to using for sputtering. Six samples with different composition and nominal thicknesses, as shown in Scheme 4.1, were deposited on the Cu foils via sputtering at room temperature. The prepared electrodes are referred to as Si, Ni/Si, Ni/Si<sub>85</sub>Ti<sub>15</sub>, Ni/Si<sub>85</sub>Ti<sub>15</sub>/C, Ni/Si<sub>85</sub>Ti<sub>15</sub>/10TiO<sub>2</sub>, Ni/Si<sub>85</sub>Ti<sub>15</sub>/5TiO<sub>2</sub>. The Si<sub>85</sub>Ti<sub>15</sub> denotes the film that has a nominal molar ratio of 85% silicon and 15% titanium and the 10TiO<sub>2</sub> and 5TiO<sub>2</sub> refer to coating thicknesses of 10 and 5 nm, respectively. For carbon coating, a thickness of 10 nm is used in this study. Nickel and carbon were deposited with radio-frequency magnetron sputtering, while silicon (n-type) and titanium deposition were performed via DC-magnetron sputtering. The sputtering was carried out under argon gas at 5 mTorr with continuous substrate rotation. Si<sub>85</sub>Ti<sub>15</sub> was prepared by co-sputtering silicon and titanium, while titanium dioxide deposition was performed by reactive sputtering of titanium and oxygen under a mixture of argon and oxygen (9:1 v/v%).<sup>205-207</sup> The sputtering rates for Ni, Si, Ti, and C are 0.0172, 0.0410, 0.0064, and 0.0069 nm/s respectively. The sputtered films were weighed with a microbalance and then transferred to an argon-filled glove box. The CR2032-type coin cells were assembled using lithium foils as the counter electrode within the argon-filled glove box with moisture and oxygen levels  $\leq 0.2$  ppm. The electrolyte used is 1.0 M LiPF<sub>6</sub> solution in EC/DEC (50:50 v/v%), mixed with FEC (10% by volume).

### 4.4.3 Electrochemical Testing

Galvanostatic charge–discharge tests were performed at a C rate of 0.4 C and in the voltage range of 5 mV–1.0 V vs Li/Li<sup>+</sup>. The c-rate is calculated based on the theoretical specific capacity of each sample prepared in this work, as shown in Table 4.1. The further two constant voltage (CV) steps were carried out at the end of the constant current (CC) steps for lithiation and delithiation( i.e., at 5 mV/1.0 V vs Li/Li<sup>+</sup>) with a current limit of 0.01 C. All coin cells were tested in a temperature controlled chamber at 25.0±0.1 °C. Gravimetric capacity was calculated using the total weight of each film except the Ni layer. Capacity retention was calculated with respect to the highest delithiation capacity exhibited in each sample.

**Table 4.1.** Theoretical Specific Capacity of Each Sample Prepared in This Work.

Sample	Theoretical specific capacity (mAh/g) <sup>a,b</sup>
Si and Ni/Si	3579
Ni/Si <sub>85</sub> Ti <sub>15</sub>	2751
Ni/Si <sub>85</sub> Ti <sub>15</sub> /C	2691
Ni/Si <sub>85</sub> Ti <sub>15</sub> /10TiO <sub>2</sub>	2431
Ni/Si <sub>85</sub> Ti <sub>15</sub> /5TiO <sub>2</sub>	2580

- The mass of the Ni layer was not taken into account.
- The theoretical capacity of sputtered carbon and TiO<sub>2</sub> used for calculation are 1116 mAh/g (assuming each C atom can consume 0.5 Li atom)<sup>185,208</sup> and 335 mAh/g,<sup>209</sup> respectively.

### 4.4.4 Characterization

X-ray diffraction (XRD) analysis was carried out using an AXS diffractometer (Discover 8, Bruker, Madison, WI) equipped with a Histar general-area two-dimensional detection system (GADDs) and using Cu-K $\alpha$  radiation (= 1.5406 Å) at an incident angle of 15 degrees. X-ray photoelectron spectroscopy (XPS) analysis was carried out with an ULTRA (Kratos Analytical) spectrometer with

monochromatic Al K $\alpha$  radiation ( $h\nu = 1486.6$  eV) and under ultrahigh vacuum ( $10^{-9}$  Torr). The samples for XPS analysis were tested for 10 charge–discharge cycles first and immediately disassembled in the argon-filled glove box. The disassembled electrodes were rinsed with DEC five times to remove the residual electrolyte and dried in the glove box. An airtight container designed for transporting air-sensitive samples was used to transfer the electrodes from the glove box to the ultrahigh vacuum chamber for XPS measurements. The XPS results were analyzed using CasaXPS software. Scanning electron microscopy (SEM) analysis was performed with a Hitachi S-4800 field emission SEM at 15 kV and 20  $\mu$ A.

#### **4.4.5 In-operando Neutron Reflectometry Experiment**

To conduct the in-operando NR experiment, a compatible electrochemical cell was designed, as shown in Figure 4.12. Two Si<sub>85</sub>Ti<sub>15</sub> alloy electrodes with 10-nm surface coatings of carbon and TiO<sub>2</sub> and one without a surface coating were prepared via dc-magnetron sputtering on 8-mm thick Si substrates and used as the working electrode (WE). Li foil was used as the counter and reference electrode. The electrolyte used is a mixture of 1.0 M LiPF<sub>6</sub> in ethylene carbonate/diethyl carbonate (1:1 v/v) and a fluoroethylene carbonate additive (9:1 v/v). NR measurements were carried out while the cell is operating (in operando). The NR measurements were done at the REFSANS instrument using a sample-detector distance of 10370 mm, a neutron wavelength band of 0.3 to 2 nm, and a wavelength resolution of 4%, to enable a time resolution of 300 s in the in-operando measurements.

# Chapter 5

## Thesis Summary and Outlook

### 5.1 Summary

This thesis sought to develop high capacity alloying anodes, including Sn, Sb, and Si based materials, and to understand their reaction and/or degradation mechanisms for advanced lithium-ion and sodium-ion batteries. High capacity alloying anodes are of great interest to enable the next leap of energy storage technologies. In this final chapter, summaries of each preceding chapter and future research directions are provided in the following sections.

#### 5.1.1 Chapter 1

In Chapter 1, the background of lithium-ion and sodium-ion batteries were introduced, and the research development of several high capacity alloying anodes related to the work in this thesis were reviewed. Advanced lithium-ion and sodium-ion batteries with high energy density and long-term stability are required for both stationary and mobile applications, including electric vehicles and microgrid and grid-level energy storage. The development of high-performance lithium-ion and sodium-ion batteries significantly relies on improving the electrode materials. To evaluate the electrode materials, several important criteria, including capacity, voltage, power, Coulombic efficiency, and cycle life, were introduced. Next, the advantages, challenges, and research development of high capacity alloying anodes, with emphasis on Sn and Sb based materials for sodium-ion batteries, were reviewed. In addition, the pro and cons and research history of Si based anode materials, which is the most promising anode material for next-generation lithium-ion batteries, were discussed.

#### 5.1.2 Chapter 2

Chapter 2 presented a study of the ternary Sn–Bi–Sb system, in which all components are active towards Na. It was found that the addition of the alloying elements effectively enhanced the cycling stability of the pure elemental anodes, while

maintaining high specific capacities. The best performing alloy, Sn<sub>10</sub>Bi<sub>10</sub>Sb<sub>80</sub> (composed of 10 at% Sn, 10 at% Bi, and 80 at% Sb), is especially interesting because of its outstanding cycling stability as well as its single-phase as-deposited microstructure. By alloying with only 10% Sn and Bi, the cycling stability of elemental Sb improved significantly. The excellent cycling stability of the Sn<sub>10</sub>Bi<sub>10</sub>Sb<sub>80</sub> electrode was attributed to two reasons. Firstly, the dissolution of tin and bismuth atoms in the antimony lattice led to improved resistance toward the internal stress accompanied by the sodiation/desodiation. Secondly, alloying with Sn and Bi modified the chemical potential of Sb, leading to multiple sodiation processes. Each process has a relatively smaller volume expansion than that of elemental Sb, resulting in smaller internal stress for the electrode. The results in this study could guide the design and formulation of high capacity anode materials for sodium-ion batteries in bulk form.

### 5.1.3 Chapter 3

Chapter 3 investigated the sodiation–desodiation mechanism of a promising anode material, intermetallic  $\beta$ -SnSb, for sodium-ion batteries. Per in-situ TEM, ex-situ XRD, and electrochemical analysis, the reaction mechanism of  $\beta$ -SnSb with Na was revealed as below:

Sodiation ( $\beta$ -SnSb decomposes):



Desodiation ( $\beta$ -SnSb re-forms):



where the label “c-” represents a crystalline phase, while “a-” denotes an amorphous phase. Upon sodiation,  $\beta$ -SnSb decomposes and forms a crystalline c-Na<sub>3</sub>Sb and amorphous a-Na<sub>x</sub>Sn<sub>y</sub>. Further sodiation results in the formation of c-Na<sub>15</sub>Sn<sub>4</sub>. During desodiation, crystalline Sn was observed first, followed by the re-formation of  $\beta$ -SnSb. Moreover, a portion of Sn was found to segregate in extensively cycled specimens, which may account for the ultimate capacity degradation of  $\beta$ -SnSb.

### **5.1.4 Chapter 4**

Chapter 4 describes a study of the Ni adhesion layer and C/TiO<sub>2</sub> surface coating on suppression of both the formation of the c-Li<sub>3.75</sub>Si phase and solid electrolyte interphase in the Si-based anode for lithium-ion batteries. By incorporating the Ni adhesion layer and C/TiO<sub>2</sub> surface coating, the formation of c-Li<sub>3.75</sub>Si in the Si-based electrode was suppressed significantly and less fragmentation of the electrode was observed, resulting in improved cycling stability and Coulombic efficiency. Moreover, the C/TiO<sub>2</sub> surface coating was found to slow down the growth of the solid electrolyte interphase and influence its composition. These results provide a fundamental understanding of adhesion layers and surface coatings on the formation of the solid electrolyte interphase and stabilization of Si-based anodes for lithium-ion batteries.

## **5.2 Proposed Research Directions**

### **5.2.1 In-situ TEM Study of the Sn<sub>10</sub>Bi<sub>10</sub>Sb<sub>80</sub> Alloy Electrode**

As discussed in Chapter 2, by substitutional dissolution of only 10 at% Sn and Bi in Sb, the Sn<sub>10</sub>Bi<sub>10</sub>Sb<sub>80</sub> alloy electrode shows a significant improvement in terms of cycling stability and Coulombic efficiency compared to the pure Sb electrode. An in-situ TEM study of the pure Sb electrode shows that the sodiation process of Sb is spatially nonuniform, leading to high internal stress that can result in buckling and localized disconnection of the Sb film from its support, as shown in Figure 5.1.<sup>175</sup> This phenomenon is believed to be the main cause of the capacity degradation of the Sb electrode. As such, the increased number of sodiation processes observed in the Sn<sub>10</sub>Bi<sub>10</sub>Sb<sub>80</sub> alloy electrode may lead to more a homogeneous sodiation process and improved structural integrity of the electrode. Investigating the sodiation/desodiation process and microstructural change of the Sn<sub>10</sub>Bi<sub>10</sub>Sb<sub>80</sub> alloy electrode via in situ TEM analysis will help to elucidate the underlying mechanism of its improvement in electrochemical performance and guide the design of alloy anodes for rechargeable batteries.

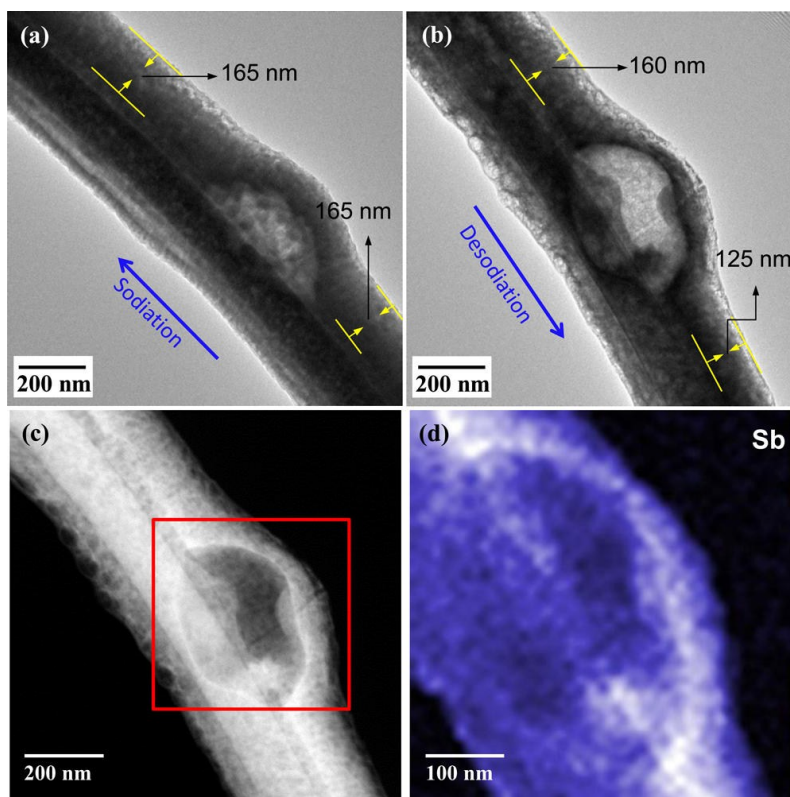
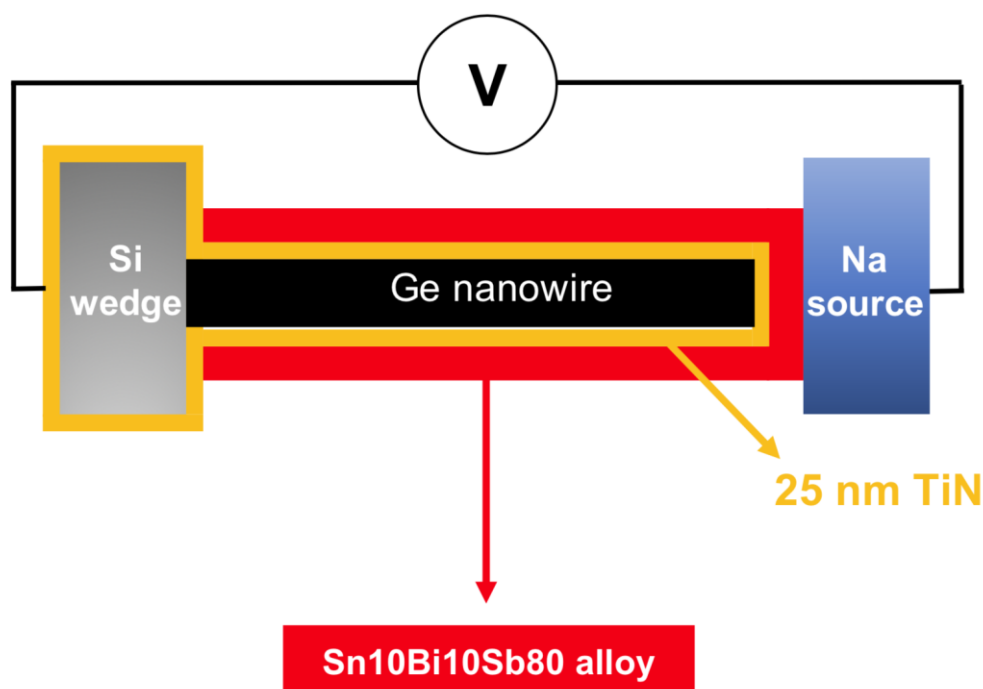


**Figure 5.1.** In situ TEM analysis of a 100-nm Sb film deposited on the TiN coated Ge nanowires. (a) BF-TEM micrograph of the film in the fully sodiated state after around 10 h and (b) in the desodiated state. Corresponding high-angle annular dark-field (HAADF) micrographs (c) and energy-dispersive X-ray spectroscopy (EDX) mapping of Sb (d) in the desodiated state. Reproduced with permission from reference 175 (Copyright 2015 American Chemical Society).

Moreover, a platform for conducting the in situ TEM experiment for alloys has been developed, as shown in Scheme 5.1, and successfully applied in our previous work.<sup>60,175</sup> The platform consists of three parts: the TiN coated Ge nanowires that grew on the Si wedge serve as an electrical conductive but Na inactive support; an alloy thin film that is deposited on the support via magnetron sputtering; and a small piece of pure Na that is used as the counter electrode. It is worth mentioning that the alloy film should not be too thick, otherwise the electrons cannot get through to obtain a clear TEM micrograph. A recommended thickness of the alloy is around 50 nm.



**Scheme 5.1.** Scheme illustration of the configuration of the platform for in-situ TEM experiments.

In addition, it would be meaningful to study the electrochemical performance of the Sn<sub>20</sub>Sb<sub>80</sub> and Bi<sub>20</sub>Sb<sub>80</sub> binary alloy electrodes; this will help to determine the roles of Bi and Sn in the improvement of the Sn<sub>10</sub>Bi<sub>10</sub>Sb<sub>80</sub> alloy electrode.

### 5.2.2 Exploration of Ternary and Quaternary Alloys for Sodium-ion Batteries

Alloying is an effective approach to improve the cycling stability of high capacity anode materials for sodium-ion batteries. As demonstrated in Chapter 2, ternary alloys show promising electrochemical performance as anodes for sodium-ion batteries. However, ternary alloys have been investigated less than binary alloys as anodes for sodium-ion batteries. Compared to binary systems, the ternary or quaternary systems offer more possibilities for optimization of the electrodes; a judicious choice of each component of these systems may lead to a synergistic effect on the electrochemical performance of the electrodes. Further investigation of high capacity element-based (e.g., Sn) ternary and quaternary alloys as anodes for sodium-ion batteries are of great interest.

### 5.2.3 The Maximum Length Scale of the Separation Between Sn and Sb to Enable the Formation of $\beta$ -SnSb

In Chapter 2, the Sn/Sb bilayers electrodes, regardless of the sequence of the layer, also exhibited the same degree of improvement in term of cycling stability and Coulombic efficiency as the  $\beta$ -SnSb electrode, compared to the pure Sn and Sb electrodes. The XRD analysis and voltage profiles of the bilayers and  $\beta$ -SnSb electrodes suggest that Sn and Sb progressively form  $\beta$ -SnSb during sodiation/desodiation, which was believed to account for their improvement. Building on these results, our recent work further investigated the mechanism of the improved cycling performance in Sn–Sb composites.<sup>210</sup> The results of this work clearly show a strong correlation between the amount of the  $\beta$ -SnSb formed and the capacity retention of the electrode, as shown in Figure 5.2. Moreover, this study indicates that Sn and Sb in the Sn–Sb composite need to be contacted intimately before the charge/discharge cycling test to form the  $\beta$ -SnSb phase; this is necessary for achieving good cycling stability. On the basis of these results, an interesting direction for future work is to study the maximum length scale of separation between Sn and Sb to enable the formation of intermetallic  $\beta$ -SnSb.

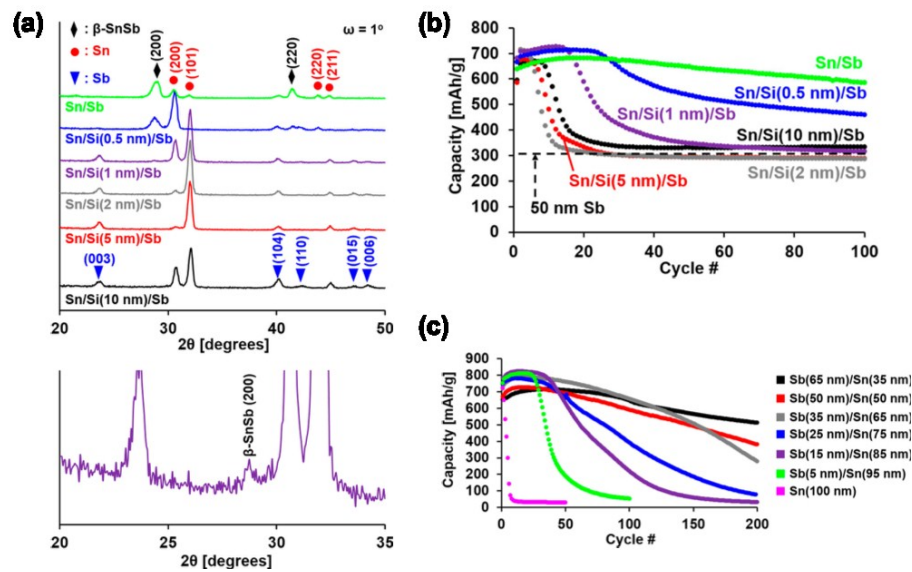
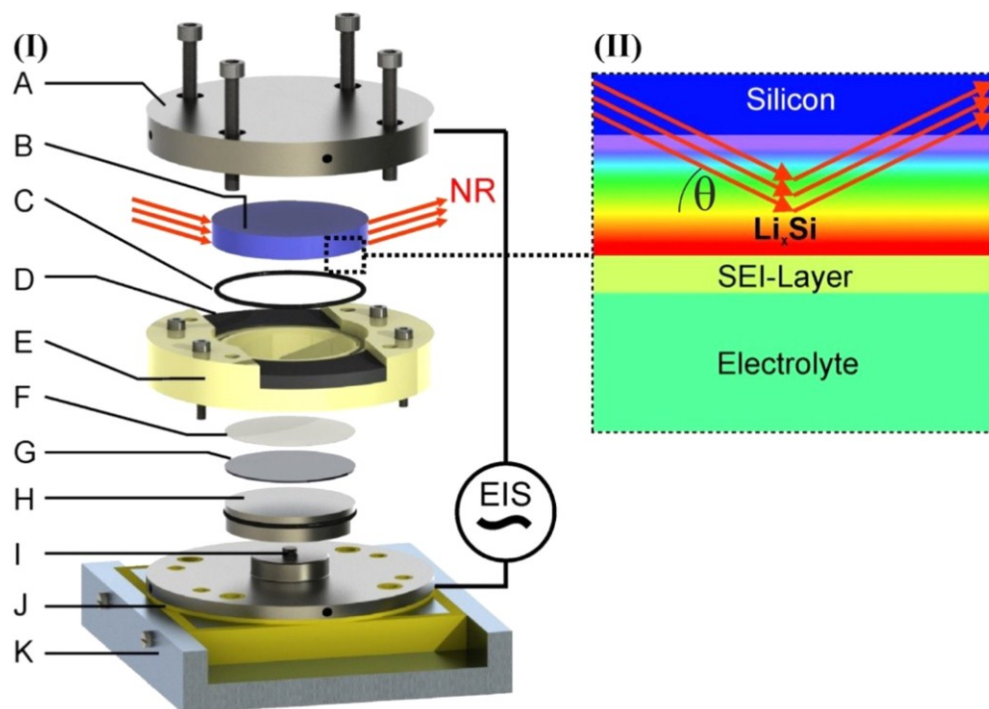


**Figure 5.2.** (a) Indexed XRD pattern of as-desodiated Sn/Si/Sb trilayer films. Specific capacity vs cycle number of (b) Sn/Si/Sb trilayer films and (c) Sb/Sn bilayer films. Reproduced and adapted with permission from reference 210 (Copyright 2019 American Chemical Society).

#### **5.2.4 Investigation of the Formation of Solid Electrolyte Interphase via In-operando Neutron Reflectometry**

It has been recognized widely that the solid electrolyte interphase (SEI), which is a passivation layer on the interface between electrode and electrolyte, plays an important role in battery performance, including cycle life, irreversible charge “loss”, and rate capability. Therefore, understanding the actual nature and formation process of the SEI is essential. However, due to its complicated composition and formation process, quantitative analysis of the formation process of SEI is still a difficult task. Neutron reflectometry (NR) is ideal for studying the SEI formation as it is sensitive to light elements, which are components of the SEI, with Ångström resolution. Moreover, neutrons are non-destructive and highly penetrating, enabling in-operando diagnostics of undisturbed SEI formed on electrodes. In Chapter 4, in-operando NR analysis of the SEI formation on a series of Si-based electrodes was conducted in an effort to investigate the effect of different surface coatings on the SEI formation. However, due to the high internal resistance of the cell, the electrodes were not lithiated fully during the in-operando NR experiment. Further development of the operando cell is required. Recently, Arne et al. reported an improved design for an electrochemical cell for conducting in-operando NR experiment that enables quantitative analysis of the SEI layer, as shown in Scheme 5.2.<sup>211</sup> A similar design of the cell can be used for and in-operando study of the roles of different surface coatings on an electrode and additives in the electrolyte on the formation of SEI. It is worth mentioning that a simulation of the theoretical neutron reflectivity profile prior to the in-operando NR analysis is essential to guiding the design of the working electrode and the experiment plan.



**Scheme 5.2.** Scheme illustration of the (a) configuration of the operando cell and (b) working electrode during neutron measurement. Reproduced and adapted with permission from reference 211 (Copyright 2018 Elsevier B.V.).

## References

- (1) World Energy Balances 2018 <https://webstore.iea.org/world-energy-balances-2018> (accessed Jun 23, 2019).
- (2) CO2 Emissions from Fuel Combustion 2018 <https://webstore.iea.org/co2-emissions-from-fuel-combustion-2018> (accessed Jun 23, 2019).
- (3) Pleßmann, G.; Erdmann, M.; Hlusiak, M.; Breyer, C. Global Energy Storage Demand for a 100% Renewable Electricity Supply. *Energy Procedia* **2014**, *46*, 22–31.
- (4) International Energy Agency. *Global EV Outlook 2019: Scaling-up the Transition to Electric Mobility*; OECD, 2019.
- (5) Dunn, B.; Kamath, H.; Tarascon, J.-M. Electrical Energy Storage for the Grid: A Battery of Choices. *Science* **2011**, *334* (6058), 928–935.
- (6) Hornsdale Power Reserve <https://hornsdailepowerreserve.com.au/> (accessed Jun 22, 2019).
- (7) Grosjean, C.; Miranda, P. H.; Perrin, M.; Poggi, P. Assessment of World Lithium Resources and Consequences of Their Geographic Distribution on the Expected Development of the Electric Vehicle Industry. *Renewable and Sustainable Energy Reviews* **2012**, *16* (3), 1735–1744.
- (8) Gruber, P. W.; Medina, P. A.; Keoleian, G. A.; Kesler, S. E.; Everson, M. P.; Wallington, T. J. Global Lithium Availability. *J. Ind. Ecol.* **2011**, *15* (5), 760–775.
- (9) Vaalma, C.; Buchholz, D.; Weil, M.; Passerini, S. A Cost and Resource Analysis of Sodium-Ion Batteries. *Nat. Rev. Mater.* **2018**, *3* (4), 18013.
- (10) Yabuuchi, N.; Kubota, K.; Dahbi, M.; Komaba, S. Research Development on Sodium-Ion Batteries. *Chem. Rev.* **2014**, *114* (23), 11636–11682.
- (11) Hwang, J.-Y.; S. Yoon, C.; Belharouak, I.; Sun, Y.-K. A Comprehensive Study of the Role of Transition Metals in O3-Type Layered Na[Ni<sub>x</sub>Co<sub>y</sub>Mn<sub>z</sub>]O<sub>2</sub> (x = 1/3, 0.5, 0.6, and 0.8) Cathodes for Sodium-Ion Batteries. *J. Mater. Chem. A* **2016**, *4* (46), 17952–17959.
- (12) Kubota, K.; Asari, T.; Yoshida, H.; Yaabuuchi, N.; Shiiba, H.; Nakayama, M.; Komaba, S. Understanding the Structural Evolution and Redox Mechanism of a NaFeO<sub>2</sub>–NaCoO<sub>2</sub> Solid Solution for Sodium-Ion Batteries. *Advanced Functional Materials* **2016**, *26* (33), 6047–6059.
- (13) de la Llave, E.; Talaie, E.; Levi, E.; Nayak, P. K.; Dixit, M.; Rao, P. T.; Hartmann, P.; Chesneau, F.; Major, D. T.; Greenstein, M.; et al. Improving Energy Density and Structural Stability of Manganese Oxide Cathodes for Na-Ion Batteries by Structural Lithium Substitution. *Chem. Mater.* **2016**, *28* (24), 9064–9076.
- (14) Zheng, Q.; Liu, W.; Li, X.; Zhang, H.; Feng, K.; Zhang, H. Facile Construction of Nanoscale Laminated Na<sub>3</sub>V<sub>2</sub>(PO<sub>4</sub>)<sub>3</sub> for a High-Performance Sodium Ion Battery Cathode. *J. Mater. Chem. A* **2016**, *4* (48), 19170–19178.
- (15) Ge, P.; Foulletier, M. Electrochemical Intercalation of Sodium in Graphite. *Solid State Ionics* **1988**, *28* (Part 2), 1172–1175.
- (16) Wan, J.; Shen, F.; Luo, W.; Zhou, L.; Dai, J.; Han, X.; Bao, W.; Xu, Y.; Panagiotopoulos, J.; Fan, X.; et al. In Situ Transmission Electron Microscopy Observation of Sodiation–Desodiation in a Long Cycle, High-Capacity Reduced Graphene Oxide Sodium-Ion Battery Anode. *Chem. Mater.* **2016**, *28* (18), 6528–6535.
- (17) Lotfabad, E. M.; Ding, J.; Cui, K.; Kohandehghan, A.; Kalisvaart, W. P.; Hazelton, M.; Mitlin, D. High-Density Sodium and Lithium Ion Battery Anodes from Banana Peels. *ACS Nano* **2014**, *8* (7), 7115–7129.
- (18) Li, Z.; Ma, L.; Surta, T. W.; Bommier, C.; Jian, Z.; Xing, Z.; Stickle, W. F.; Dolgos, M.; Amine, K.; Lu, J.; et al. High Capacity of Hard Carbon Anode in Na-Ion Batteries Unlocked by POx Doping. *ACS Energy Lett.* **2016**, *1* (2), 395–401.
- (19) Xie, H.; Kalisvaart, W. P.; Olsen, B. C.; Luber, E. J.; Mitlin, D.; Buriak, J. M. Sn–Bi–Sb Alloys as Anode Materials for Sodium Ion Batteries. *J. Mater. Chem. A* **2017**, *5* (20), 9661–9670.
- (20) Wang, J. W.; Liu, X. H.; Mao, S. X.; Huang, J. Y. Microstructural Evolution of Tin Nanoparticles during In Situ Sodium Insertion and Extraction. *Nano Lett.* **2012**, *12* (11), 5897–5902.
- (21) Tan, H.; Chen, D.; Rui, X.; Yu, Y. Peering into Alloy Anodes for Sodium-Ion Batteries: Current Trends, Challenges, and Opportunities. *Adv. Funct. Mater.* **2019**, *29* (14), 1808745.

- (22) Lao, M.; Zhang, Y.; Luo, W.; Yan, Q.; Sun, W.; Dou, S. X. Alloy-Based Anode Materials toward Advanced Sodium-Ion Batteries. *Advanced Materials* **2017**, *29* (48), 1700622.
- (23) Wang, W.; Li, W.; Wang, S.; Miao, Z.; Kun Liu, H.; Chou, S. Structural Design of Anode Materials for Sodium-Ion Batteries. *J. Mater. Chem. A* **2018**, *6* (15), 6183–6205.
- (24) Cui, J.; Yao, S.; Kim, J.-K. Recent Progress in Rational Design of Anode Materials for High-Performance Na-Ion Batteries. *Energy Storage Materials* **2017**, *7*, 64–114.
- (25) Liu, Y.; Zhang, N.; Jiao, L.; Tao, Z.; Chen, J. Ultrasmall Sn Nanoparticles Embedded in Carbon as High-Performance Anode for Sodium-Ion Batteries. *Adv. Funct. Mater.* **2015**, *25* (2), 214–220.
- (26) Qian, J.; Chen, Y.; Wu, L.; Cao, Y.; Ai, X.; Yang, H. High Capacity Na-Storage and Superior Cyclability of Nanocomposite Sb/C Anode for Na-Ion Batteries. *Chem. Commun.* **2012**, *48* (56), 7070–7072.
- (27) He, M.; Kravchyk, K.; Walter, M.; Kovalenko, M. V. Monodisperse Antimony Nanocrystals for High-Rate Li-Ion and Na-Ion Battery Anodes: Nano versus Bulk. *Nano Lett.* **2014**, *14* (3), 1255–1262.
- (28) Liu, S.; Feng, J.; Bian, X.; Liu, J.; Xu, H. The Morphology-Controlled Synthesis of a Nanoporous-Antimony Anode for High-Performance Sodium-Ion Batteries. *Energy Environ. Sci.* **2016**, *9* (4), 1229–1236.
- (29) Yang, F.; Yu, F.; Zhang, Z.; Zhang, K.; Lai, Y.; Li, J. Bismuth Nanoparticles Embedded in Carbon Spheres as Anode Materials for Sodium/Lithium-Ion Batteries. *Chem. Eur. J.* **2016**, *22* (7), 2333–2338.
- (30) Walter, M.; Doswald, S.; Kovalenko, M. V. Inexpensive Colloidal SnSb Nanoalloys as Efficient Anode Materials for Lithium- and Sodium-Ion Batteries. *J. Mater. Chem. A* **2016**, *4* (18), 7053–7059.
- (31) He, M.; Walter, M.; Kravchyk, K. V.; Erni, R.; Widmer, R.; Kovalenko, M. V. Monodisperse SnSb Nanocrystals for Li-Ion and Na-Ion Battery Anodes: Synergy and Dissonance between Sn and Sb. *Nanoscale* **2014**, *7* (2), 455–459.
- (32) Liu, Y.; Xu, Y.; Zhu, Y.; Culver, J. N.; Lundgren, C. A.; Xu, K.; Wang, C. Tin-Coated Viral Nanoforests as Sodium-Ion Battery Anodes. *ACS Nano* **2013**, *7* (4), 3627–3634.
- (33) Han, X.; Liu, Y.; Jia, Z.; Chen, Y.-C.; Wan, J.; Weadock, N.; Gaskell, K. J.; Li, T.; Hu, L. Atomic-Layer-Deposition Oxide Nanogluue for Sodium Ion Batteries. *Nano Lett.* **2014**, *14* (1), 139–147.
- (34) Wang, N.; Bai, Z.; Qian, Y.; Yang, J. Double-Walled Sb@TiO<sub>2-x</sub> Nanotubes as a Superior High-Rate and Ultralong-Lifespan Anode Material for Na-Ion and Li-Ion Batteries. *Adv. Mater.* **2016**, *28* (21), 4126–4133.
- (35) Liu, Y.; Fang, X.; Ge, M.; Rong, J.; Shen, C.; Zhang, A.; Enaya, H. A.; Zhou, C. SnO<sub>2</sub> Coated Carbon Cloth with Surface Modification as Na-Ion Battery Anode. *Nano Energy* **2015**, *16*, 399–407.
- (36) Kim, Y.; Park, Y.; Choi, A.; Choi, N.-S.; Kim, J.; Lee, J.; Ryu, J. H.; Oh, S. M.; Lee, K. T. An Amorphous Red Phosphorus/Carbon Composite as a Promising Anode Material for Sodium Ion Batteries. *Adv. Mater.* **2013**, *25* (22), 3045–3049.
- (37) Li, W.-J.; Chou, S.-L.; Wang, J.-Z.; Liu, H.-K.; Dou, S.-X. Simply Mixed Commercial Red Phosphorus and Carbon Nanotube Composite with Exceptionally Reversible Sodium-Ion Storage. *Nano Lett.* **2013**, *13* (11), 5480–5484.
- (38) Zhao, X.; Vail, S. A.; Lu, Y.; Song, J.; Pan, W.; Evans, D. R.; Lee, J.-J. Antimony/Graphitic Carbon Composite Anode for High-Performance Sodium-Ion Batteries. *ACS Appl. Mater. Interfaces* **2016**, *8* (22), 13871–13878.
- (39) Hong, K.-S.; Nam, D.-H.; Lim, S.-J.; Sohn, D.; Kim, T.-H.; Kwon, H. Electrochemically Synthesized Sb/Sb<sub>2</sub>O<sub>3</sub> Composites as High-Capacity Anode Materials Utilizing a Reversible Conversion Reaction for Na-Ion Batteries. *ACS Appl. Mater. Interfaces* **2015**, *7* (31), 17264–17271.
- (40) Jangid, M. K.; Vemulapally, A.; Sonia, F. J.; Aslam, M.; Mukhopadhyay, A. Feasibility of Reversible Electrochemical Na-Storage and Cyclic Stability of Amorphous Silicon and Silicon-Graphene Film Electrodes. *J. Electrochem. Soc.* **2017**, *164* (12), A2559–A2565.

- (41) Zhu, H.; Jia, Z.; Chen, Y.; Weadock, N.; Wan, J.; Vaaland, O.; Han, X.; Li, T.; Hu, L. Tin Anode for Sodium-Ion Batteries Using Natural Wood Fiber as a Mechanical Buffer and Electrolyte Reservoir. *Nano Lett.* **2013**, *13* (7), 3093–3100.
- (42) Zhao, X. B.; Cao, G. S. A Study of Zn<sub>4</sub>Sb<sub>3</sub> as a Negative Electrode for Secondary Lithium Cells. *Electrochimica Acta* **2001**, *46* (6), 891–896.
- (43) Li, W.; Hu, C.; Zhou, M.; Tao, H.; Wang, K.; Cheng, S.; Jiang, K. Carbon-Coated Mo<sub>3</sub>Sb<sub>7</sub> Composite as Anode Material for Sodium Ion Batteries with Long Cycle Life. *Journal of Power Sources* **2016**, *307*, 173–180.
- (44) Baggetto, L.; Allcorn, E.; Manthiram, A.; Veith, G. M. Cu<sub>2</sub>Sb Thin Films as Anode for Na-Ion Batteries. *Electrochemistry Communications* **2013**, *27*, 168–171.
- (45) Jackson, E. D.; Green, S.; Prieto, A. L. Electrochemical Performance of Electrodeposited Zn<sub>4</sub>Sb<sub>3</sub> Films for Sodium-Ion Secondary Battery Anodes. *ACS Appl. Mater. Interfaces* **2015**, *7* (14), 7447–7450.
- (46) Wang, L.; Wang, C.; Zhang, N.; Li, F.; Cheng, F.; Chen, J. High Anode Performance of in Situ Formed Cu<sub>2</sub>Sb Nanoparticles Integrated on Cu Foil via Replacement Reaction for Sodium-Ion Batteries. *ACS Energy Lett.* **2017**, *2* (1), 256–262.
- (47) Darwiche, A.; Toiron, M.; Sougrati, M. T.; Fraisse, B.; Stievano, L.; Monconduit, L. Performance and Mechanism of FeSb<sub>2</sub> as Negative Electrode for Na-Ion Batteries. *Journal of Power Sources* **2015**, *280*, 588–592.
- (48) Lin, Y.-M.; Abel, P. R.; Gupta, A.; Goodenough, J. B.; Heller, A.; Mullins, C. B. Sn–Cu Nanocomposite Anodes for Rechargeable Sodium-Ion Batteries. *ACS Appl. Mater. Interfaces* **2013**, *5* (17), 8273–8277.
- (49) Farbod, B.; Cui, K.; Kalisvaart, W. P.; Kupsta, M.; Zahiri, B.; Kohandehghan, A.; Lotfabad, E. M.; Li, Z.; Luber, E. J.; Mitlin, D. Anodes for Sodium Ion Batteries Based on Tin–Germanium–Antimony Alloys. *ACS Nano* **2014**, *8* (5), 4415–4429.
- (50) Zhao, Y.; Manthiram, A. High-Capacity, High-Rate Bi–Sb Alloy Anodes for Lithium-Ion and Sodium-Ion Batteries. *Chem. Mater.* **2015**, *27* (8), 3096–3101.
- (51) Abel, P. R.; Fields, M. G.; Heller, A.; Mullins, C. B. Tin–Germanium Alloys as Anode Materials for Sodium-Ion Batteries. *ACS Appl. Mater. Interfaces* **2014**, *6* (18), 15860–15867.
- (52) Darwiche, A.; Sougrati, M. T.; Fraisse, B.; Stievano, L.; Monconduit, L. Facile Synthesis and Long Cycle Life of SnSb as Negative Electrode Material for Na-Ion Batteries. *Electrochemistry Communications* **2013**, *32*, 18–21.
- (53) Sony's New Nexelion Hybrid Lithium Ion Batteries to Have Thirty-percent More Capacity Than Conventional Offering <http://www.sony.net/SonyInfo/News/Press/200502/05-006E/index.html> (accessed Jun 22, 2019).
- (54) Panasonic Develops High-Capacity Lithium-Ion Battery Cells That Can Power Laptops and Electric Vehicles | Headquarters News | Panasonic Newsroom Global <https://news.panasonic.com/global/press/data/en091225-3/en091225-3.html> (accessed Jun 23, 2019).
- (55) Vogt, L. O.; Villevieille, C. FeSn<sub>2</sub> and CoSn<sub>2</sub> Electrode Materials for Na-Ion Batteries. *J. Electrochem. Soc.* **2016**, *163* (7), A1306–A1310.
- (56) Kreder, K. J.; Heligman, B. T.; Manthiram, A. Interdigitated Eutectic Alloy Foil Anodes for Rechargeable Batteries. *ACS Energy Lett.* **2017**, *2* (10), 2422–2423.
- (57) Baggetto, L.; Carroll, K. J.; Hah, H.-Y.; Johnson, C. E.; Mullins, D. R.; Unocic, R. R.; Johnson, J. A.; Meng, Y. S.; Veith, G. M. Probing the Mechanism of Sodium Ion Insertion into Copper Antimony Cu<sub>2</sub>Sb Anodes. *J. Phys. Chem. C* **2014**, *118* (15), 7856–7864.
- (58) Baggetto, L.; Hah, H.-Y.; Johnson, C. E.; Bridges, C. A.; Johnson, J. A.; Veith, G. M. The Reaction Mechanism of FeSb<sub>2</sub> as Anode for Sodium-Ion Batteries. *Phys. Chem. Chem. Phys.* **2014**, *16* (20), 9538–9545.
- (59) Xiao, L.; Cao, Y.; Xiao, J.; Wang, W.; Kovarik, L.; Nie, Z.; Liu, J. High Capacity, Reversible Alloying Reactions in SnSb/C Nanocomposites for Na-Ion Battery Applications. *Chem. Commun.* **2012**, *48* (27), 3321–3323.
- (60) Xie, H.; Tan, X.; Luber, E. J.; Olsen, B. C.; Kalisvaart, W. P.; Jungjohann, K. L.; Mitlin, D.; Buriak, J. M. β-SnSb for Sodium Ion Battery Anodes: Phase Transformations Responsible for Enhanced Cycling Stability Revealed by In Situ TEM. *ACS Energy Lett.* **2018**, *3* (7), 1670–1676.

- (61) Kalisvaart, W. P.; Olsen, B. C.; Lubner, E. J.; Buriak, J. M. Sb–Si Alloys and Multilayers for Sodium-Ion Battery Anodes. *ACS Appl. Energy Mater.* **2019**, *2* (3), 2205–2213.
- (62) *Alloy Phase Diagrams*; Okamoto, H., Schlesinger, M. E., Mueller, E. M., Eds.; ASM International, 2016.
- (63) Ellis, L. D.; Hatchard, T. D.; Obrovac, M. N. Reversible Insertion of Sodium in Tin. *J. Electrochem. Soc.* **2012**, *159* (11), A1801–A1805.
- (64) Stratford, J. M.; Mayo, M.; Allan, P. K.; Pecher, O.; Borkiewicz, O. J.; Wiaderek, K. M.; Chapman, K. W.; Pickard, C. J.; Morris, A. J.; Grey, C. P. Investigating Sodium Storage Mechanisms in Tin Anodes: A Combined Pair Distribution Function Analysis, Density Functional Theory, and Solid-State NMR Approach. *J. Am. Chem. Soc.* **2017**, *139* (21), 7273–7286.
- (65) Zhu, J.; Deng, D. Amorphous Bimetallic Co<sub>3</sub>Sn<sub>2</sub> Nanoalloys Are Better Than Crystalline Counterparts for Sodium Storage. *J. Phys. Chem. C* **2015**, *119* (37), 21323–21328.
- (66) Abel, P. R.; Fields, M. G.; Heller, A.; Mullins, C. B. Tin–Germanium Alloys as Anode Materials for Sodium-Ion Batteries. *ACS Appl. Mater. Interfaces* **2014**, *6* (18), 15860–15867.
- (67) Darwiche, A.; Marino, C.; Sougrati, M. T.; Fraisse, B.; Stievano, L.; Monconduit, L. Better Cycling Performances of Bulk Sb in Na-Ion Batteries Compared to Li-Ion Systems: An Unexpected Electrochemical Mechanism. *J. Am. Chem. Soc.* **2012**, *134* (51), 20805–20811.
- (68) Allan, P. K.; Griffin, J. M.; Darwiche, A.; Borkiewicz, O. J.; Wiaderek, K. M.; Chapman, K. W.; Morris, A. J.; Chupas, P. J.; Monconduit, L.; Grey, C. P. Tracking Sodium–Antimonide Phase Transformations in Sodium-Ion Anodes: Insights from Operando Pair Distribution Function Analysis and Solid-State NMR Spectroscopy. *J. Am. Chem. Soc.* **2016**, *138* (7), 2352–2365.
- (69) Nie, A.; Gan, L.; Cheng, Y.; Tao, X.; Yuan, Y.; Sharifi-Asl, S.; He, K.; Asayesh-Ardakani, H.; Vasiraju, V.; Lu, J.; et al. Ultrafast and Highly Reversible Sodium Storage in Zinc–Antimony Intermetallic Nanomaterials. *Adv. Funct. Mater.* **2016**, *26* (4), 543–552.
- (70) Gao, H.; Niu, J.; Zhang, C.; Peng, Z.; Zhang, Z. A Dealloying Synthetic Strategy for Nanoporous Bismuth–Antimony Anodes for Sodium Ion Batteries. *ACS Nano* **2018**, *12* (4), 3568–3577.
- (71) Baggetto, L.; Allcorn, E.; Unocic, R. R.; Manthiram, A.; Veith, G. M. Mo<sub>3</sub>Sb<sub>7</sub> as a Very Fast Anode Material for Lithium-Ion and Sodium-Ion Batteries. *J. Mater. Chem. A* **2013**, *1* (37), 11163–11169.
- (72) Baggetto, L.; Marszewski, M.; Górka, J.; Jaroniec, M.; Veith, G. M. AlSb Thin Films as Negative Electrodes for Li-Ion and Na-Ion Batteries. *Journal of Power Sources* **2013**, *243*, 699–705.
- (73) Blomgren, G. E. The Development and Future of Lithium Ion Batteries. *J. Electrochem. Soc.* **2017**, *164* (1), A5019–A5025.
- (74) C. Yao, K. P.; S. Okasinski, J.; Kalaga, K.; A. Shkrob, I.; P. Abraham, D. Quantifying Lithium Concentration Gradients in the Graphite Electrode of Li-Ion Cells Using Operando Energy Dispersive X-Ray Diffraction. *Energy Environ. Sci.* **2019**, *12* (2), 656–665.
- (75) Sharma, R. A.; Seefurth, R. N. Thermodynamic Properties of the Lithium–Silicon System. *J. Electrochem. Soc.* **1976**, *123* (12), 1763–1768.
- (76) Seefurth, R. N.; Sharma, R. A. Investigation of Lithium Utilization from a Lithium–Silicon Electrode. *J. Electrochem. Soc.* **1977**, *124* (8), 1207–1214.
- (77) Wen, C. J.; Huggins, R. A. Chemical Diffusion in Intermediate Phases in the Lithium–Silicon System. *Journal of Solid State Chemistry* **1981**, *37* (3), 271–278.
- (78) Beattie, S. D.; Larcher, D.; Morcrette, M.; Simon, B.; Tarascon, J.-M. Si Electrodes for Li-Ion Batteries—A New Way to Look at an Old Problem. *J. Electrochem. Soc.* **2008**, *155* (2), A158–A163.
- (79) Luo, F.; Liu, B.; Zheng, J.; Chu, G.; Zhong, K.; Li, H.; Huang, X.; Chen, L. Review—Nano-Silicon/Carbon Composite Anode Materials Towards Practical Application for Next Generation Li-Ion Batteries. *J. Electrochem. Soc.* **2015**, *162* (14), A2509–A2528.
- (80) Obrovac, M. N.; Krause, L. J. Reversible Cycling of Crystalline Silicon Powder. *J. Electrochem. Soc.* **2007**, *154* (2), A103–A108.
- (81) Ogata, K.; Salager, E.; Kerr, C. J.; Fraser, A. E.; Ducati, C.; Morris, A. J.; Hofmann, S.; Grey, C. P. Revealing Lithium–Silicide Phase Transformations in Nano-Structured Silicon-Based Lithium Ion Batteries via *in Situ* NMR Spectroscopy. *Nat. Commun.* **2014**, *5*, 3217.

- (82) Sayed, S. Y.; Kalisvaart, W. P.; Olsen, B. C.; Lubner, E. J.; Xie, H.; Buriak, J. M. Alternating Silicon and Carbon Multilayer-Structured Anodes Suppress Formation of the  $c\text{-Li}_{3.75}\text{Si}$  Phase. *Chem. Mater.* **2019**.
- (83) Choi, J. W.; Aurbach, D. Promise and Reality of Post-Lithium-Ion Batteries with High Energy Densities. *Nat. Rev. Mater.* **2016**, *1* (4), 16013.
- (84) Wu, H.; Cui, Y. Designing Nanostructured Si Anodes for High Energy Lithium Ion Batteries. *Nano Today* **2012**, *7* (5), 414–429.
- (85) Feng, K.; Li, M.; Liu, W.; Kashkooli, A. G.; Xiao, X.; Cai, M.; Chen, Z. Silicon-Based Anodes for Lithium-Ion Batteries: From Fundamentals to Practical Applications. *Small* **2018**, *14* (8), 1702737.
- (86) Zuo, X.; Zhu, J.; Müller-Buschbaum, P.; Cheng, Y.-J. Silicon Based Lithium-Ion Battery Anodes: A Chronicle Perspective Review. *Nano Energy* **2017**, *31*, 113–143.
- (87) Hyejung, K.; Minho, S.; Mi-Hee, P.; Jaephil, C. A Critical Size of Silicon Nano-Anodes for Lithium Rechargeable Batteries. *Angew. Chem. Int. Ed.* **49** (12), 2146–2149.
- (88) Liu, X. H.; Zhong, L.; Huang, S.; Mao, S. X.; Zhu, T.; Huang, J. Y. Size-Dependent Fracture of Silicon Nanoparticles During Lithiation. *ACS Nano* **2012**, *6* (2), 1522–1531.
- (89) Chockla, A. M.; Harris, J. T.; Akhavan, V. A.; Bogart, T. D.; Holmberg, V. C.; Steinhagen, C.; Mullins, C. B.; Stevenson, K. J.; Korgel, B. A. Silicon Nanowire Fabric as a Lithium Ion Battery Electrode Material. *J. Am. Chem. Soc.* **2011**, *133* (51), 20914–20921.
- (90) Nguyen, H. T.; Yao, F.; Zamfir, M. R.; Biswas, C.; So, K. P.; Lee, Y. H.; Kim, S. M.; Cha, S. N.; Kim, J. M.; Pribat, D. Highly Interconnected Si Nanowires for Improved Stability Li-Ion Battery Anodes. *Adv. Energy Mater.* **2011**, *1* (6), 1154–1161.
- (91) Park, M.-H.; Kim, M. G.; Joo, J.; Kim, K.; Kim, J.; Ahn, S.; Cui, Y.; Cho, J. Silicon Nanotube Battery Anodes. *Nano Lett.* **2009**, *9* (11), 3844–3847.
- (92) Wu, H.; Chan, G.; Choi, J. W.; Ryu, I.; Yao, Y.; McDowell, M. T.; Lee, S. W.; Jackson, A.; Yang, Y.; Hu, L.; et al. Stable Cycling of Double-Walled Silicon Nanotube Battery Anodes through Solid-Electrolyte Interphase Control. *Nat Nano* **2012**, *7* (5), 310–315.
- (93) Cui, L.-F.; Yang, Y.; Hsu, C.-M.; Cui, Y. Carbon–Silicon Core–Shell Nanowires as High Capacity Electrode for Lithium Ion Batteries. *Nano Lett.* **2009**, *9* (9), 3370–3374.
- (94) Cui, L.-F.; Ruffo, R.; Chan, C. K.; Peng, H.; Cui, Y. Crystalline-Amorphous Core–Shell Silicon Nanowires for High Capacity and High Current Battery Electrodes. *Nano Lett.* **2009**, *9* (1), 491–495.
- (95) Liu, N.; Wu, H.; McDowell, M. T.; Yao, Y.; Wang, C.; Cui, Y. A Yolk-Shell Design for Stabilized and Scalable Li-Ion Battery Alloy Anodes. *Nano Lett.* **2012**, *12* (6), 3315–3321.
- (96) Liu, N.; Lu, Z.; Zhao, J.; McDowell, M. T.; Lee, H.-W.; Zhao, W.; Cui, Y. A Pomegranate-Inspired Nanoscale Design for Large-Volume-Change Lithium Battery Anodes. *Nat Nano* **2014**, *9* (3), 187–192.
- (97) Hu, X.; Jin, Y.; Zhu, B.; Tan, Y.; Zhang, S.; Zong, L.; Lu, Z.; Zhu, J. Free-Standing Graphene-Encapsulated Silicon Nanoparticle Aerogel as an Anode for Lithium Ion Batteries. *ChemNanoMat* **2016**, *2* (7), 671–674.
- (98) Xu, B.; Wu, H.; Lin, C. X. (Cynthia); Wang, B.; Zhang, Z.; Zhao, X. S. Stabilization of Silicon Nanoparticles in Graphene Aerogel Framework for Lithium Ion Storage. *RSC Adv.* **2015**, *5* (39), 30624–30630.
- (99) Lu, Z.; Liu, N.; Lee, H.-W.; Zhao, J.; Li, W.; Li, Y.; Cui, Y. Nonfilling Carbon Coating of Porous Silicon Micrometer-Sized Particles for High-Performance Lithium Battery Anodes. *ACS Nano* **2015**, *9* (3), 2540–2547.
- (100) Aghajamali, M.; Xie, H.; Javadi, M.; Kalisvaart, W. P.; Buriak, J. M.; Veinot, J. G. C. Size and Surface Effects of Silicon Nanocrystals in Graphene Aerogel Composite Anodes for Lithium Ion Batteries. *Chem. Mater.* **2018**, *30* (21), 7782–7792.
- (101) NuLi, Y.; Wang, B.; Yang, J.; Yuan, X.; Ma, Z.  $\text{Cu}_5\text{Si-Si/C}$  Composites for Lithium-Ion Battery Anodes. *Journal of Power Sources* **2006**, *153* (2), 371–374.
- (102) Li, T.; Cao, Y. L.; Ai, X. P.; Yang, H. X. Cycleable Graphite/ $\text{FeSi}_6$  Alloy Composite as a High Capacity Anode Material for Li-Ion Batteries. *Journal of Power Sources* **2008**, *184* (2), 473–476.
- (103) Lee, H.-Y.; Kim, Y.-L.; Hong, M.-K.; Lee, S.-M. Carbon-Coated  $\text{Ni}_{20}\text{Si}_{80}$  Alloy–Graphite Composite as an Anode Material for Lithium-Ion Batteries. *Journal of Power Sources* **2005**, *141* (1), 159–162.

- (104) Park, M.-S.; Rajendran, S.; Kang, Y.-M.; Han, K.-S.; Han, Y.-S.; Lee, J.-Y. Si–Ni Alloy–Graphite Composite Synthesized by Arc-Melting and High-Energy Mechanical Milling for Use as an Anode in Lithium-Ion Batteries. *Journal of Power Sources* **2006**, *158* (1), 650–653.
- (105) Yan, J. M.; Huang, H. Z.; Zhang, J.; Yang, Y. The Study of Mg<sub>2</sub>Si/Carbon Composites as Anode Materials for Lithium Ion Batteries. *Journal of Power Sources* **2008**, *175* (1), 547–552.
- (106) Magasinski, A.; Zdyrko, B.; Kovalenko, I.; Hertzberg, B.; Burtovyy, R.; Huebner, C. F.; Fuller, T. F.; Luzinov, I.; Yushin, G. Toward Efficient Binders for Li-Ion Battery Si-Based Anodes: Polyacrylic Acid. *ACS Appl. Mater. Interfaces* **2010**, *2* (11), 3004–3010.
- (107) Wang, C.; Wu, H.; Chen, Z.; McDowell, M. T.; Cui, Y.; Bao, Z. Self-Healing Chemistry Enables the Stable Operation of Silicon Microparticle Anodes for High-Energy Lithium-Ion Batteries. *Nat Chem* **2013**, *5* (12), 1042–1048.
- (108) Erk, C.; Brezesinski, T.; Sommer, H.; Schneider, R.; Janek, J. Toward Silicon Anodes for Next-Generation Lithium Ion Batteries: A Comparative Performance Study of Various Polymer Binders and Silicon Nanopowders. *ACS Appl. Mater. Interfaces* **2013**, *5* (15), 7299–7307.
- (109) Hu, B.; Shkrob, I. A.; Zhang, S.; Zhang, L.; Zhang, J.; Li, Y.; Liao, C.; Zhang, Z.; Lu, W.; Zhang, L. The Existence of Optimal Molecular Weight for Poly(Acrylic Acid) Binders in Silicon/Graphite Composite Anode for Lithium-Ion Batteries. *Journal of Power Sources* **2018**, *378*, 671–676.
- (110) Mazouzi, D.; Karkar, Z.; Reale Hernandez, C.; Jimenez Manero, P.; Guyomard, D.; Roué, L.; Lestriez, B. Critical Roles of Binders and Formulation at Multiscales of Silicon-Based Composite Electrodes. *Journal of Power Sources* **2015**, *280*, 533–549.
- (111) Higgins, T. M.; Park, S.-H.; King, P. J.; Zhang, C. (John); McEvoy, N.; Berner, N. C.; Daly, D.; Shmeliov, A.; Khan, U.; Duesberg, G.; et al. A Commercial Conducting Polymer as Both Binder and Conductive Additive for Silicon Nanoparticle-Based Lithium-Ion Battery Negative Electrodes. *ACS Nano* **2016**, *10* (3), 3702–3713.
- (112) Ellis, L. D.; Wilkes, B. N.; Hatchard, T. D.; Obrovac, M. N. In Situ XRD Study of Silicon, Lead and Bismuth Negative Electrodes in Nonaqueous Sodium Cells. *J. Electrochem. Soc.* **2014**, *161* (3), A416–A421.
- (113) Abel, P. R.; Lin, Y.-M.; de Souza, T.; Chou, C.-Y.; Gupta, A.; Goodenough, J. B.; Hwang, G. S.; Heller, A.; Mullins, C. B. Nanocolumnar Germanium Thin Films as a High-Rate Sodium-Ion Battery Anode Material. *J. Phys. Chem. C* **2013**, *117* (37), 18885–18890.
- (114) Kohandehghan, A.; Cui, K.; Kupsta, M.; Ding, J.; Memarzadeh Lotfabad, E.; Kalisvaart, W. P.; Mitlin, D. Activation with Li Enables Facile Sodium Storage in Germanium. *Nano Lett.* **2014**, *14* (10), 5873–5882.
- (115) Darwiche, A.; Marino, C.; Sougrati, M. T.; Fraisse, B.; Stievano, L.; Monconduit, L. Better Cycling Performances of Bulk Sb in Na-Ion Batteries Compared to Li-Ion Systems: An Unexpected Electrochemical Mechanism. *J. Am. Chem. Soc.* **2012**, *134* (51), 20805–20811.
- (116) He, M.; Kravchyk, K.; Walter, M.; Kovalenko, M. V. Monodisperse Antimony Nanocrystals for High-Rate Li-Ion and Na-Ion Battery Anodes: Nano versus Bulk. *Nano Lett.* **2014**, *14* (3), 1255–1262.
- (117) Su, D.; Dou, S.; Wang, G. Bismuth: A New Anode for the Na-Ion Battery. *Nano Energy* **2015**, *12*, 88–95.
- (118) Xu, Y.; Zhu, Y.; Liu, Y.; Wang, C. Electrochemical Performance of Porous Carbon/Tin Composite Anodes for Sodium-Ion and Lithium-Ion Batteries. *Adv. Energy Mater.* **2013**, *3* (1), 128–133.
- (119) Baggetto, L.; Ganesh, P.; Meisner, R. P.; Unocic, R. R.; Jumas, J.-C.; Bridges, C. A.; Veith, G. M. Characterization of Sodium Ion Electrochemical Reaction with Tin Anodes: Experiment and Theory. *Journal of Power Sources* **2013**, *234*, 48–59.
- (120) Baggetto, L.; Ganesh, P.; Sun, C.-N.; A. Meisner, R.; A. Zawodzinski, T.; M. Veith, G. Intrinsic Thermodynamic and Kinetic Properties of Sb Electrodes for Li-Ion and Na-Ion Batteries: Experiment and Theory. *J. Mater. Chem. A* **2013**, *1* (27), 7985–7994.
- (121) Farbod, B.; Cui, K.; Kalisvaart, W. P.; Kupsta, M.; Zehri, B.; Kohandehghan, A.; Lotfabad, E. M.; Li, Z.; Luber, E. J.; Mitlin, D. Anodes for Sodium Ion Batteries Based on Tin–Germanium–Antimony Alloys. *ACS Nano* **2014**, *8* (5), 4415–4429.

- (122) Fukunishi, M.; Yabuuchi, N.; Dahbi, M.; Son, J.-Y.; Cui, Y.; Oji, H.; Komaba, S. Impact of the Cut-Off Voltage on Cyclability and Passive Interphase of Sn-Polyacrylate Composite Electrodes for Sodium-Ion Batteries. *J. Phys. Chem. C* **2016**, *120* (28), 15017–15026.
- (123) Abel, P. R.; Fields, M. G.; Heller, A.; Mullins, C. B. Tin–Germanium Alloys as Anode Materials for Sodium-Ion Batteries. *ACS Appl. Mater. Interfaces* **2014**, *6* (18), 15860–15867.
- (124) Lin, Y.-M.; Abel, P. R.; Gupta, A.; Goodenough, J. B.; Heller, A.; Mullins, C. B. Sn–Cu Nanocomposite Anodes for Rechargeable Sodium-Ion Batteries. *ACS Appl. Mater. Interfaces* **2013**, *5* (17), 8273–8277.
- (125) Sottmann, J.; Herrmann, M.; Vajeeston, P.; Hu, Y.; Ruud, A.; Drathen, C.; Emerich, H.; Fjellvåg, H.; Wragg, D. S. How Crystallite Size Controls the Reaction Path in Nonaqueous Metal Ion Batteries: The Example of Sodium Bismuth Alloying. *Chem. Mater.* **2016**, *28* (8), 2750–2756.
- (126) Yang, F.; Yu, F.; Zhang, Z.; Zhang, K.; Lai, Y.; Li, J. Bismuth Nanoparticles Embedded in Carbon Spheres as Anode Materials for Sodium/Lithium-Ion Batteries. *Chem. – Eur. J.* **2016**, *22* (7), 2333–2338.
- (127) Obrovac, M. N.; Chevrier, V. L. Alloy Negative Electrodes for Li-Ion Batteries. *Chem. Rev.* **2014**, *114* (23), 11444–11502.
- (128) Zhao, X.; Vail, S. A.; Lu, Y.; Song, J.; Pan, W.; Evans, D. R.; Lee, J.-J. Antimony/Graphitic Carbon Composite Anode for High-Performance Sodium-Ion Batteries. *ACS Appl. Mater. Interfaces* **2016**, *8* (22), 13871–13878.
- (129) Lin, Y.-M.; Abel, P. R.; Heller, A.; Mullins, C. B.  $\alpha$ -Fe<sub>2</sub>O<sub>3</sub> Nanorods as Anode Material for Lithium Ion Batteries. *J. Phys. Chem. Lett.* **2011**, *2* (22), 2885–2891.
- (130) Zhao, Y.; Manthiram, A. High-Capacity, High-Rate Bi–Sb Alloy Anodes for Lithium-Ion and Sodium-Ion Batteries. *Chem. Mater.* **2015**, *27* (8), 3096–3101.
- (131) Baggetto, L.; Allcorn, E.; Manthiram, A.; Veith, G. M. Cu<sub>2</sub>Sb Thin Films as Anode for Na-Ion Batteries. *Electrochemistry Communications* **2013**, *27*, 168–171.
- (132) Baggetto, L.; Allcorn, E.; R. Unocic, R.; Manthiram, A.; M. Veith, G. Mo<sub>3</sub>Sb<sub>7</sub> as a Very Fast Anode Material for Lithium-Ion and Sodium-Ion Batteries. *J. Mater. Chem. A* **2013**, *1* (37), 11163–11169.
- (133) Baggetto, L.; Marszewski, M.; Górka, J.; Jaroniec, M.; Veith, G. M. AlSb Thin Films as Negative Electrodes for Li-Ion and Na-Ion Batteries. *Journal of Power Sources* **2013**, *243*, 699–705.
- (134) Nie, A.; Gan, L.; Cheng, Y.; Tao, X.; Yuan, Y.; Sharifi-Asl, S.; He, K.; Asayesh-Ardakani, H.; Vasiraju, V.; Lu, J.; et al. Ultrafast and Highly Reversible Sodium Storage in Zinc-Antimony Intermetallic Nanomaterials. *Adv. Funct. Mater.* **2016**, *26* (4), 543–552.
- (135) Darwiche, A.; Sougrati, M. T.; Fraisse, B.; Stievano, L.; Monconduit, L. Facile Synthesis and Long Cycle Life of SnSb as Negative Electrode Material for Na-Ion Batteries. *Electrochemistry Communications* **2013**, *32*, 18–21.
- (136) He, M.; Walter, M.; V. Kravchyk, K.; Erni, R.; Widmer, R.; V. Kovalenko, M. Monodisperse SnSb Nanocrystals for Li-Ion and Na-Ion Battery Anodes: Synergy and Dissonance between Sn and Sb. *Nanoscale* **2015**, *7* (2), 455–459.
- (137) Walter, M.; Doswald, S.; V. Kovalenko, M. Inexpensive Colloidal SnSb Nanoalloys as Efficient Anode Materials for Lithium- and Sodium-Ion Batteries. *J. Mater. Chem. A* **2016**, *4* (18), 7053–7059.
- (138) Du, Z.; Hatchard, T. D.; Dunlap, R. A.; Obrovac, M. N. Combinatorial Investigations of Ni-Si Negative Electrode Materials for Li-Ion Batteries. *J. Electrochem. Soc.* **2015**, *162* (9), A1858–A1863.
- (139) Du, Z.; Liu, H.; Ellis, S. N.; Dunlap, R. A.; Zhu, M.; Obrovac, M. N. Electrochemistry of CuxSi<sub>1-x</sub> Alloys in Li Cells. *J. Electrochem. Soc.* **2016**, *163* (7), A1275–A1279.
- (140) Fan, S.; Y. Lim, L.; Yan Tay, Y.; Snellius Pramana, S.; Rui, X.; Kabiri Samani, M.; Yan, Q.; Kang Tay, B.; F. Toney, M.; Hoon Hng, H. Rapid Fabrication of a Novel Sn–Ge Alloy: Structure–Property Relationship and Its Enhanced Lithium Storage Properties. *J. Mater. Chem. A* **2013**, *1* (46), 14577–14585.
- (141) He, K.; Chen, N.; Wang, C.; Wei, L.; Chen, J. Method for Determining Crystal Grain Size by X-Ray Diffraction. *Cryst. Res. Technol.* **2018**, *53* (2), 1700157.
- (142) Holder, C. F.; Schaak, R. E. Tutorial on Powder X-Ray Diffraction for Characterizing Nanoscale Materials. *ACS Nano* **2019**, *13* (7), 7359–7365.

- (143) Baggetto, L.; Hah, H.-Y.; Jumas, J.-C.; Johnson, C. E.; Johnson, J. A.; Keum, J. K.; Bridges, C. A.; Veith, G. M. The Reaction Mechanism of SnSb and Sb Thin Film Anodes for Na-Ion Batteries Studied by X-Ray Diffraction,  $^{119}\text{Sn}$  and  $^{121}\text{Sb}$  Mössbauer Spectroscopies. *Journal of Power Sources* **2014**, *267*, 329–336.
- (144) Li, Z.; Tan, X.; Li, P.; Kalisvaart, P.; Janish, M. T.; Mook, W. M.; Lubber, E. J.; Jungjohann, K. L.; Carter, C. B.; Mitlin, D. Coupling In Situ TEM and Ex Situ Analysis to Understand Heterogeneous Sodiation of Antimony. *Nano Lett.* **2015**, *15* (10), 6339–6348.
- (145) Wu, P.; Du, N.; Zhang, H.; Liu, J.; Chang, L.; Wang, L.; Yang, D.; Jiang, J.-Z. Layer-Stacked Tin Disulfide Nanorods in Silica Nanoreactors with Improved Lithium Storage Capabilities. *Nanoscale* **2012**, *4* (13), 4002–4006.
- (146) Xu, X.; Liu, W.; Kim, Y.; Cho, J. Nanostructured Transition Metal Sulfides for Lithium Ion Batteries: Progress and Challenges. *Nano Today* **2014**, *9* (5), 604–630.
- (147) Tan, G.; Wu, F.; Yuan, Y.; Chen, R.; Zhao, T.; Yao, Y.; Qian, J.; Liu, J.; Ye, Y.; Shahbazian-Yassar, R.; et al. Freestanding Three-Dimensional Core–Shell Nanoarrays for Lithium-Ion Battery Anodes. *Nat. Commun.* **2016**, *7*, 11774.
- (148) Liu, X. H.; Zhong, L.; Huang, S.; Mao, S. X.; Zhu, T.; Huang, J. Y. Size-Dependent Fracture of Silicon Nanoparticles During Lithiation. *ACS Nano* **2012**, *6* (2), 1522–1531.
- (149) McDowell, M. T.; Ryu, I.; Lee, S. W.; Wang, C.; Nix, W. D.; Cui, Y. Studying the Kinetics of Crystalline Silicon Nanoparticle Lithiation with In Situ Transmission Electron Microscopy. *Adv. Mater.* **2012**, *24* (45), 6034–6041.
- (150) Sethuraman, V. A.; Srinivasan, V.; Bower, A. F.; Guduru, P. R. In Situ Measurements of Stress-Potential Coupling in Lithiated Silicon. *J. Electrochem. Soc.* **2010**, *157* (11), A1253–A1261.
- (151) Iaboni, D. S. M.; Obrovac, M. N.  $\text{Li}_{15}\text{Si}_4$  Formation in Silicon Thin Film Negative Electrodes. *J. Electrochem. Soc.* **2016**, *163* (2), A255–A261.
- (152) Wang, J. W.; Liu, X. H.; Mao, S. X.; Huang, J. Y. Microstructural Evolution of Tin Nanoparticles during In Situ Sodium Insertion and Extraction. *Nano Lett.* **2012**, *12* (11), 5897–5902.
- (153) Kim, Y.; Ha, K.-H.; Oh, S. M.; Lee, K. T. High-Capacity Anode Materials for Sodium-Ion Batteries. *Chemistry – A European Journal* **2014**, *20* (38), 11980–11992.
- (154) Mao, J.; Fan, X.; Luo, C.; Wang, C. Building Self-Healing Alloy Architecture for Stable Sodium-Ion Battery Anodes: A Case Study of Tin Anode Materials. *ACS Appl. Mater. Interfaces* **2016**, *8* (11), 7147–7155.
- (155) Ramireddy, T.; Sharma, N.; Xing, T.; Chen, Y.; Leforestier, J.; Glushenkov, A. M. Size and Composition Effects in Sb–Carbon Nanocomposites for Sodium-Ion Batteries. *ACS Appl. Mater. Interfaces* **2016**, *8* (44), 30152–30164.
- (156) Wang, J. W.; Liu, X. H.; Mao, S. X.; Huang, J. Y. Microstructural Evolution of Tin Nanoparticles during In Situ Sodium Insertion and Extraction. *Nano Lett.* **2012**, *12* (11), 5897–5902.
- (157) Zhu, H.; Jia, Z.; Chen, Y.; Weadock, N.; Wan, J.; Vaaland, O.; Han, X.; Li, T.; Hu, L. Tin Anode for Sodium-Ion Batteries Using Natural Wood Fiber as a Mechanical Buffer and Electrolyte Reservoir. *Nano Lett.* **2013**, *13* (7), 3093–3100.
- (158) Xie, H.; Kalisvaart, W. P.; Olsen, B. C.; Lubber, E. J.; Mitlin, D.; Buriak, J. M. Sn–Bi–Sb Alloys as Anode Materials for Sodium Ion Batteries. *J. Mater. Chem. A* **2017**, *5* (20), 9661–9670.
- (159) Liang, L.; Xu, Y.; Wang, C.; Wen, L.; Fang, Y.; Mi, Y.; Zhou, M.; Zhao, H.; Lei, Y. Large-Scale Highly Ordered Sb Nanorod Array Anodes with High Capacity and Rate Capability for Sodium-Ion Batteries. *Energy Environ. Sci.* **2015**, *8* (10), 2954–2962.
- (160) Yaru, L.; Wei-Hong, L.; Zongcheng, M.; Shu-Lei, C. Nanocomposite Materials for the Sodium–Ion Battery: A Review. *Small* **2018**, *14* (5), 1702514.
- (161) Liu, Y.; Xu, Y.; Zhu, Y.; Culver, J. N.; Lundgren, C. A.; Xu, K.; Wang, C. Tin-Coated Viral Nanoforests as Sodium-Ion Battery Anodes. *ACS Nano* **2013**, *7* (4), 3627–3634.
- (162) Nam, D.-H.; Kim, T.-H.; Hong, K.-S.; Kwon, H.-S. Template-Free Electrochemical Synthesis of Sn Nanofibers as High-Performance Anode Materials for Na-Ion Batteries. *ACS Nano* **2014**, *8* (11), 11824–11835.
- (163) Zhu, Y.; Han, X.; Xu, Y.; Liu, Y.; Zheng, S.; Xu, K.; Hu, L.; Wang, C. Electrospun Sb/C Fibers for a Stable and Fast Sodium-Ion Battery Anode. *ACS Nano* **2013**, *7* (7), 6378–6386.

- (164) Sottmann, J.; Herrmann, M.; Vajeeston, P.; Hu, Y.; Ruud, A.; Drathen, C.; Emerich, H.; Fjellvåg, H.; Wragg, D. S. How Crystallite Size Controls the Reaction Path in Nonaqueous Metal Ion Batteries: The Example of Sodium Bismuth Alloying. *Chem. Mater.* **2016**, *28* (8), 2750–2756.
- (165) Xiao, L.; Cao, Y.; Xiao, J.; Wang, W.; Kovarik, L.; Nie, Z.; Liu, J. High Capacity, Reversible Alloying Reactions in SnSb/C Nanocomposites for Na-Ion Battery Applications. *Chem. Commun.* **2012**, *48* (27), 3321–3323.
- (166) Baggetto, L.; Hah, H.-Y.; Jumas, J.-C.; Johnson, C. E.; Johnson, J. A.; Keum, J. K.; Bridges, C. A.; Veith, G. M. The Reaction Mechanism of SnSb and Sb Thin Film Anodes for Na-Ion Batteries Studied by X-Ray Diffraction, <sup>119</sup>Sn and <sup>121</sup>Sb Mössbauer Spectroscopies. *Journal of Power Sources* **2014**, *267*, 329–336.
- (167) Ji, L.; Gu, M.; Shao, Y.; Li, X.; Engelhard, M. H.; Arey, B. W.; Wang, W.; Nie, Z.; Xiao, J.; Wang, C.; et al. Controlling SEI Formation on SnSb-Porous Carbon Nanofibers for Improved Na Ion Storage. *Adv. Mater.* **2014**, *26* (18), 2901–2908.
- (168) Yi, Z.; Han, Q.; Geng, D.; Wu, Y.; Cheng, Y.; Wang, L. One-Pot Chemical Route for Morphology-Controllable Fabrication of Sn-Sb Micro/Nano-Structures: Advanced Anode Materials for Lithium and Sodium Storage. *Journal of Power Sources* **2017**, *342*, 861–871.
- (169) Chen, S.-W.; Chen, C.-C.; Gierlotka, W.; Zi, A.-R.; Chen, P.-Y.; Wu, H.-J. Phase Equilibria of the Sn-Sb Binary System. *Journal of Elec Materi* **2008**, *37* (7), 992–1002.
- (170) Okamoto, H. Sb-Sn (Antimony-Tin). *J. Phase Equilib. Diffus.* **2012**, *33* (4), 347–347.
- (171) Lubner, E.; Mohammadi, R.; Ophus, C.; Lee, Z.; Nelson-Fitzpatrick, N.; Westra, K.; Evoy, S.; Dahmen, U.; Radmilovic, V.; D Mitlin. Tailoring the Microstructure and Surface Morphology of Metal Thin Films for Nano-Electro-Mechanical Systems Applications. *Nanotechnology* **2008**, *19* (12), 125705.
- (172) Yuan, Y.; Amine, K.; Lu, J.; Shahbazian-Yassar, R. Understanding Materials Challenges for Rechargeable Ion Batteries with *in Situ* Transmission Electron Microscopy. *Nat. Commun.* **2017**, *8*, 15806.
- (173) Hasti, A.-A.; Wentao, Y.; Yifei, Y.; Anmin, N.; Khalil, A.; Jun, L.; Reza, S.-Y. In Situ TEM Investigation of ZnO Nanowires during Sodiation and Lithiation Cycling. *Small Methods* **2017**, *1* (9), 1700202.
- (174) Mitlin, D.; Raeder, C. H.; Messler, R. W. Solid Solution Creep Behavior of Sn-XBi Alloys. *Metall and Mat Trans A* **1999**, *30* (1), 115–122.
- (175) Li, Z.; Tan, X.; Li, P.; Kalisvaart, P.; Janish, M. T.; Mook, W. M.; Lubner, E. J.; Jungjohann, K. L.; Carter, C. B.; Mitlin, D. Coupling In Situ TEM and Ex Situ Analysis to Understand Heterogeneous Sodiation of Antimony. *Nano Lett.* **2015**.
- (176) Gu, M.; Kushima, A.; Shao, Y.; Zhang, J.-G.; Liu, J.; Browning, N. D.; Li, J.; Wang, C. Probing the Failure Mechanism of SnO<sub>2</sub> Nanowires for Sodium-Ion Batteries. *Nano Lett.* **2013**, *13* (11), 5203–5211.
- (177) Liu, Y.; Fan, F.; Wang, J.; Liu, Y.; Chen, H.; Jungjohann, K. L.; Xu, Y.; Zhu, Y.; Bigio, D.; Zhu, T.; et al. In Situ Transmission Electron Microscopy Study of Electrochemical Sodiation and Potassiation of Carbon Nanofibers. *Nano Lett.* **2014**, *14* (6), 3445–3452.
- (178) Lu, X.; Adkins, E. R.; He, Y.; Zhong, L.; Luo, L.; Mao, S. X.; Wang, C.-M.; Korgel, B. A. Germanium as a Sodium Ion Battery Material: In Situ TEM Reveals Fast Sodiation Kinetics with High Capacity. *Chem. Mater.* **2016**, *28* (4), 1236–1242.
- (179) Iaboni, D. S. M.; Obrovac, M. N. Li<sub>15</sub>Si<sub>4</sub> Formation in Silicon Thin Film Negative Electrodes. *J. Electrochem. Soc.* **2016**, *163* (2), A255–A261.
- (180) Gao, H.; Xiao, L.; Plümel, I.; Xu, G.-L.; Ren, Y.; Zuo, X.; Liu, Y.; Schulz, C.; Wiggers, H.; Amine, K.; et al. Parasitic Reactions in Nanosized Silicon Anodes for Lithium-Ion Batteries. *Nano Lett.* **2017**, *17* (3), 1512–1519.
- (181) Sayed, S. Y.; Kalisvaart, W. P.; Olsen, B. C.; Lubner, E. J.; Xie, H.; Buriak, J. M. Alternating Silicon and Carbon Multilayer-Structured Anodes Suppress Formation of the c-Li<sub>3.75</sub>Si Phase. *Chem. Mater.* **2019**.
- (182) Wang, Y.; Cao, S.; Kalinina, M.; Zheng, L.; Li, L.; Zhu, M.; Obrovac, M. N. Lithium Insertion in Nanostructured Si<sub>1-x</sub>Ti<sub>x</sub> Alloys. *J. Electrochem. Soc.* **2017**, *164* (13), A3006–A3010.
- (183) Du, Z.; Ellis, S. N.; Dunlap, R. A.; Obrovac, M. N. Ni<sub>x</sub>Si<sub>1-x</sub> Alloys Prepared by Mechanical Milling as Negative Electrode Materials for Lithium Ion Batteries. *J. Electrochem. Soc.* **2016**, *163* (2), A13–A18.

- (184) Du, Z.; Liu, H.; Ellis, S. N.; Dunlap, R. A.; Zhu, M.; Obrovac, M. N. Electrochemistry of  $\text{Cu}_x\text{Si}_{1-x}$  Alloys in Li Cells. *J. Electrochem. Soc.* **2016**, *163* (7), A1275–A1279.
- (185) Dahn, J. R.; Mar, R. E.; Abouzeid, A. Combinatorial Study of  $\text{Sn}_{1-x}\text{Co}_x$  ( $0 < x < 0.6$ ) and  $[\text{Sn}_{0.55}\text{Co}_{0.45}]_{1-y}\text{C}_y$  ( $0 < y < 0.5$ ) Alloy Negative Electrode Materials for Li-Ion Batteries. *J. Electrochem. Soc.* **2006**, *153* (2), A361–A365.
- (186) Sethuraman, V. A.; Srinivasan, V.; Bower, A. F.; Guduru, P. R. In Situ Measurements of Stress-Potential Coupling in Lithiated Silicon. *J. Electrochem. Soc.* **2010**, *157* (11), A1253–A1261.
- (187) Shin, J.; Cho, E. Agglomeration Mechanism and a Protective Role of  $\text{Al}_2\text{O}_3$  for Prolonged Cycle Life of Si Anode in Lithium-Ion Batteries. *Chem. Mater.* **2018**, *30* (10), 3233–3243.
- (188) Xiao, X. Multifunctional Surface Coating As Artificial Solid Electrolyte Interphase for Lithium Ion Batteries. *Meet. Abstr.* **2014**, MA2014-01 (3), 341–341.
- (189) Halim, M.; Kim, J. S.; Choi, J.-G.; Lee, J. K. Electrochemical Characterization of Carbon Coated Bundle-Type Silicon Nanorod for Anode Material in Lithium Ion Secondary Batteries. *Applied Surface Science* **2015**, *334*, 115–122.
- (190) Memarzadeh Lotfabad, E.; Kalisvaart, P.; Kohandehghan, A.; Cui, K.; Kupsta, M.; Farbod, B.; Mitlin, D. Si Nanotubes ALD Coated with  $\text{TiO}_2$ ,  $\text{TiN}$  or  $\text{Al}_2\text{O}_3$  as High Performance Lithium Ion Battery Anodes. *J. Mater. Chem. A* **2014**, *2* (8), 2504–2516.
- (191) Kim, S. J.; Kargar, A.; Wang, D.; Graham, G. W.; Pan, X. Lithiation of Rutile  $\text{TiO}_2$ -Coated Si NWs Observed by in Situ TEM. *Chem. Mater.* **2015**, *27* (20), 6929–6933.
- (192) Keil, P.; Jossen, A. Charging Protocols for Lithium-Ion Batteries and Their Impact on Cycle Life—An Experimental Study with Different 18650 High-Power Cells. *Journal of Energy Storage* **2016**, *6*, 125–141.
- (193) Wetjen, M.; Pritzl, D.; Jung, R.; Solchenbach, S.; Ghadimi, R.; Gasteiger, H. A. Differentiating the Degradation Phenomena in Silicon-Graphite Electrodes for Lithium-Ion Batteries. *J. Electrochem. Soc.* **2017**, *164* (12), A2840–A2852.
- (194) Aghajamali, M.; Xie, H.; Javadi, M.; Kalisvaart, W. P.; Buriak, J. M.; Veinot, J. G. C. Size and Surface Effects of Silicon Nanocrystals in Graphene Aerogel Composite Anodes for Lithium Ion Batteries. *Chem. Mater.* **2018**, *30* (21), 7782–7792.
- (195) Chen, L. B.; Xie, J. Y.; Yu, H. C.; Wang, T. H. An Amorphous Si Thin Film Anode with High Capacity and Long Cycling Life for Lithium Ion Batteries. *J. Appl. Electrochem.* **2009**, *39* (8), 1157–1162.
- (196) Gauthier, M.; Mazouzi, D.; Reyter, D.; Lestriez, B.; Moreau, P.; Guyomard, D.; Roué, L. A Low-Cost and High Performance Ball-Milled Si-Based Negative Electrode for High-Energy Li-Ion Batteries. *Energy Environ. Sci.* **2013**, *6* (7), 2145–2155.
- (197) Schroder, K. W.; Dylla, A. G.; Harris, S. J.; Webb, L. J.; Stevenson, K. J. Role of Surface Oxides in the Formation of Solid–Electrolyte Interphases at Silicon Electrodes for Lithium-Ion Batteries. *ACS Appl. Mater. Interfaces* **2014**, *6* (23), 21510–21524.
- (198) Schroder, K. W.; Celio, H.; Webb, L. J.; Stevenson, K. J. Examining Solid Electrolyte Interphase Formation on Crystalline Silicon Electrodes: Influence of Electrochemical Preparation and Ambient Exposure Conditions. *J. Phys. Chem. C* **2012**, *116* (37), 19737–19747.
- (199) Schroder, K.; Alvarado, J.; Yersak, T. A.; Li, J.; Dudney, N.; Webb, L. J.; Meng, Y. S.; Stevenson, K. J. The Effect of Fluoroethylene Carbonate as an Additive on the Solid Electrolyte Interphase on Silicon Lithium-Ion Electrodes. *Chem. Mater.* **2015**, *27* (16), 5531–5542.
- (200) Pan, Q.; Lou, S.; Zuo, P.; Mu, T.; Du, C.; Cheng, X.; Ma, Y.; Gao, Y.; Yin, G. Toward Promising Turnkey Solution for Next-Generation Lithium Ion Batteries: Scale Preparation, Fading Analysis, and Enhanced Performance of Microsized Si/C Composites. *ACS Appl. Energy Mater.* **2018**, *1* (12), 6977–6985.
- (201) Wang, W.; Yang, S. Enhanced Overall Electrochemical Performance of Silicon/Carbon Anode for Lithium-Ion Batteries Using Fluoroethylene Carbonate as an Electrolyte Additive. *Journal of Alloys and Compounds* **2017**, *695*, 3249–3255.
- (202) Nishi, Y. Lithium Ion Secondary Batteries; Past 10 Years and the Future. *Journal of Power Sources* **2001**, *100* (1), 101–106.
- (203) Jorn, R.; Kumar, R.; Abraham, D. P.; Voth, G. A. Atomistic Modeling of the Electrode–Electrolyte Interface in Li-Ion Energy Storage Systems: Electrolyte Structuring. *J. Phys. Chem. C* **2013**, *117* (8), 3747–3761.

- (204) Owejan, J. E.; Owejan, J. P.; DeCaluwe, S. C.; Dura, J. A. Solid Electrolyte Interphase in Li-Ion Batteries: Evolving Structures Measured In Situ by Neutron Reflectometry. *Chem. Mater.* **2012**, *24* (11), 2133–2140.
- (205) Löbl, P.; Huppertz, M.; Mergel, D. Nucleation and Growth in TiO<sub>2</sub> Films Prepared by Sputtering and Evaporation. *Thin Solid Films* **1994**, *251* (1), 72–79.
- (206) Takeda, S.; Suzuki, S.; Odaka, H.; Hosono, H. Photocatalytic TiO<sub>2</sub> Thin Film Deposited onto Glass by DC Magnetron Sputtering. *Thin Solid Films* **2001**, *392* (2), 338–344.
- (207) Mardare, D.; Tasca, M.; Delibas, M.; Rusu, G. I. On the Structural Properties and Optical Transmittance of TiO<sub>2</sub> r.f. Sputtered Thin Films. *Applied Surface Science* **2000**, *156* (1), 200–206.
- (208) Ferguson, P. P.; Todd, A. D. W.; Dahn, J. R. Comparison of Mechanically Alloyed and Sputtered Tin–Cobalt–Carbon as an Anode Material for Lithium-Ion Batteries. *Electrochemistry Communications* **2008**, *10* (1), 25–31.
- (209) Ren, Y.; Liu, Z.; Pourpoint, F.; Armstrong, A. R.; Grey, C. P.; Bruce, P. G. Nanoparticulate TiO<sub>2</sub>(B): An Anode for Lithium-Ion Batteries. *Angew. Chem. Int. Ed.* **2012**, *51* (9), 2164–2167.
- (210) Kalisvaart, W. P.; Xie, H.; Olsen, B. C.; Luber, E. J.; Buriak, J. M. Understanding the Mechanism of Enhanced Cycling Stability in Sn–Sb Composite Na-Ion Battery Anodes: Operando Alloying and Diffusion Barriers. *ACS Appl. Energy Mater.* **2019**.
- (211) Ronneburg, A.; Trapp, M.; Cubitt, R.; Silvi, L.; Cap, S.; Ballauff, M.; Risse, S. Surface Structure Inhibited Lithiation of Crystalline Silicon Probed with Operando Neutron Reflectivity. *Energy Storage Materials* **2019**, *18*, 182–189.